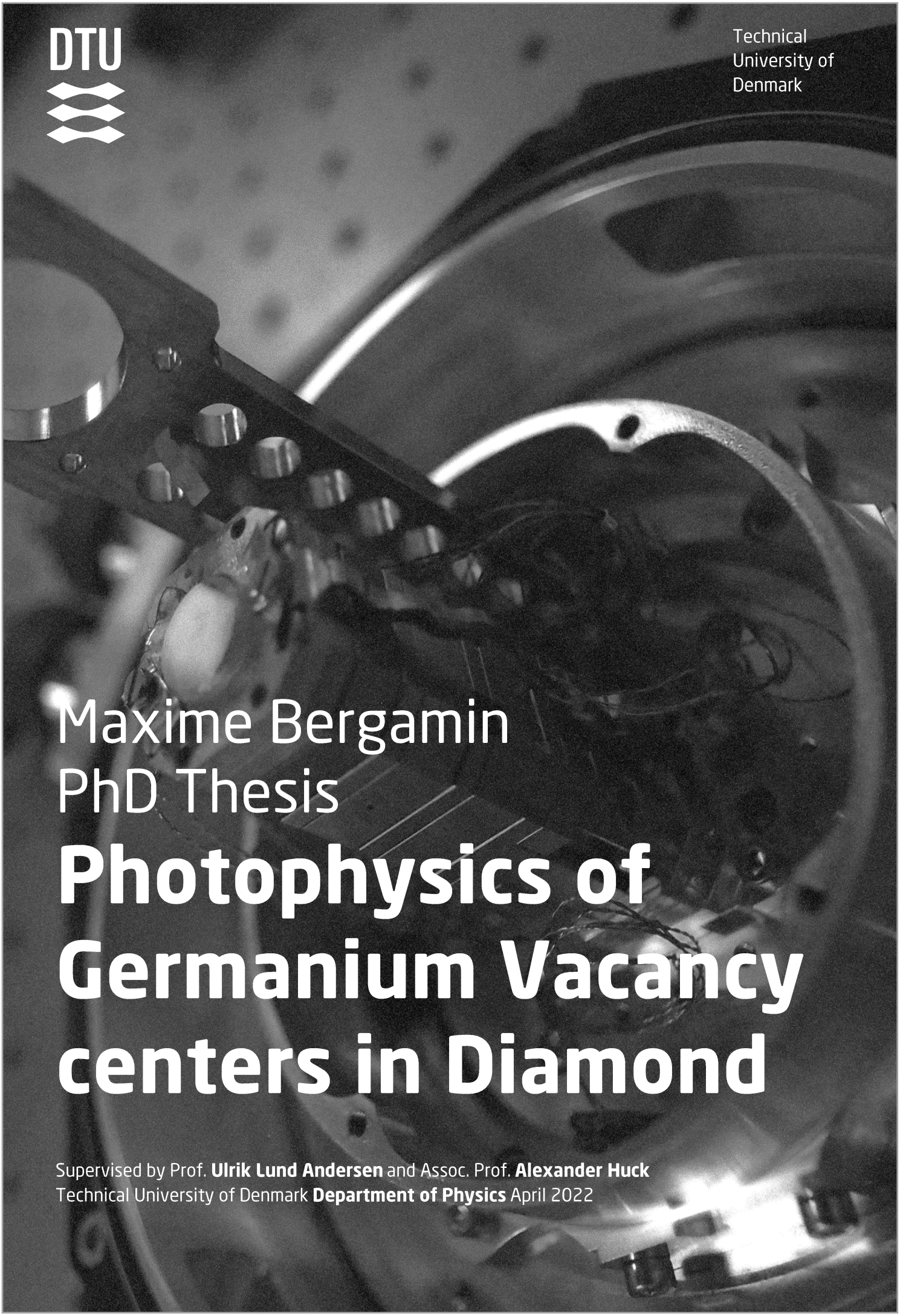

DTU

Technical University of Denmark

Maxime Bergamin

PhD Thesis

Photophysics of Germanium Vacancy centers in Diamond

Supervised by Prof. **Ulrik Lund Andersen** and Assoc. Prof. **Alexander Huck**
Technical University of Denmark **Department of Physics** April 2022

Photophysics of Germanium-Vacancy centers in Diamond

PhD dissertation

April 2022

By Maxime Bergamin

This project was part of BigQ, with the support of the Danish National Research Foundation

Cover photo: GeV centers diamond sample in Attocube cryostat chamber

Published by: DTU, Fysik, Fysikvej, Building 307, 2800 Kgs. Lyngby, Denmark

www.dtu.dk

Abstract

Point defects in diamond are promising candidates in the solid-state for a wide range of applications in quantum information processing. Among different defects with allowed optical transitions, the germanium-vacancy center (GeV) is attractive because it has good optical properties at room temperature, including a narrow zero-phonon line and low emission into the phonon sideband. Some of the GeV center's intrinsic physical properties are yet unknown. This contribution focuses on the optical investigation of single GeV center deeply implanted into a synthetic diamond crystal at a cryogenic sample temperature of 4K. Single GeV center's optical properties are monitored by collecting photons emitted in the phonon side band and the zero-phonon line using a cross-polarization scheme. Applying a resonant optical excitation scheme, we report on the observation of fluorescence switching effects with the evidence of a dark shelving state, optical gating of the phonon-sidebands emission with the addition of weak power off-resonant laser, and discrete spectral jumps. Further, evidence of nonclassical states of light is studied using a dual correlation approach. Finally, a fiber-based Fabry-Pérot microcavity in a bath cryostat design is proposed as a low vibration solution for enabling Purcell enhancement.

Dansk Resumé

Defekter i diamanter er en lovende faststofs kandidater til adskillige anvendelser inden for kvanteinformation. Blandt forskellige typer af defekter med den tilladte optiske overgang, er germanium-vacancy center (GeV) særlig attraktiv, grundet de gode optiske egenskaber ved stuetemperatur, blandt andet en smal nul-fonon linje og en lav emission til fonon sidebåndet.

Nogle iboende fysiske egenskaber for GeV centre er endnu ukendte. Dette bidrag har fokus på den optiske undersøgelse af dybt implanteret enkelte GeV centre i en syntetisk diamant krystal ved kryogeniske temperaturer på 4 K.

Et GeV center optiske egenskaber kan observeres gennem fotoner udsendt i det fononiske sidebånd og nul-fonon-linjen ved brug af (et) kryds-polarisering(s skema/protokol). Ved at anvende resonant optisk excitations målinger, observerer vi fluorescens switching effekter som er evidens af en mørk tilstand, optisk gating af en fonon-sidebånds-emission ved yderligere anvendelse af en ikke-resonant laser ved lav effekt, samt diskrete spektrale hop.

Herudover er evidens af ikke-klassiske lys tilstande blevet undersøgt ved brug af dobbelt korrelations målinger. Endelig, er et design for en fiber baseret Fabry-Pérot mikro-kavitet i en bad kryostat foreslået som en lav-vibration løsning til at opnå Purcell effekt.

Acknowledgements

The last three-and-a-half years were a nonstop rollercoaster which I went through with the help and support of so many people.

I first want to thank my supervisor Ulrik Lund Andersen, who found a place for me in his big group and manages to keep it together. On the same level, I thank my other supervisor, Alexander Huck, for his unbridled energy and continuous help and guidance. May your morning double coffee shot always be with you.

I want to thank my successive mentors, Olivier and Ilya, for their never-ending support and patience in the lab. Olivier, I would have never started without your optimism. Ilya, I would have never finished without your wisdom… I will miss our conversations.

Thanks to my office mates in diamond, Rasmus Light-sleeper, Deepak Black-tongue, Juanita, Yannik, and Rakshyaskar. You've helped me so much in so many ways that it's hard to find the right words to say how grateful I am to have shared these moments with you.

To my brother in arms, Angelo, it requires a companion to join the battle from D-day until the last breath. Thanks to my QPIT buddies, Luca, Iyad, and Sissel, for bringing some fun to work. And of course, Joost, Arne, Teresa, Josh, Adnan, Anna, Jens, Casper, Rayssa, Josh, Haitham, Luiz, Anders, I enjoyed the bit of life we shared on the battlefield.

Daniel, well… thank you and godspeed!

I'm particularly thankful to Tine, Søren, and his team for the invaluable work you're doing for us. I don't think I've thanked you enough.

Thanks to Lily for welcoming me into her lab *Montréalais*, and thanks to Cesar, Rigel, and Adrian for the time you shared with me. And of course, Erika, thank you for your positive energy during your visits (and making such precious samples).

I want to thank Lukas for helping me understanding his work.

To my other brothers in arms from *La Une,* I really enjoyed the Octobers' duty getaways as chief *tarmaquisticianisticien* with you guys: "*y-en a qu'une*…*!*"

Thanks to my family and friends in Switzerland, Australia, France, and CPH for always being present for me.

Merci à mes parents. Votre petiot a enfin fini ses études.

Hermine, you bring endless happiness and support in my life. Thank you.

Table of contents

List of Abbreviations

AOM .....Acousto Optical Modulator

APD .....Avalanche Photo Diode

ASP .....Amplitude Spectral Density

BS .....Beam Splitter

CB.....Conduction Band

CTL .....Continuous Tunable Laser

CW.....Continuous Wave

FWHM.....Full Width at Half Maximum

HBT .....Hanbury-Brown and Twiss

HWP.....Half Wave Plate

IR.....Infrared

LED .....Light Emitting Diode

MBE.....Molecular Beam Epitaxy

ND .....Neutral Density filter

PBS .....Polarizing Beam Splitter

PD.....Photon-detector

PL .....Photoluminescence

PSB.....Phonon-Sidebands

PSD .....Power Spectral Density

QWP .....Quarter Wave Plate

RF .....Resonance Fluorescence

SC.....Semi-Conductor

SPAD .....Single Photon Avalanche Diode

TE .....Transverse Electric field

TM.....Transverse Magnetic field

TTL .....Transistor-Transistor Logic

TTTR.....Time Tagged Time Resolved

VB.....Valence Band

WG .....Wave Guide

WM .....Wavemeter

ZPL.....Zero-Phonon Line

Contributions

PhD project

Maxime Bergamin: Contributed to the experimental design and construction, data acquisition, analysis and interpretation.

Ilya Radko: Contributed to the experimental design and results interpretation.

Olivier Gobron & Yuriy Zakharko: Designed and built the cavity and the cryogenic setup described in Ch.8.

Daniel Allepuz Requena: Contributed to the fabrication of the cross-polarization extinction setup.

Erika Janitz: Fabricated the diamond sample used in this work.

Alexander Huck: Contributed with the supervision of the project, the experimental design, and data interpretation.

Ulrik L. Andersen: Contributed with the supervision of the project, and data interpretation.

Analysis of hBN and GeV using dual correlation functions α and β (manuscript in preparation)

Lukas Lachman: Contributed in the nonclassicality detection modelling and interpretation, and manuscript writing.

Maxime Bergamin: Contributed to the experimental design and construction, GeV data acquisition, analysis and interpretation, and manuscript revision.

Ilya Radko: Contributed to the experimental design, hBN data acquisition, and data interpretation.

Alexander Huck: Contributed to the data interpretation, manuscript writing and revision.

Radim Filip: Contributed to the data interpretation, manuscript writing and revision.

CHAPTER 1

INTRODUCTION

"There is nothing new to be discovered in physics now. All that remains is more and more precise measurement."

William Thomson, 1st Baron Kelvin, 1897

In the early 20th century, a new paradigm for our understanding of physical phenomena emerged with a new theory, quantum mechanics. A new era was born. This new science gave the tools to answer problems that were not even suspected. It took a few decades to see the emergence of new technologies ruled by this revolutionary theory's predictions. Nuclear energy, semiconductor electronics, MRI scanners, and lasers came to the public and transformed our society in a way that science fiction writers could hardly predict. It is impossible to look at our lives and acknowledge the importance of the work of Einstein, Bohr, Heisenberg, and all those names that changed the course of mankind's history. It was the first quantum revolution.

The technologies developed by this novel theory used ensembles of quantum effects to produce a signal strong enough that contemporary instruments could measure. The scanning tunneling microscope measures a stream of electrons overcoming a potential barrier, a transistor act as a switch using doped semiconductors comprising a significant ensemble of charges to block or let electrons flow, and a laser amplifies atoms photoemission to generate billions and billions of photons. The continuous innovation of new technologies, which directly resulted from the first quantum revolution, allowed us to delve deeper into the matter and access individual particles at a quantum level. It enabled a new technological paradigm transforming all the standards established over decades of development. We entered the second quantum revolution.

The upheavals might not yet reach the public as the advent of semiconductor electronics has; it will still lead to tremendous technological transformation in the way we practice secure communication [1], sense with unparalleled sensitivity [2], and enable the invention and development of quantum computing [3]. These new branches of quantum information

science and technology are still undergoing considerable research to find suitable candidates for wide-scale industrialization. Quantum sensors, for example, often use continuous-variable systems such as squeezed states of light [4] or environment-sensitive energy levels to reach ultra-high sensitivity [5]. On the other hand, quantum computing and communication rely on interconnected qubits as core elements of their operating principle to beat their classical counterparts. Photonic systems are investigated as possible solutions towards building a quantum computer; they appear to be natural candidates for building a scalable quantum telecommunication network where re-using existing optical fiber infrastructures is desirable [6,7]. In either case, such networks need long-lived quantum memories to perform operations or transmit information in the required processing time.

Quantum memory is an essential construction block in quantum repeaters and quantum processors. In a quantum network, information carried between nodes by flying qubits (such as photons) is disturbed. Nodes typically consist of one or more stationary qubits, which can be encoded with quantum information. Several photonic solutions exist for this role. One can cite quantum dots [8], 2D materials such as hBN/WSe2/TMDC [9], ion traps [10], and defects in diamonds [11,12]. The criteria that will determine the best candidates will be found in their photophysical properties and integration abilities. Stable homogeneous spectral properties, for example, are necessary to enable a coherent and deterministic drive of the quantum state. Too much spectral diffusion would make it challenging to perform the operations with high fidelity over time, and a significant spectral distribution among different inter-connected emitters can prevent communication between nodes. A high-emission rate is a crucial feature for high-speed telecommunication to transmit a large volume of information. In terms of quantum emitters, it translates by a short excited-state lifetime and high quantum efficiency. A favored encoding vector for stationary quantum qubits is the electrons' spin. Therefore, a long electron spin coherence time is also desirable to perform the necessary gate operations and transmit information over long distances between sending and receiving nodes. Finally, integration is equally essential to building a scalable quantum network. Engineering and tailoring of the quantum emitters into the standardized photonic system must be considered.

Despite their name, defects in diamond exhibit most of the advantageous optical properties and have proved to be serious contenders for quantum information processing technologies. The following paragraphs will focus on their integration into photonic platforms, which can take different roles.

Color centers in diamond can act as an interface between a stationary (local electron of nuclear spin) and a flying qubit (photons). The optical in- and out-coupling can be done using a free-space, fiber, or nanophotonic waveguide approach. The excitation will mainly depend

on the emitter's absorption cross-section; it is commonly performed using a free-space method, whether it is embedded in a photonic waveguide, in a bulk substrate, or standing on a substrate. The collection can take many forms; solid immersion lenses expand the numerical aperture increasing the collection efficiency [13], tapered fibers coupled to nanobeam waveguides have also proved to get coupling efficiency up to 97 % [14], or inverse vertical coupler fabricated on waveguides [15]. Eventually, fiber-based microcavities have also shown excellent collection yield [16].

The spins associated with a color center in diamond can also be manipulated typically using microwaves and the spin coherence can be prolonged via dynamical control. It can be done using so-called dynamical decoupling protocols, such as the Carr-Purcell-Meiboom-Gill scheme [17]. This modulation re-synchronizes the dephasing with a series of pulse schemes to suppress the system's decoherence. The application of external magnetic fields induces energy levels to undergo a Zeeman splitting, giving access to additional electronic structures to do qubit manipulation [18].

Increasing the coherence by limiting the electron-phonon interaction can be achieved by cooling down the temperature. Cryostats offer cooling powers down to sub-millikelvin regimes, which can be determinant to increase the coherence time and reduce the linewidth [19].

Finally, a solid-state platform can also act as a spontaneous emission booster by increasing the light-matter interaction. It is achieved by inserting the emitter inside an optical resonator. When the optical cavity mode volume becomes small enough, the radiative decay rate increases by the so-called Purcell factor. Different directions have been pursued to find the best cavity design, such as nanopillars [20] and nanoring resonators [21], photonic crystal cavities, and fiber-based open cavities have shown the most promising results toward a wide-scale integration.

Photonic crystal cavities have been extensively used in photonic applications using semiconductor industry fabrication processes. Similar methods were used with a nanodiamond placed on the waveguide [22]. In this particular case, the sample was placed at the center of the cavity using an atomic force microscope (AFM). However, the development of new processes and dedicated use of ICP-RIE plasma etching chambers enabled bulk diamond tailoring [23]. Emitted photons are then outcoupled using diffraction gratings or tapered fibers, as mentioned earlier. The main limitation of this approach is the lack of tunability. Indeed, the diamond defects need to be incorporated appropriately inside the cavity, and the optical transition needs to be in resonance with the cavity mode.

Open cavities have practically the opposite characteristics; excellent tunability properties but challenging integration capabilities. Many designs exist; Plano-parallel, spherical, concave-convex, and hemispherical. The latter has been the privileged arrangement in diamond photonics as it offers a broad stability regime, and the flat side can be used to place a diamond membrane. The concave mirror is often etched at the tip of an optical fiber, which gives the possibility of sending emitted photons in a quantum network [16]. Most of the elements can be mounted on actuators which allow to vary the cavity distance and do spatial selection of the emitters. But this tunability comes with a cost; the degrees of freedom offered by this approach makes the system highly sensitive to vibrations and drifts. Therefore, supplementary control is required to compensate for such effect, adding complexity to the platform.

This thesis presents one of the many types of vacancy centers in diamond, the germanium, or GeV centers [24]. It starts by describing the emitters and the sample fabrication process to expose possible roots for explaining the work done in this thesis. After a description of the experimental setup, results presenting the observation of fluorescence switching are detailed and discussed whereas the possible causes for these phenomena. A chapter is dedicated to the detection of nonclassical states of light in the emitted photons. Finally, a cryogenic fiber-based open Fabry-Pérot cavity setup presentation will conclude and offer possible outlooks regarding the integration of GeV centers in diamond.

CHAPTER 2

BACKGROUND AND THEORY

2.1 DEFECTS CENTER IN DIAMOND

Diamond is considered to be one of the noblest materials and has been used as ornament for centuries. It's the hardest element on earth, and its natural fabrication process takes place in exceptional thermodynamical conditions, which takes millions, even billions of years.

Defects in diamond have been known for a long time. Jeweler industrials were interested in understanding the meaning of impurities and what could result from a marketing point of view. In their natural form, these defects can impact the color of the stone, e.g., 10 ppm of nitrogen inclusion leads to a yellow diamond, which could influence its commercial value.

In science, the diamond's hardness was the main point of focus, e.g., in developing Anvil cells to measure other materials' hardness or in using nanodiamonds in grinder blades to enhance the cutting power.

A new kind of interest emerged with the second quantum revolution. The defects' optical properties appeared to be exceptional for a natural material; they could behave as a single-photon source [25,26]. One defect in particular came under a lot of scrutinies: the nitrogen-vacancy centers, or NV centers. The M-vacancy centers defects are characterized by two adjacent carbon atoms being replaced by a single guest atom (M), leaving a discrepancy in the crystalline structure or vacancy. In the case of the NV centers, the nitrogen atom will substitute one of the vacant sites and leave the other free (see Fig.1), forming a C_{3V} symmetry. This results in spin-triplets $^3A_2$ orbital in the ground state and ^3E in the excited state, split by a 1.95 eV, or 637 nm for the zero-phonon line (ZPL). NVs have a spin-dependent fluorescence, which is a great feature allowing for optical read-out of the spin state. Furthermore, optical pumping can initialize the spin qubit and microwave control can be used to coherently manipulate the spin state. The branching ratio into the ZPL is characterized by a low Debye-Waller factor of ~3 % [27], which can be disappointing for quantum information processing technologies, where the broad spectrum coming from the phonon-sideband is not of great interest.

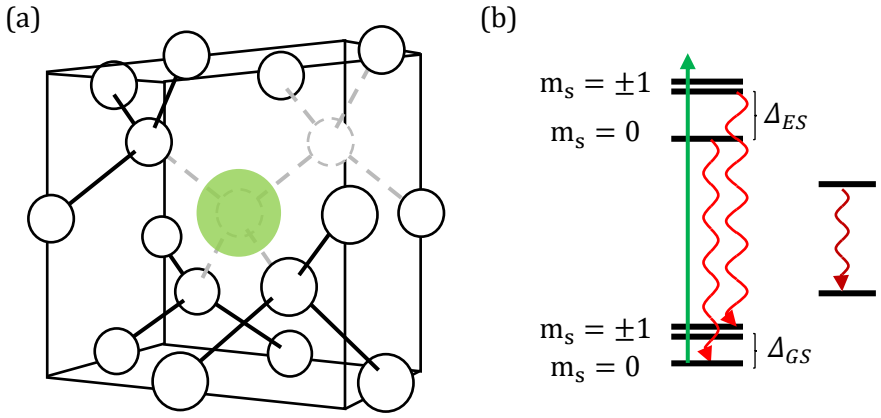

Figure 1 – (a) Atomic structure of the NV centers in diamond, where the nitrogen atom substitutes one of the di-vacancy sites. (b) Simplified electronic structure of the NV centers with the ground and excited states spin triplets, and intermediate-state singlets.

Nonetheless, NV centers have shown very long nuclear and electron spin coherence times, up to one second [28,29]. Moreover, electron spin coherence T_2 of 1.8 ms was measured at room temperature. This is due to weak spin-orbit coupling in the ground state and only limited by spin-spin interactions [30]. A high quantum efficiency (QE) of ~0.75 [31] is limited by a long excited-state lifetime of 12 ns [32]. Finally, it has been shown that it was possible to switch between the NV centers negative and neutral charge states with different excitation conditions [33].

One can see the contrast in the NV centers optical and electronic properties between long spin coherence times, high QE, but low Debye-Waller factor, and high excited-state lifetime. However, its strong interaction with external physical variations such as magnetic field, temperature, and pressure guarantees its interest in the field of quantum sensing.

NV centers is not the only defect that finds a place in quantum technology applications. Another class appeared to have interesting properties, and it was discovered as being a collateral imperfection from the NV fabrication process. Some silicon impurities remaining in vacuum and deposition chambers from the silicon industry accidentally included some of this element in diamonds [34]. They rapidly showed interesting properties that unraveled a new field of research, the group-IV defects in diamond.

2.2 THE GROUP-IV DEFECTS

This class of defects is composed of the group-IV elements: silicon, germanium, tin, and lead. In contrast with the NV centers where the nitrogen was substituting a carbon atom, the group-IV impurity will lie between the two vacancies, forming D_{3d} symmetry with the <111> axis, also called split-vacancy. This structure has an inversion symmetry that induces a vanishing

permanent electric dipole. Hence, the group-IV centers are invariant to fluctuating external electric fields. Eleven electrons are involved in the negatively charged configuration, 6 from adjacent carbon atoms, 4 from the group-IV element, and 1 from the crystal lattice, inducing the negative charge. The ground-state has a ^2E_g, and the excited-state has a ^2E_u orbitals and have double orbital degeneracy.

The common negatively charged has a half-occupied ground-state, yielding a spin S=1/2. A high Debye-Waller factor characterizes them, e.g., ~60 % of fluorescence branches into the ZPL for the GeV and SnV [24,35] and up to 70 % for SiV centers [36]. Due to spin-orbit interaction, the ground and excited states split into two energy levels at low temperatures resulting in four optical transitions, as shown in Fig.2. The large ground-state splitting of group-IV defects were predicted by DFT calculations, suggesting long electron spin coherence times, added to high QE [37]. Moreover, results showed that this class of defects has short few nanoseconds excited-state lifetimes. The table below summarizes the optical properties of the group-IV defects in diamond:

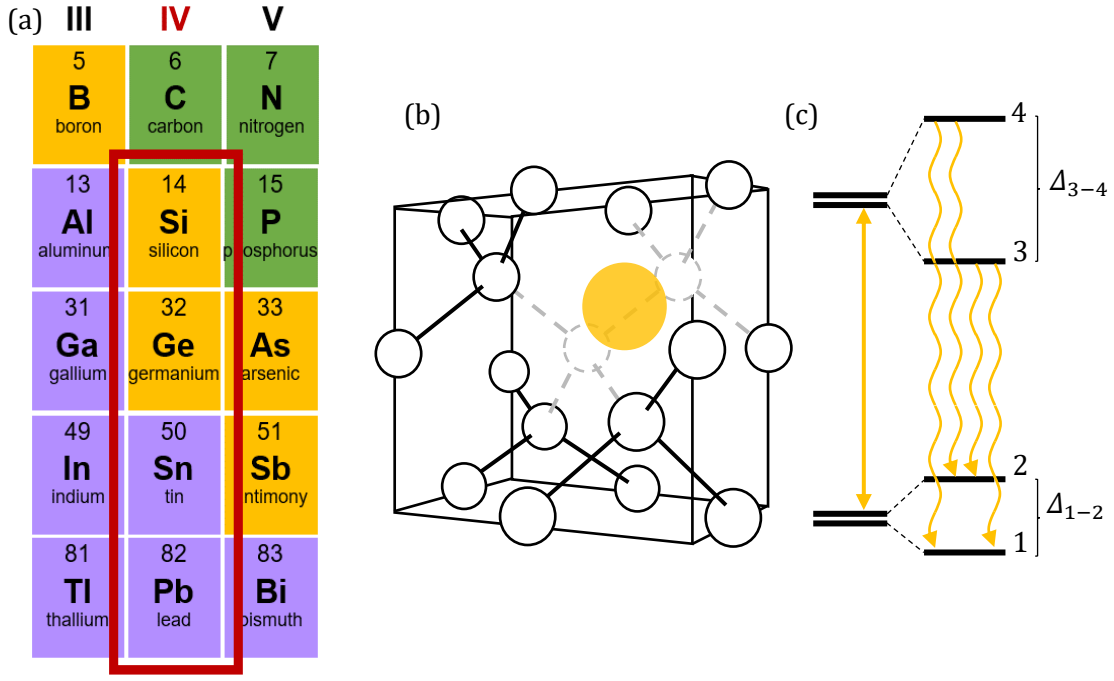

Figure 2 – (a) Group-IV elements, including the silicon, germanium, tin and lead, which will form a vacancy defect complex by sitting at the center of the divacancy of a diamond lattice (b). (c) The electronic structure shows the ground and excited splitting enabling four optical transitions at cold temperatures.

	ZPL λ (nm)	Exc. state lifetime (ns)	Debye-Waller	QE
SiV-	738 [38]	1-2.4 [34]	0.7 [36]	0.34-0.66% [39]
GeV-	602 [24]	1.4-5.5 [24]	0.6 [40]	measured 0.22 [41]
SnV-	619 [42]	4.5 [43,44]	0.6 [35]	expected 80% [42]
PbV-	520-552 [36,39,45,46]	3.7-4.5 [46,47]	unk.	unk.

Table 1 – Optical properties of the group-IV defects.

It was shown that low temperatures are necessary to limit the ground-state dephasing coming from the phonon-mediated transition rate, which is proportional to the occupation of the phonon mode [48]:

$$n(\Delta_{gs}, T) = 1/(e^{(h\Delta_{gs}/k_B T)} - 1) \quad (2\text{-}1)$$

This results in sub-millikelvin for SiV, 7 K for GeV, 40 K for SnV, and 200 K for PbV. Different measurements were done to characterize the spin properties, using coherent population trapping (CPT) to measure the spin relaxation time T_1 and dephasing time T_2^* of 2.4 ns and 35 ns for SiV centers at 5 K [49], and 25 μs and 20 ns at 2.2 K for GeV centers [50]. Ramsey measurements showed 45-115 ns spin coherence times for SiV centers at 4 K [18,51], and Carr-Purcell-Meiboom-Gill CPMG pulse sequences showed T_2 of 13 ms and T_1 up to 1 second at 100 mK [19]. It has also been shown that spin coherence time could be enhanced by 6 fold using strain engineering [52]. Fabrication of PbV sample is still challenging to date, T_1 of 10 ms at 2.9 K [53] and T_2 of 0.3 ms at 1.7 K [54] were demonstrated for SnV centers. The table below shows the main electronic and spin properties of group-IV defects.

	Z	Δ_{gs} exp. (GHz)	Δ_{gs} calc (GHz)	T_1	T_2
SiV-	14	48	61	>1s (100mK) [19]	13ns [19]
GeV-	32	169	207	25us (2K) [50]	T2* 20ns [50]
SnV-	50	850	945	10ms (3K) [53]	0.3ms (1.7K) [54]
PbV-	82	4230	4385	unk.	unk

Table 2 – Modeled and measurement values for the ground-state splitting Δ_{gs} and spin relaxation and coherence times T_1 and T_2.

The group-IV defects neutral charge state is also just unraveling new exciting properties. Neutrally charge silicon-vacancy centers' spin S=1 showed by electron-spin resonance (ESR) [55] suggests more robustness to phonon-interactions, which should yield longer spin coherence times. Exciting results showed that the SiV^0 has a strong 90 % branching ratio in the ZPL with a short excited-state lifetime of 1.8 ns and a long T_1 time of 255 ms at 15 K [56]. It appears evident that charge state control could open perspectives for this class of defects, which was obtained by adding boron impurities during growth to get SiV^0 [56] or using a p-i-p junction around an SnV defect [44], or with optical charge control [57].

As one can see, the optical properties of group-IV defects showed promising optical properties. It appeared that the spin coherence times require low temperatures to levels of use for quantum information processing, which is not an excluding condition for such technologies due to the extended usage of cryostats. Additional quantum efficiency measurements are required to expand the scope of knowledge for these defects and better characterize the PbV centers. Finally, the neutral charge state could combine desirable optical and spin properties of such defects but needs further development in their deterministic fabrication.

2.3 THE GERMANIUM VACANCY CENTERS

The negatively charged GeV centers is the subject of focus of this work. Let us extract the main known properties from the previous section.

Z	ZPL λ (nm)	Δ_{gs} (GHz)	T_1	T_2^*	Exc. state lifetime (ns)	Debye-Waller	QE
32	602	207	25us (2K)	20ns	1.4-5.5	0.6	0.22

Table 3 - Negatively charged germanium vacancy centers physical properties.

The first investigation of GeV centers was by *Iwasaki et al.*(2015) [24]. They showed a spectrum with a strong branching ratio in the ZPL and proved it to be a single photon source by second-order correlation measurements. In 2017, the four optical transitions were unraveled, and a short excited-state lifetime was shown on transitions 1-3 by *Bhaskar et al.* [58]. At the same time, *Siyushev et al*. [50] extracted T_1 and T_2^* by doing optical and microwave control on spins. The following year, *Thiering and Gali* [37] released density functional theory (DFT) calculations on group-IV defects predicting the charge state stability, the spin-orbit and electron-phonon couplings, and spin Hamiltonian. The first evidence of spectral switching phenomena was mentioned by *Maity et al.* [59] with evidence of spectral jumps. *Chen et al.* (2019) [60] showed evidence of a dark-state and optical gating to trigger resonantly driven fluorescence. The quantum efficiency was estimated by *Nguyen et al.* [41] in 2020.

This short overview shows the interest of GeV centers and that additional measurements are required to fully understand this emitter, such as T_2 characterization, and experimental approach for extracting the QE, similar as in [31]. Recent works suggested linear and quadratic Stark shifts of SnV centers. Similar measurements on GeV centers would also be of interest.

Switching phenomena understanding is also an important aspect in the development of defects in diamond. A better understanding of their physical origins could improve fabrication processes or better external control to mitigate their importance.

2.4 GeV CENTERS DYNAMICS

Understanding the dynamics is essential to predicting and interpreting experimental results. The electronic structure of the germanium vacancy centers still has some unknowns. The existence of a dark state, and evidence of a metastable state was reported [60]. Therefore, the model equations relevant to this work's measurements will be listed and described for two and three levels systems.

The following sub-chapters were inspired by the book *Quantum Optics* by *Girish. S. Agarwal* [61] and *Daniel Allepuz Requena*'s thesis [62].

2.4.1 Two-level system dissipative dynamics

The results presented on this work were measured on GeV centers transition 1-3, at 4 K (see Fig.2), which is assumed to be a two-level system with the ground $|g\rangle$, and the excited states $|e\rangle$. The system if coherently driven by a continuous wave laser (CW).

Two-level Hamiltonian in the absence of interaction is:

$$H_0 = E_g|g\rangle\langle g| + E_e|e\rangle\langle e| \tag{2-2}$$

with E_g and E_e the energies for the ground and excited states. The zero-energy origin is set halfway between ground and excited states, $\widehat{H}_0$ is then expressed as:

$$\widehat{H}_0 = \frac{\hbar\omega_0}{2}(|e\rangle\langle e| - |g\rangle\langle g|) \tag{2-3}$$

where $\omega = (E_e - E_g)/\hbar$.

Let us consider an external electromagnetic field $\mathrm{E}(\mathbf{r}, t)$:

$$\mathrm{E}(\mathbf{r}, t) = \mathrm{E}_0 \mathrm{e}^{\mathrm{i}\mathrm{k}\cdot\mathbf{r} - \mathrm{i}\omega\nu_l t} + c.c. \tag{2-4}$$

Its interaction with the two-level system dipole $\hat{\mathrm{d}}$ is:

$$\widehat{H}_I = -\hat{\mathbf{d}} \cdot \mathbf{E}(\mathbf{r}, t). \tag{2-5}$$

or:

$$\widehat{H}_I = -\hbar\big(g|e\rangle\langle g|\mathrm{e}^{-\mathrm{i}\omega_l t} + \text{ H.c. }\big) - \hbar\big(g^*|e\rangle\langle g|\mathrm{e}^{\mathrm{i}\omega_l t} + \text{ H.c. }\big) \tag{2-6}$$

with $g = \frac{\mathrm{d}_{eg}\cdot\mathrm{E}_0}{\hbar}$

An approximation known as the rotating wave can be made by removing the time-dependence part of the Hamiltonian. These terms are negligible in resonant excitation experiment where $|g| \ll \omega_0$.The effective Hamiltonian of a dipole under a monochromatic field becomes:

$$\hat{H}_{\text{eff.}} = \hbar\Delta\hat{S}_z - \hbar\left(g\hat{S}_+ + g^*\hat{S}_-\right) \tag{2-7}$$

where $\Delta = \omega_0 - \omega_l$ is the field detuning and the introduced operators $\hat{S}_z, \hat{S}_+, \hat{S}_-$ are defined are as:

$$\hat{S}_z = \frac{1}{2}(|e\rangle\langle e| - |g\rangle\langle g|), \hat{S}_+ = |e\rangle\langle g|, \hat{S}_- = |g\rangle\langle e| \tag{2-8}$$

The Master equation describing the coherently driven two-level system can be formed by combining equation (2-8) to the dissipative master equation of a two-level system [61]:

$$\begin{gathered}\frac{\partial\hat{\rho}}{\partial t} = -i\left[\Delta\hat{S}_z - \left(g\hat{S}_+ + g^*\hat{S}_-\right), \hat{\rho}\right] \\ -\gamma_{\text{sp}}(1+n_0)\left(\hat{S}_+\hat{S}_-\hat{\rho} - 2\hat{S}_-\hat{\rho}\hat{S}_+ + \hat{\rho}\hat{S}_+\hat{S}_-\right) \\ -\gamma_{\text{sp}}n_0\left(\hat{S}_-\hat{S}_+\hat{\rho} - 2\hat{S}_+\hat{\rho}\hat{S}_- + \hat{\rho}\hat{S}_-\hat{S}_+\right) \\ -\gamma_{\text{pd}}\left(\hat{S}_z\hat{S}_z\hat{\rho} - 2\hat{S}_z\hat{\rho}\hat{S}_z + \hat{\rho}\hat{S}_z\hat{S}_z\right)\end{gathered} \tag{2-9}$$

where the $n_0 = 1/[\exp(\hbar\omega_0/k_BT) - 1]$ phonon number can be set to 0 for cold experimental temperatures such as used in this work, *2g* is the Rabi frequency, γ_{sp} is the spontaneous emission rate, and γ_{pd} is the dephasing rate.

The equations for the mean values of the inversion operator $\langle\hat{S}_z\rangle$, and the dipole moment operators $\langle\hat{S}_+\rangle$ and $\langle\hat{S}_-\rangle$ can be obtained from (2-9) and can take a compact matrix form*:*

$$\begin{gathered}\frac{\mathrm{d}\psi}{\mathrm{d}t} = M\psi + f \\ \psi = \begin{pmatrix}\langle\hat{S}_+\rangle \\ \langle\hat{S}_-\rangle \\ \langle\hat{S}_z\rangle\end{pmatrix}, f = \begin{pmatrix}0 \\ 0 \\ \eta/T_1\end{pmatrix}, M = \begin{pmatrix}\mathrm{i}\Delta - 1/T_2 & 0 & 2\mathrm{i}g^* \\ 0 & -\mathrm{i}\Delta - 1/T_2 & -2\mathrm{i}g \\ \mathrm{i}g & -\mathrm{i}g^* & -1/T_1\end{pmatrix}\end{gathered} \tag{2-10}$$

where T_1 is the relaxation time and T_2 is the coherence time, expressed by:

$$1/T_1 = 2\gamma_{sp}, \;\; 1/T_2 = \gamma_{sp} + \gamma_{pd} \tag{2-11}$$

2.4.2 Steady-state and saturation

The steady-state solution of (2-10) is reached in the limit $t \to \infty$, when $\frac{\mathrm{d}\psi}{\mathrm{d}t}$=0. The solution is:

$$\begin{gathered}\langle\hat{S}_z\rangle = \frac{(1 + (\Delta T_2)^2)\eta}{1 + (\Delta T_2)^2 + 4|g|^2T_1T_2}, \\ \langle\hat{S}_\pm)\rangle = \frac{-2\mathrm{i}g(-\mathrm{i}\Delta T_2 \mp 1)\eta}{1 + (\Delta T_2)^2 + 4|g|^2T_1T_2}\end{gathered} \tag{2-12}$$

For high drive fields, $\langle\hat{S}_z\rangle \to 0$. Therefore, the field equalize the ground and excited states populations. The saturation fluorescence intensity is proportional to the excited state population ρ_{ee}:

$$I_\infty \propto \rho_{ee}(\infty) = \frac{2|g|^2 T_1 T_2}{1 + (\Delta T_2)^2 + 4|g|^2 T_1 T_2} \tag{2-13}$$

The fluorescence saturation behavior in resonant excitation (Δ=0), (2-13) can be rewritten as follows:

$$I(P) = \frac{I_\infty P}{P_{sat} + P} + bP \tag{2-14}$$

Where I_∞ is the saturation fluorescence as $P \to \infty$. The saturation behavior is represented in Fig.3b. The second term is added as the background contribution to the signal, with a linear power dependence. It exists a relationship between the Rabi frequency $\Omega=2|g|$, and the power:

$$|g|^2 = \frac{1}{4T_1 T_2} \frac{P}{P_{sat}} \tag{2-15}$$

The spectral linewidth can also be extracted from (2-13) as we vary the detuning Δ to obtain a Lorentzian function (see Fig.3a), and to extract the following expression for the FWHM Δν :

$$\Delta\nu = \frac{1}{\pi T_2} \sqrt{1 + 4|g|^2 T_1 T_2} \tag{2-16}$$

At low excitation power, Ω→0 and we can extract the decoherence limited linewidth equal to $\frac{1}{\pi T_2}$.

2.4.3 Second-order correlation function

The second-order correlation function is an important expression of quantum emitters giving information about single-photon emission, or antibunching. Its general expression is:

$$g^{(2)}(\tau) = \frac{\langle I(t) I(t+\tau) \rangle}{\langle I(t) \rangle^2} \tag{2-17}$$

An important characteristic in a quantum emitter is the $g^{(2)}$ at 0-time delays. A criterion for single-photon emission is $g^{(2)}(0) < \frac{1}{2}$, that indicates antibunching.

For a stationary electric field, it can be written as:

$$g^{(2)}(\tau) = \frac{\left\langle \hat{\mathrm{E}}^-(\mathbf{r},t) \cdot \hat{\mathrm{E}}^-(\mathbf{r},t+\tau) \cdot \hat{\mathrm{E}}^+(\mathbf{r},t+\tau) \cdot \hat{\mathrm{E}}^+(\mathbf{r},t) \right\rangle}{\left\langle \hat{\mathrm{E}}^-(\mathbf{r},t) \cdot \hat{\mathrm{E}}^+(\mathbf{r},t) \right\rangle^2} \tag{2-18}$$

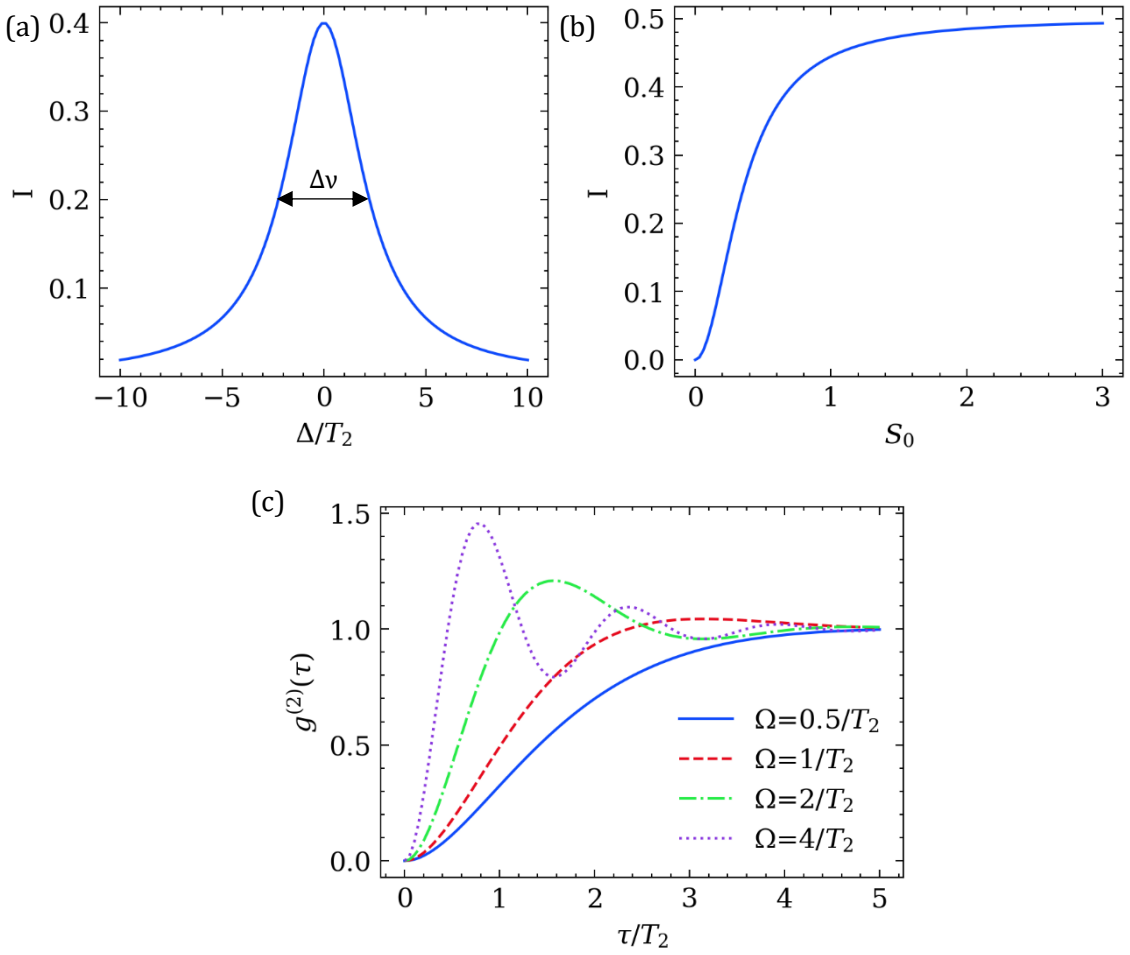

Figure 3 – (a) Intensity function with drive-field detuning, with T_1=T_2. (b) Saturation behavior when Δ=0, as a function of drive strength parameter S_0. (c) $g^{(2)}$ function for different drive intensities, with T_1=T_2. As the drive strength get smaller than the coherence time, oscillations appear with the Rabi frequency Ω.

where E is the electric field emitted by the dipole d, described by the operator:

$$\hat{\mathrm{d}}(t) = \mathrm{d}_{ge}^{*}\hat{S}_{+}(t)\mathrm{e}^{+\mathrm{i}\omega lt} + \mathrm{d}_{ge}\hat{S}_{-}(t)\mathrm{e}^{-\mathrm{i}\omega lt} \tag{2-19}$$

And the expression for E coming from an oscillating dipole emission:

$$\hat{\mathrm{E}}^{+}(\mathbf{r},t) = \hat{\mathrm{E}}_0^{+} - \frac{\omega_l^2}{c^2}\mathrm{n}\times\left[\mathrm{n}\times\mathrm{d}\left(t-\frac{|\mathbf{r}|}{c}\right)\right]\frac{\mathrm{e}^{\mathrm{i}k_l\mathbf{r}-\mathrm{i}\omega_l t}}{|r|} \tag{2-20}$$

For a coherently driven two level system, it can be shown that the $g^{(2)}$ function becomes (see ref. [62] for full derivation):

$$g^{(2)}(\tau) = 1 - \mathrm{e}^{-\frac{\tau}{2}\left(\frac{1}{T_1}+\frac{1}{T_2}\right)}\left[\cos(\alpha\tau) + \frac{T_1+T_2}{2T_1T_2\alpha}\sin(\alpha\tau)\right],$$
$$\text{with } \alpha = \frac{1}{2}\sqrt{16|\frac{\Omega}{2}|^2 - \left(\frac{1}{T_1}-\frac{1}{T_2}\right)^2} \tag{2-21}$$

When T_1 and T_2 are greater than Ω, Rabi oscillations are visible on the correlation function, as shown in Fig.3c.

2.4.4 Three level systems

As mentioned in Ch.2.3, *Chen et al.* showed evidence of a dark state in GeV centers [60]. In this situation, the dark state is not driven coherently, but by non-resonant excitation, thermalization or multiple photon absorption processes. A new master equation was proposed with a dark state as a third level, which can be accessed by the ground and excited states, defined with the rates k_{gd}, k_{dg}, and k_{ed}. They did not include a transition from the dark to the excited state, and also excluded thermalization processes.

$$\frac{\mathrm{d}}{\mathrm{d}t}\begin{pmatrix}\rho_{gg}\\ \rho_{ge}\\ \rho_{eg}\\ \rho_{ee}\\ \rho_{dd}\end{pmatrix}=\begin{pmatrix}-2\gamma_{\mathrm{sp}}n_0-k_{gd} & -\mathrm{ig} & \mathrm{ig}^* & 2\gamma_{\mathrm{sp}}(n_0+1) & k_{dg}\\ -\mathrm{ig}^* & \mathrm{i}\Delta-1/T_2 & 0 & \mathrm{ig} & 0\\ \mathrm{ig} & 0 & -\mathrm{i}\Delta-1/T_2 & -\mathrm{ig} & 0\\ 2\gamma_{\mathrm{sp}}n_0 & \mathrm{ig} & -\mathrm{ig}^* & -2\gamma_{\mathrm{sp}}(n_0+1)-k_{ed} & 0\\ k_{gd} & 0 & 0 & k_{ed} & -\rho_{gg}\end{pmatrix}\begin{pmatrix}\rho_{gg}\\ \rho_{ge}\\ \rho_{eg}\\ \rho_{ee}\\ \rho_{dd}\end{pmatrix} \tag{2-22}$$

where the parameters are similar to as in the two-level system model. Similarly as in 2.4.2, the steady-state solution can be derived to obtain [60]:

$$I^{3-\,\mathrm{level}}\propto\rho_{ee}^{3-level}(\infty)=\frac{1}{2}\frac{k_{dg}}{k_{dg}+k_{gd}}\left[\frac{(\Delta^2+T_2^{-2})(k_{ed}+T_1^{-1})}{4|g|^2T_2^{-1}}+\frac{1}{2}\left(1+\frac{k_{ed}+k_{dg}}{k_{dg}+k_{gd}}\right)\right]^{-1} \tag{2-23}$$

And the linewidth Δν can also be derived from (2-22) by varying the detuning Δ:

$$\Delta\nu=\frac{1}{\pi T_2}\sqrt{1+\frac{2|g|^2T_2}{T_1^{-1}+k_{ed}}\left(1+\frac{k_{ed}+k_{dg}}{k_{dg}+k_{gd}}\right)} \tag{2-24}$$

2.5 NONCLASSICAL STATES OF LIGHT

This section was written with the help of *Lukáš Lachman*, in preparation of the manuscript: *Analysis of hBN and GeV using dual correlation functions* α *and* β.

2.5.1 Motivation

Emission of single photons is an important aspect of many different quantum computing and communication application. The Hanbury-Brown and Twiss (HBT) interferometer depicted in Fig.4 is the most commonly used setup to test single photon emission by determining the second-order correlation function introduced in Ch.2.4.3. In the setup, a photons flow impinges a beam splitter dividing the light into two path and detected by two single-photon avalanche photodiodes (SPADs) detectors. The cross-correlation between the two detectors' signals is extracted and the $g^{(2)}$ function can be extracted to get the single photon emission criterion where $g^{(2)}(0)<1/2$. This method finds some limitation in experiment where the quantum system's transition is pumped with a coherent light source scattering light to the detectors and deteriorating the photons statistics [63]. Therefore, alternative methods are being investigated to get around this issue.

2.5.2 Nonclassical light

Laws of electromagnetism allow to describe classical optics phenomena that we can witness with simple experiments, e.g., Young's double slit interference experiment. An important consideration is the Poissonian photons statistics of classical states of light where $\Delta n^2 = \langle n \rangle$. However, the classical description of light was found to be incomplete to explain some corpuscular aspect of the thermal radiation. The classical coherence of quantum systems was explained by *R. Glauber* and *G. Sudarshan* in 1963 [64–66]. It gave an explanation on why

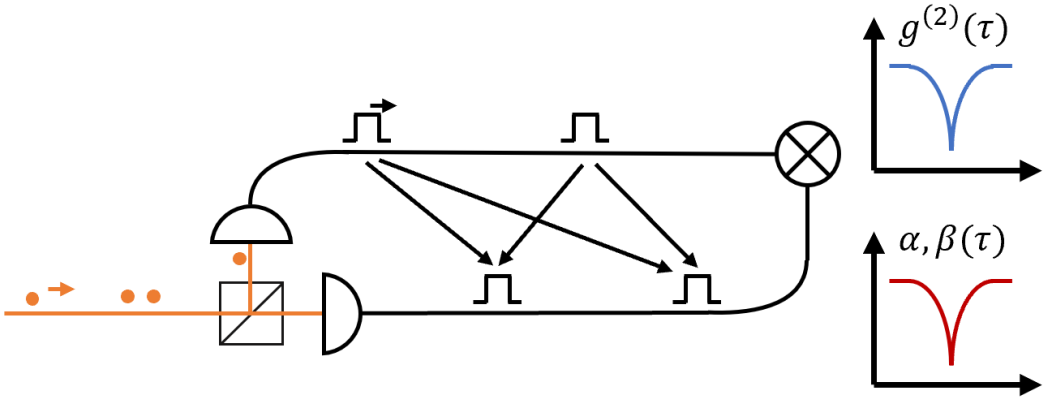

Figure 4 – Hanbury-Brown and Twiss interferometer allowing to do second-order correlation measurement $g^{(2)}$ or alternatively, determine the nonclassicality parameters α and β.

classical interference experiments were reproducible with single quantum photons by measuring the intensity.

A new quantum theory of light was born, and new experiments such as second-order correlation function on the emission of a quantum emitter showing single photon antibunching with an HBT interferometer [67], or the observation of squeezed states of light [68] only find explanation in a nonclassical form. Such states of light can have sub-Poissonian statistics, $\Delta n^2 < \langle n \rangle$.

Measurement of nonclassical states, e.g., squeezed states, can require complex experimental setup such as homodyne detectors to map out the quadrature of a 2-level system [69]. Alternatively, the HBT interferometer has been proposed to extract sub-Poissonian photons statistics and overcome the shot-noise limit of the second-order correlation functions obtained with such setup [70,71].

2.5.3 Nonclassicality parameters

In the proposed approach, the photons statistics coming from a quantum emitter is recorded using an HBT interferometer. Each photons impinging either of the detectors is saved with a time-tag, to determine precisely when it hit the sensing cell.

Formally, the nonclassicality of state ρ is defined by the inequality

$$\rho \neq \int \mathrm{d}^2\alpha P(\alpha)|\alpha\rangle\langle\alpha| \tag{2-25}$$

with $|\alpha\rangle$ being the coherent state and P being a density probability function of the amplitude α.

Let us define the click statistics P_1 is to probability of having a click in either of the detectors, regardless of the other. $P_{11}(\tau)$ is the double-click probability, when both detectors record an event in the same time bin. The probability $P_{00}(\tau)$ is the no-click events in neither of the channels, and P_0 is the combined no-click probability of each channel ($P_0 = \sqrt{P_{01} \cdot P_{02}}$). The following identities can be written from the introduced statistics:

$$\begin{aligned} P_1 &= 1 - P_0 \\ P_{11}(\tau) &= 1 - 2P_0 + P_{00}(\tau) \end{aligned} \tag{2-26}$$

Two correlations functions are now introduced utilizing the no-clicks and clicks probabilities, $\alpha(\tau)$ [71] and $\beta(\tau)$ [70], respectively:

$$\alpha(\tau) = \frac{P_{11}(\tau)}{P_1^2} \tag{2-27}$$

$$\beta(\tau) = \frac{P_{00}(\tau)}{P_0^2}$$

Note that β is referred to the parameter d used in [70], where $\beta = 1/(1+d)$.

This dual approach has the advantage that both parameters behave differently to the loss in the channel and the Poissonian background of a measured state ρ, defined by a simplified model:

$$\rho = [(1-\eta T)|0\rangle\langle 0| + \eta T|1\rangle\langle 1|\,]\otimes\rho_{T\bar{n}} \tag{2-28}$$

where T is transmission through a lossy channel, $\rho_{\bar{n}}$ is a Poissonian noise background with a mean number of photons $\bar{n}$, and η is the single photon emission efficiency. The losses have an impact on the parameters η and $\bar{n}$ by reducing them. The temporal evolution is not considered in the simplified model. Hence, for $\eta \ll 1$ and $\bar{n} \ll 1$:

$$\alpha \approx \frac{(1\eta\,\bar{n} + \bar{n}^2)}{(\eta + \bar{n})^2}$$
$$\beta \approx 1 - (\eta T)^2/4 \tag{2-29}$$

We can see that α is independent of T but increases with $\bar{n}$ and β is independent of $\bar{n}$ and increases with T, regardless of Poissonian background [72]. Finally, it has been proven that the criteria $\alpha<1$ or $\beta<1$ certifies nonclassicality [70,71].

2.6 FABRY-PÉROT MICROCAVITY

Optical cavities are used in many applications. Most notable in lasers. Inserting a defect in diamond inside an optical cavity can improve the optical properties like the branching ratio into the ZPL and shorten the lifetime. Furthermore, collection efficiency can be improved by guiding the emission into well-defined mode. This section will outline the theory behind optical cavity and the coupling to a two-level system.

This discussion draws inspiration from the PhD thesis by *Erika Janitz* and *Rasmus Jensen* [73,74].

2.6.1 Optical cavity

An optical Fabry-Pérot cavity is composed of two reflecting surfaces facing each other, as illustrated in Fig.5a. When light is coupled in, it acts as a resonator with specific wavelengths that fulfill the condition $\lambda_{0_m} = \frac{2nL}{m}, m \in \mathbb{N}$. Only then, constructive interferences will occur between the waves resonating inside the cavity. A Fabry-Pérot cavity is characterized by its length L and the reflectivity of both mirrors, R_1, and R_2. The length will determine the free-spectral range (FSR), corresponding to $FSR_\nu = \frac{c}{2nL}$, and the reflectivities will give the cavity Finesse:

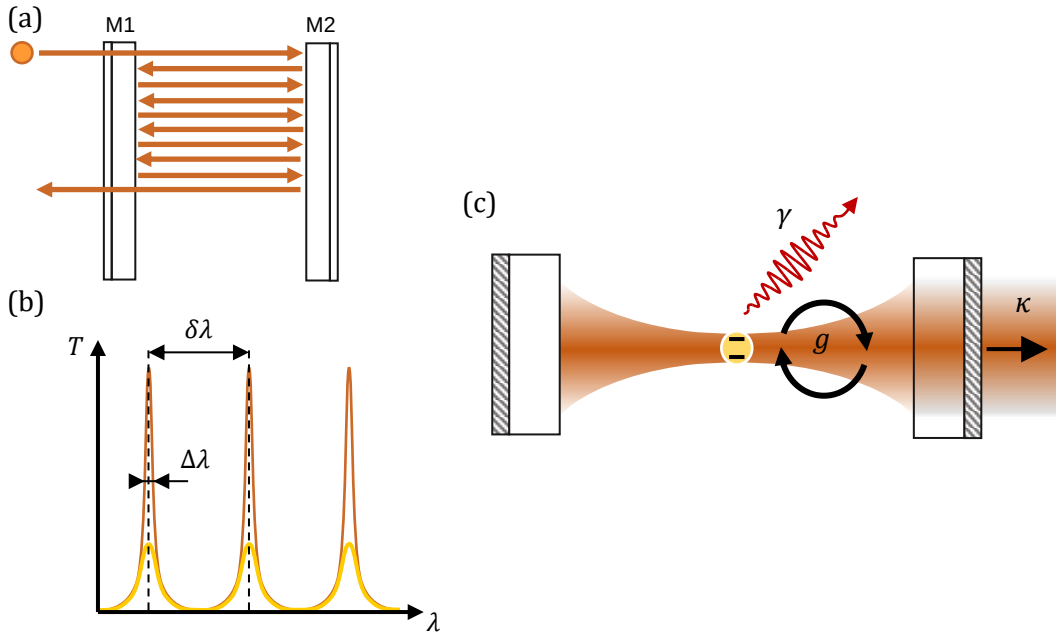

Figure 5 – (a) Illustration of a plano-parallel Fabry-Pérot cavity with photons bouncing back and forth between the two mirrors. (b) Transmission intensity spectrum for a low-Finesse (yellow) and high-Finesse (orange), where δλ is the FSR and Δλ the linewidth.(c) Illustration of the Jaynes-cunning model with an atom coupled to the field mode of the cavity at a rate g. The 2-level system has decay rate γ and photons leaks out of the cavity at rate κ.

$$\mathcal{F} = \frac{FSR}{FWHM} = \frac{\delta\lambda}{\Delta\lambda} = \frac{\delta\nu}{\Delta\nu} = \frac{2\pi}{-\ln(R_1 R_2)} \tag{2-30}$$

where Δν, Δλ, is the full width at half-maxima FWHM in frequency and wavelength, respectively(see Fig.5b). Another cavity property of an optical cavity is the quality factor Q, which is closely related to the Finesse and the cavity length:

$$Q = \frac{\nu_0}{\Delta\nu} = \frac{2L}{\lambda}\mathcal{F} \tag{2-31}$$

The cavity's transmission coefficients increase up to 100 % in resonance, letting optical waves go through the mirror interfaces.

2.6.2 Purcell enhancement

Fermi's golden rule describes the emission rate between two states:

$$\gamma = \frac{2\pi}{\hbar^2} D(\omega)|M|^2 \tag{2-32}$$

where $D(\omega)$ is the optical density of states and M is the transition matrix element. For a free-space emission, it can be shown that:

$$D(\omega) = \frac{\omega^2 V}{\pi^2 \left(\frac{c}{n}\right)^3} \tag{2-33}$$

$$M^2 = \frac{\mu^2 \hbar\omega}{6\epsilon_0 V} \tag{2-34}$$

where μ is the dipole moment and V is the mode volume. Hence, the free space emission rate is:

$$\gamma_{free} = \frac{\mu^2}{3\pi\hbar\epsilon_0}\left(\frac{\omega n}{c}\right)^3 \tag{2-35}$$

In cavity quantum electrodynamics CQED, the two-level system quantum emitter is inside a cavity. When the maximal electric field is considered, and the field is coherently driven, the optical density of states and the transition matrix are:

$$D(\omega) = \frac{2Q}{\pi\omega} \tag{2-36}$$

$$M^2 = \frac{\mu^2 \hbar\omega}{2\epsilon_0 V} \tag{2-37}$$

The emission rate into the cavity mode becomes:

$$\gamma_{cav} = \frac{2Q\mu^2}{\hbar\epsilon_0 V} \tag{2-38}$$

We can compare the change in rates between free-space and cavity emission:

$$F_P = \frac{\gamma_{cav}}{\gamma_{free}} = \frac{3Q(\lambda/n)^3}{4\pi V} \quad (2\text{-}39)$$

An enhancement in emission rate is observed relative to the cavity quality factor and mode volume, also known as the Purcell factor.

One can see the significant interest in embedding a quantum emitter in a cavity. Enhancing the emission rate enables faster communication and processing. Diverse photonic solutions exist and are investigated for diamond-based emitters. They will be discussed in the following section.

2.6.3 Integrated cavity design

A lot of effort was put into embedding color centers in optical cavities to enhance the emission rate. Two ways of proceeding can be defined: open cavities and photonic resonators.

Open cavities are usually represented with a plano-parallel geometry (see Fig.6a). This model was excluded from most approaches, as the stability regime is hardly achieved. Therefore, the hemispherical geometry was favored for most of the solutions, where at least one of the mirrors is concave (see Fig.6b). To obtain small mode volumes, short radii of curvatures are needed, which are often obtained by etching using a focused ion beam (FIB) [75] or using laser ablation techniques [76]. To reach high Finesses, distributed Bragg reflectors (DBR) are deposited on both interfaces. These coatings also enable wavelength tunability for the reflection and transmission coefficients, which is an essential feature for quantum information technologies where different quantum emitters have different resonant wavelengths.

Different substrates were employed as an etching base for the concave mirror of an hemispherical cavity geometry. Commonly, one of the mirrors is kept flat to place a thin diamond membrane on it. *Riedel et al.* [77] achieved a 4.7 Purcell enhancement of the diamond Raman emission line using two flat mirrors, having a cavity factor Q of 8200. However, this approach can be limited by the interface tilt for large mirrors. Therefore, a favored method is to use a fiber-tip as the concave mirror, which allows more freedom of positioning closer to the flat interface, as illustrated in Fig.6c. Using this method, F_P of 1.9-9.2 was reached at room temperature on SiV centers with up to 90 % coupling in the fiber side [78,79]. A remarkable 32-fold photon emission enhancement was obtained using a similar design for GeV centers [80]. To date, only one measurement reported on Purcell enhancement of a group-IV defect (SiV^-) at cold temperatures (4 K), where F_P of 0.075 was achieved using a bath cryostat [81]. The main challenges of this approach come in the experimental control and sample fabrication. Indeed, to achieve full tunability, the two

mirrors are mounted on nano-positioners requiring complex active controls, that can induce mechanical vibrations translating into instability in the cavity mode. In addition, cryostats often use cold Helium flow circuits, bringing additional vibrations to the system, requiring several isolating stages [82]. Finally, inserting a thin diamond membrane in the cavity changes the cavity mode, and optimal design in DBR coatings, membrane thickness, and defects implantation depth need to be considered to maximize the light-matter interaction leading to a Purcell enhancement [83].

Alternatively, photonic resonators are serious contenders to the open cavities systems. Both approaches have antinomical properties. Photonic resonators offer perfect mechanical stability but suffer from cavity zero-tunability. Nanoring resonators coupled to GeV centers showed a Purcell enhancement of ~4 [21], and more efforts have been concentrated on photonic crystal cavities. Interestingly, nanodiamonds were coupled to a Si_3N_4 photonic crystal, with the diamond positioning using an atomic-force microscope (AFM), reaching fluorescence enhancement of ~4 [22]. Development of new ICP-RIE recipes enabled fabricating directly in bulk diamond substrates. *Riedrich-Möller et al.* even suggested a post-processing method to tune the cavity mode to a SiV center, reaching an F_P of 2.8 [84]. Other results with SiV centers got Purcell factors up to 28 [39,85] and 37 for SnV centers [86,87].

An open-cavity design is proposed in this work, using a bath cryostat to limit vibrational noise. The stability measurement of the existing setup is discussed in Ch. 8.

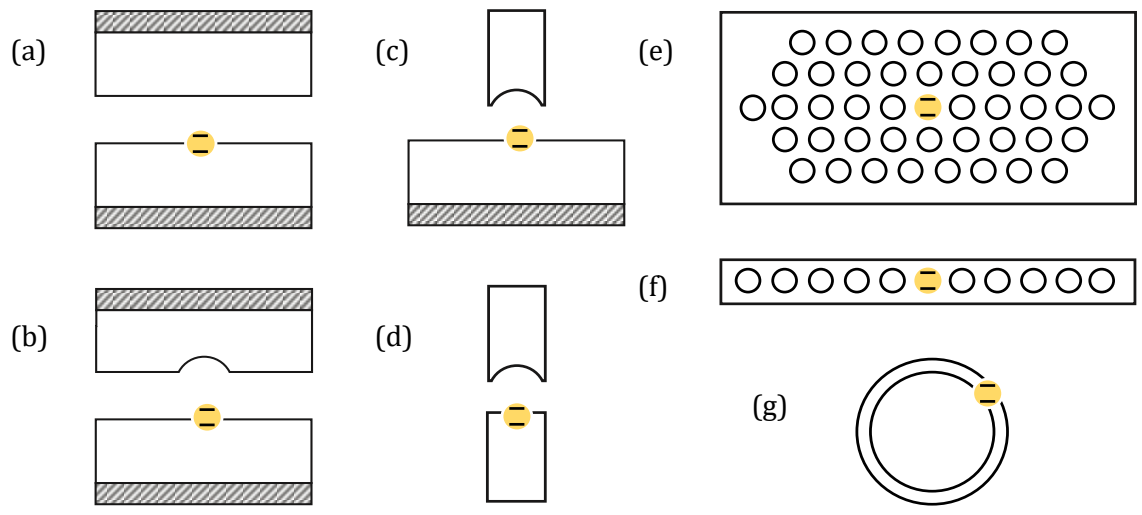

Figure 6 – Different cavity designs with embedded quantum emitters. (a) Plano-plano geometry. (b)(c)(d) Hemispherical geometry, with a dimple etched on a planar mirror (b), a fiber-tip (c), and with both interfaces on fibers (d). (e) Photonic crystal cavity in a bulk substrate (e), embedded in a nanobeam waveguide (f). Nanoring photonic resonator(g).

CHAPTER 3

SAMPLE FABRICATION

This chapter reviews the different fabrication methods in diamond-based research regarding their growth, defects incorporation, and processing. A detailed description of the parameters and methods employed for the sample used in this work will be detailed for each step.

3.1 DIAMOND PHOTONICS

A great dormant knowledge regarding diamond physics existed from the jewelry industry, which conducted considerable research from the 1950s regarding their optical properties and lab growth processes. Their motivations being far from today's, they skimmed this field considerably to give a good physical ground at the dawn of the second quantum revolution. Since then, diamond photonics has been substantially growing over the last decade, following the revelation of optical properties of great interest in the NV centers, such as long-lived spin coherence and addressable spin states [28,30]. It rapidly appeared that fabrication processes greatly impacted their optical and electronic properties [88]. Tremendous efforts have been put into optimizing each step to compete with other candidates for QIP technologies such as trapped ions, quantum dots, and superconducting qubits.

3.2 SAMPLE FABRICATION

The different steps of the fabrication process are described in the next subsections and illustrated in Fig.7.

3.2.1 Diamond growth

Naturally formed diamonds are formed in exceptional conditions of high pressure and high temperature through geological processes. It was logical that the first synthesis method reproduced similar thermodynamical conditions of high-pressure, high temperature in press cells [89]. This method allows the growth of larger volumes of polycrystalline diamonds, which can limit the control over defects implantation. On the other hand, CVD (chemical vapor deposition) allows the production of monocrystalline bulk diamond, which enables further machining and tailoring of the material. The advantage of HPHT over CVD growth process lies

in the ion incorporation step, which we will show can bring complications in the latter technique.

Diamond suppliers offer various properties for both HPHT and CVD growth processes regarding purity and crystalline structures, affecting their optical, mechanical, and thermal properties.

[1]The product used in this work is an <100>-cut electronic grade CVD grown diamond 0.5 mm thick bulk sample from Element6. This grade announces a high monocrystalline purity with a nitrogen impurities concentration of <5 ppb. The sample was sent for laser slicing (Delaware Diamond Knive) to reduce the thickness to ~20 μm to reduce the RIE etching time. [73]

3.2.2 Ion incorporation

Direct incorporation of defects during CVD growth has been shown for NV and SiV centers where preferential direction along the diamond <111> axis [90–92]. This process requires dedicated deposition machines to avoid contamination from residues inside the chamber [34].

More commonly, the defects are implanted using ion implantation methods with particles' accelerators. SRIM simulations [93] allow for determining the defects concentration and implantation depth. The depth is essential in open-microcavity with distributed Bragg reflectors (DBR), where the termination layer refractive index will determine the first electric-field antinode's position in the diamond [83].

The sample was implanted with a 250 keV implantation energy, yielding an average implantation depth of 125 nm, or $\lambda/4n_d$. The fluence of $5{\cdot}10^9$ ions·cm^{-2} gives the defects concentration. The conversion factor will be measured in Ch.5.

3.2.3 Annealing

Defects incorporation via ion implantation process generate a considerable number of vacancies when releasing energy during the deceleration. Simulations showed that a 250 keV germanium ion penetrating a diamond bulk sample leaves on average ~1500 vacancies on its way through the crystal (see SRIM simulation, Ch.6.2).

The process consisted of three steps of annealing at 400 (4 hours), 800 (2 hours), and 1200 °C (2 hours), a recipe that demonstrated to improve the spectral distribution in NVs [88]. Each

[1] Additional information about the fabrication processes and recipes can be found in *Erika Janitz*' thesis [73], Ch.1.4.

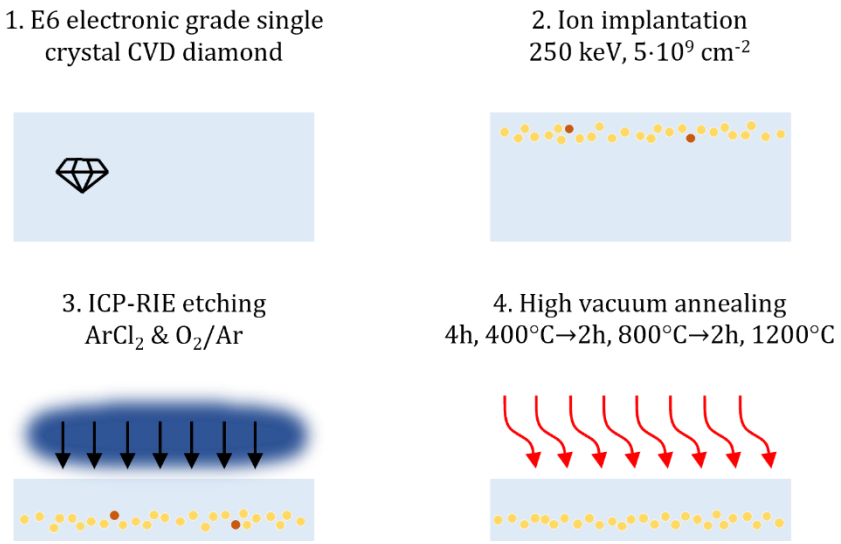

Figure 7 – Different steps of the fabrication process with 1. bulk diamond sample, 2. germanium ions implantation. 3. inductive couple plasma reactive ion etching (ICP-RIE) and 4. high temperature annealing.

step plays a role in the defects formation and in the vacancy diffusion [94]; The first step allows the migration and annihilation of interstitial implanted ions with vacancies, the second enables the mobility of vacancies and the formation of M-V centers, and the last step triggers the mobility of additional defects (divacancies, sp^2 type defects, hydrogen, remaining paramagnetic defects). A high vacuum was maintained throughout the process in the furnace chamber to reduce the graphitization of the diamond's surface due to residual gases.

Despite the high vacuum, a thin graphitized layer was formed and was etched in a Tri-acid bath.

Finally, a subsequent 465 °C O_2-atmosphere annealing was done to remove sp^2-hybridized carbon and leave a cleaner surface termination.

3.2.4 Etching/polishing

Before annealing, the ion implantation side was etched and polished using an ICP-RIE recipe to reach low surface roughness. After annealing, the back side was similarly etched/polished using the same recipe to obtain a smooth surface and get the desired membrane thickness. A thickness of ~1.5 μm was obtained to have an open diamond-air cavity air-like mode. Surface texture is critical to limit the scattering loss in the cavity, and a σ = 0.3 nm-rms roughness was obtained with the ICP-RIE recipe.

3.3 Sample summary

This table summarizes the resulting sample parameters:

	Results	Info/Source
Reference	MGEV2	McGill
Diamond	CVD monocrystalline electronic grade	Element6 [95]
Implantation dose	$5 \cdot 10^9$ ions·cm^{-2}	250 keV SRIM [93]
Implantation depth	~125 nm ($\lambda/4n_d$)	
Annealing	4h @ 400 °C →2h @ 800 °C →2h @ 1200 °C	*Chu et al.* [88]
Thickness	~1.5 μm	$ArCl_2$ & O_2/Ar ICP-RIE [73,96,97]
Surface roughness	0.3 nm-rms	

Table 4 - Sample summary with different fabrication parameters and results.

3.4 DISCUSSION

Recent works proposed an alternative annealing approach. A high-pressure and high-temperature annealing was applied after conventional tin [8,16] or lead [20] ion implantations in CVD single crystal diamonds. Temperatures up to 2100 C and pressure of 7 GPa were reached using an original belt-type high-pressure apparatus in CsCl atmosphere [98]. The high-pressure prevented graphitization from high-temperature annealing, which suppresses inhomogeneous broadening due to surrounding defects and strain.

CHAPTER 4

EXPERIMENTAL SETUP

All the measurements presented in this work were performed with a homemade confocal microscope setup with a cryogenic cooling chamber. Two different light sources enable the germanium vacancy centers' off resonant and resonant excitation. The sample lies inside a closed-cycle cryostat on piezo actuators to do fluorescence mapping and get a spatial selectivity of the emitters and a heat-plate to heat the sample in temperatures ranging from 4 to 300 Kelvin. A cross-polarization scheme allows the detection path to reject up to 66 dB of excitation light and collect photons emitted from the zero-phonon line (ZPL) and the phonon-sidebands (PSB). A single-mode (SM) fiber is used as a confocal spatial filter to perform high-resolution imaging of the emitters. Finally, the collected photons are sent into a single photon avalanche diode (SPAD), a Hanbury-Brown and Twiss (HBT) interferometer, or a spectrometer to do the adequate measurement.

The following chapters will present the experimental setup in detail. The lenses employed for collimation and focusing were selected assuming a perfect Gaussian beam using the following expression [99]:

$$2w_0 = \frac{4\lambda f}{\pi D} \tag{4-1}$$

Where, $2w_0$ is the beam diameter at focus ($1/e^2$), λ is the wavelength, f is the lens focal distance, and D is the beam diameter at the lens.

4.1 CONFOCAL MICROSCOPE

Fig. 8 presents the experimental optical setup. The continuous wave (CW) resonant 602 nm wavelength beam is generated with a sum-frequency-generation (SFG) crystal module (NTT Electronics). To reach the desired 497.993 THz (602 nm) frequency laser output, the SFG module requires 312.936 THz (958 nm) and 185.057 THz (1620 nm) laser frequencies as pump wavelengths. A 1620nm single-frequency-laser (Thorlabs SFL1620s, $\Delta\nu = 10$kHz) and a continuously tunable laser (Toptica CTL950, $\Delta\nu < 10$kHz). The latter has a 57 GHz mode-hop-free piezo fine-tuning range to align to the emitters' energy levels and perform laser scans. Phase-matching is essential to optimize the SFG module efficiency and is obtained with

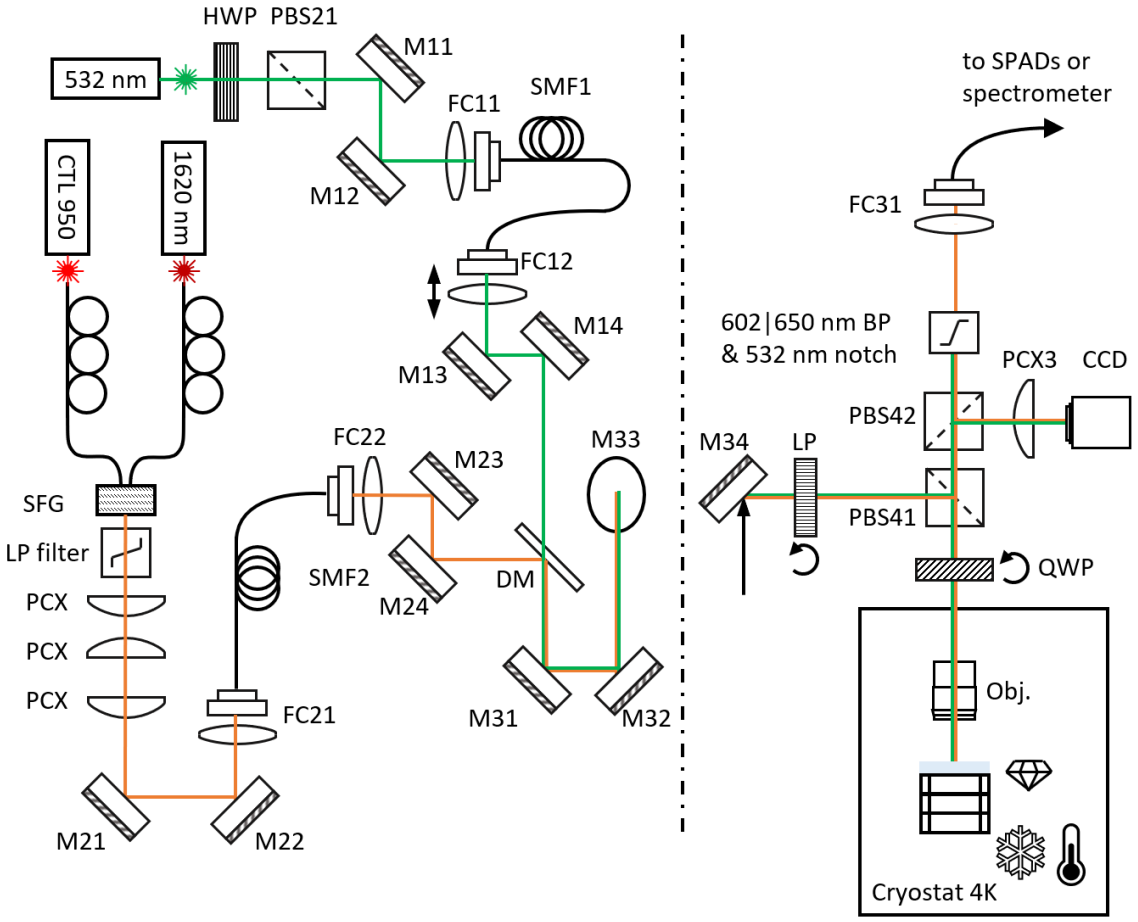

Figure 8 – Confocal optical setup scheme used for GeV⁻ characterization. (CTL) Continuously Tunable Laser. (SFG) Sum-Frequency Generation. (LP) Low-Pass filter. (PCX) Plano-convex lens. (M) dielectric Mirror. (FC) Fiber-Coupler. (HWP). Half-Wave Plate). (PBS) Polarizing Beam-Splitter. (DM) Dichroic Mirror. (LP) Linear Polarizer. (QWP) Quarter-Wave Plate. (Obj.) Objective lens. (CCD) Charge-Couple Device camera. (BP) Band-Pass filter. (SPAD) Single Photon Avalanche Detector.

temperature control accordingly to the desired wavelength (Wavelength Electronics LFI3751). The SFG free-space output frequency is characterized by a laser-spectrum analyzer (HighFinesse, resolution 1 GHz). Finally, the output mode is spatially cleaned by a single-mode fiber (Fig.8, SMF2) and outcouple to produce a ~4 mm diameter collimated Gaussian beam using an 18.4mm aspheric lens (Fig. 8, FC22, Thorlabs A280TM-A). The maximum output power is ~5 mW.

The 532 nm laser beam (CNI Lasers, MSL-S-532) is used for off-resonant excitation and confocal imaging. The power output is controlled with a rotating half-wave plate (HWP) and a polarizing beam-splitter. Equivalently as for the 602 nm beam, the mode is cleaned through a SM fiber (Fig.8, SMF1). The collimation lens is mounted on a Z-translation stage to compensate for chromatic aberration induced by the aspheric objective lens inside the cryostat.

The two beams are combined with a dichroic beam-splitter (Thorlabs, DMLP550R) and directed by a PBS to the cryostat. The objective lens (Thorlabs, C330TMD-A, $f = 3.1$, 0.7NA) focuses the beam to an excitation diameter of ~600 nm on the sample. The latter is mounted on a Z-actuator (Attocube, ANPz102) to adjust focus.

The objective lens clear aperture collimates the fluorescence photons emitted by the sample to a collection beam diameter of 3.84 mm. Interchangeable bandpass filters allow the collection of photons from the ZPL (Semrock FF01-605/15, OD>5) or PSB (2x Edmund Optics, 650±25nm OD4). An additional notch filter (Semrock NF01-532U-25) suppresses light from the 532 nm excitation beam.

The role of the following polarization optics elements; linear polarizer (LP), PBS41, and QWP, in the excitation beam rejection will be developed in Chapter 4.3.2.

Finally, the ZPL or PSB photons are coupled into a SM fiber (Thorlabs SM450) with a mode field diameter of ~5 μm at 602 nm with an aspheric lens (Thorlabs, A280TM, 0.15NA), reaching a ~45 % coupling efficiency at 602 nm and ~37 % at 637 nm.

An imaging system (Imagine Source,) collects a fraction of the light at the second PBS (PBS42) and is used to align focus and concentricity.

4.2 CRYOGENIC SETUP

A Gifford-McMahon (GM) closed-cycle cryostat (Attocube, attoDRY800) is used to cool the sample to temperatures down to 4 Kelvin (Fig.9a). The total cooldown (including pumping) takes approximately 6 hours, as shown in Fig.9b). Attocube provides the following instrument vibration stability [100]:

Direction	Peak-to-Peak @200 Hz (1500 Hz)	RMS @200 Hz (1500 Hz)
vertical	3 nm (4 nm)	1.0 nm (1.1 nm)
horizontal	2 nm (17 nm)	0.6 nm (2.1 nm)

Table 5 –AttoDRY800 vibrational stability measurement values for two bandwidths, 200 and 1500 Hz, showing displacement of ~1-2 nm RMS. The measurements were taken using an interferometric method on the cold plate. Table reproduced from [100].

The principal sources of vibrations come from the rotary valve, and the liquid Helium flow through the high and low-pressure lines.

The vacuum shroud has wedged uncoated glass windows on the top and the four sides to allow free-space optical access to the sample chamber. The sample is mounted inside the thermal shield with homemade clamps on a piezo stack, including XYZ positioners (Attocube,

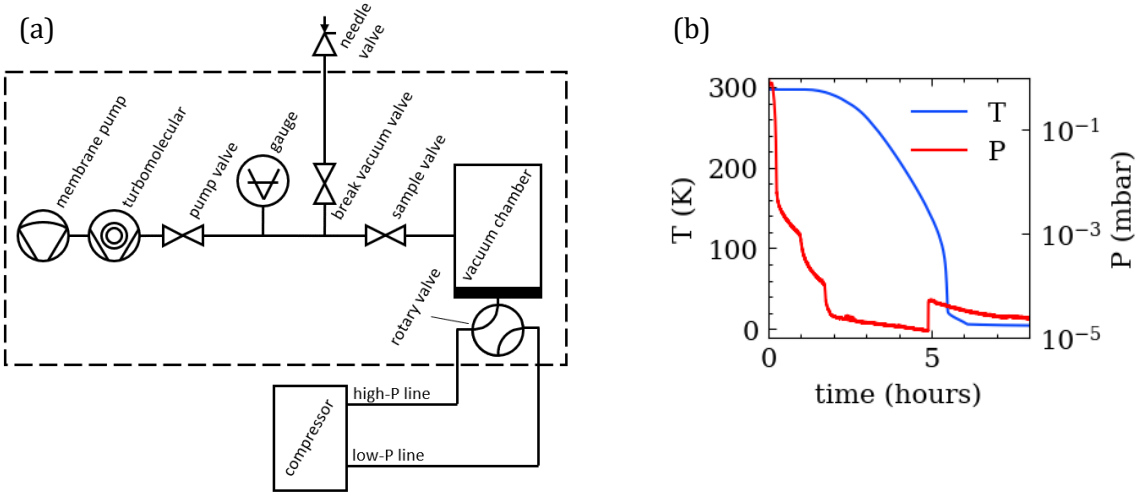

Figure 9 – (a) AttoDRY800 pump diagram. (b) Sample chamber cooldown curve. The sudden temperature drop at ~100 Kelvin originates from the cooling sequence switch between liquid Nitrogen to liquid Helium starting.

ANPx51/RES/LT), XY scanners (Attocube, ANSxy50/LT), and a heat-plate. The positioners have a 5 mm course range for coarse positioning and focal-plane adjustment. The scanners are used for confocal imaging emitters selection and have a 30 μm scanning range.

The objective lens is mounted to the thermal shield with a homemade mount to limit undesired effects from thermal shrinking on optical properties such as birefringence.

4.3 COLLECTION

Collecting from the ZPL is crucial for generating indistinguishable single photons with a high degree of coherence. The group-IV defects strong emissions in the ZPL, making it even more important for integrating into a scalable quantum network. However, a technical challenge occurs with a resonant excitation scheme; both wavelengths from the excitation beam and the fluorescence signal from the quantum emitter are the same. Since the scattered light from the laser is much stronger than the fluorescence, it is necessary to find methods to filter it out.

Spectral filtering is employed for PSB detection resonant excitation or ZPL detection off-resonant excitation, where commercial filters can be used. However, other methods have to be used for resonant excitation ZPL detection as emission and collection beams have the same wavelength.

Spatial filtering is widely employed in techniques such as dark-field microscopy. Excitation and fluorescence signals take different optical paths, which offers the possibility of rejecting the illumination beam. Nanophotonics engineering can achieve alternative spatial filtering, where guiding the fluorescence photons to nanobeam waveguides can separate both fluxes.

In diamond optics, however, cumbersome fabrication processes hinder the widespread usage of this approach. Therefore, polarization filtering could be a viable option as it requires simpler commercial polarizing optical components.

4.3.1 Cross-polarization extinction

Cross-polarization filtering consists of discriminating a linearly polarized excitation beam by expecting it to go back to the same path it came from, using polarizing optical components. Hence, fluorescence photons scattered with another polarization state will take another path, as pictured in Fig.11.

It has been shown that a linearly polarized light beam reflected on Silver, dielectric high-reflective, and gold film mirrors induces in a small shift, or "leakage," in the polarization angle, in the order of ±1 deg. This gives understanding about compensation to be made.

Another phenomenon occurs, allowing an extreme extinction ratio. A polarized Gaussian beam propagates along $\vec{k}_0$ with an angular distribution $\vec{k}_0/k_0 = u\vec{p} + v\vec{s} + w\vec{k}_0/k_0$:

$$\vec{E}_{0uv} = \frac{E_0}{4\theta_0^2} e^{-\left(\frac{u^2+v^2}{\theta_0^2}\right)} \begin{bmatrix} cos\beta \\ sin\beta \end{bmatrix} \tag{4-2}$$

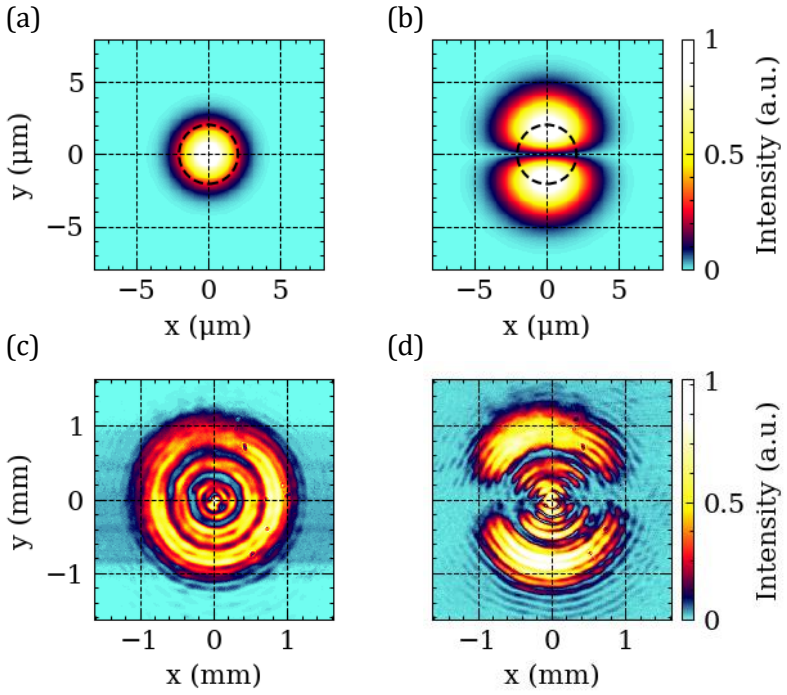

Figure 10 – Simulated electric field mode shape focusing on the fiber with a Thorlabs lens 354280-A, f=18.4mm, in colinear(a) and cross-polarization(b). The dotted circles represent an SM fiber core. (c)(d) Beam shape measurement with the described lens for the respective configuration.

Here $\theta_0 = 2/(k_0\omega_0)$ Is the mode divergence. When the beam is reflected with an angle θ_i on a mirror will undergo a modal transformation $M_{u,v}$

$$\vec{E}_{uv} = M_{u,v}\vec{E}_{0uv} \tag{4-3}$$

Where:

$$M_{u,v} = \begin{bmatrix} r_p & 0 \\ 0 & r_s \end{bmatrix} + u\begin{bmatrix} r_p' & 0 \\ 0 & r_s' \end{bmatrix} + v\frac{r_p + r_s}{tan\theta_i}\begin{bmatrix} 0 & -1 \\ 1 & 0 \end{bmatrix} \tag{4-4}$$

Which transforms a beam such as eq. 4.2 into a sum of Hermit-Gaussian modes TEM_{00}, TEM_{01}, and TEM_{10} [101].

Only the third term remains after going through a polarizer, as the first and the seconds cancel out. Finally, when the beam is focused with a lens with focal *f*, the field becomes:

$$\vec{E}_{f\perp}(x,y) = \frac{E_0}{\pi\omega_f^2}\frac{r_p + r_s}{tan\theta_i}\frac{y}{l_f}e^{-\left(\frac{x^2+y^2}{w_f^2}\right)}\vec{e}_\perp \tag{4-5}$$

Here $\omega_f = \lambda f/\pi\omega_0$ is the beam waist at the focal plane and $l_f = k_0\omega_f^2/2$ is the Rayleigh range. An intensity hole appears at the center, surrounded by two lobes at $y = \pm\omega_f/\sqrt{2}$. This result

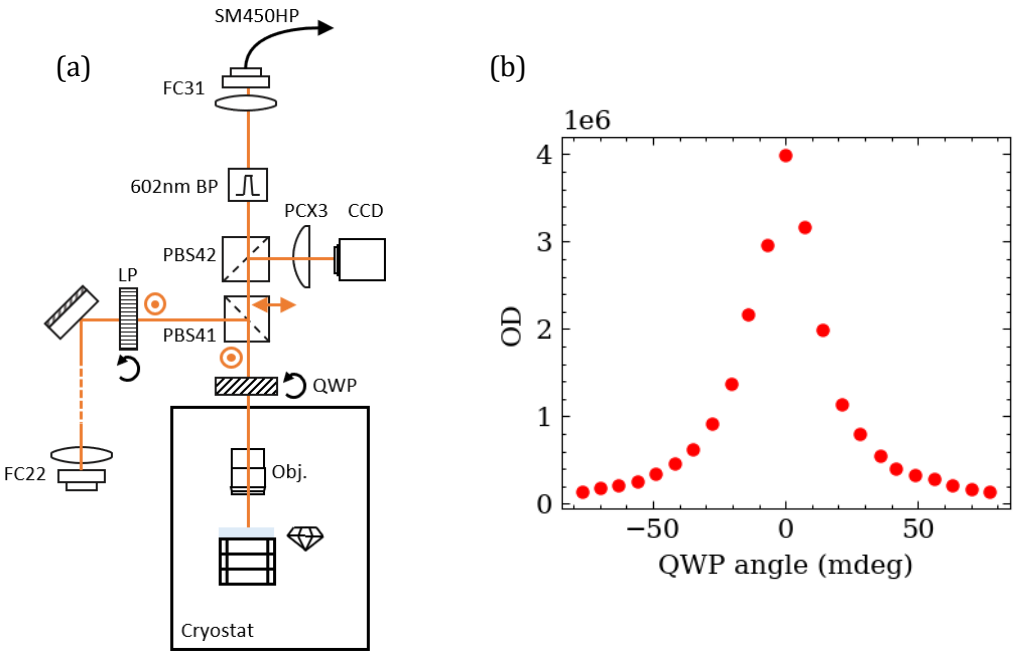

Figure 11 – (a) Cross-polarization extinction confocal microscope setup. LP: Glan-Thompson linear polarizer, PBS polarizing beam splitter cube, QWP: quarter waveplate, BP: bandpass filter, FC: fiber coupler, SM: single mode fiber, PCX: plano-convex lens. (b) Extinction curve measurement obtained by rotating the QWP, showing a maximum extinction ratio of 4e6.

indicates that a cross-polarization extinction setup will perform polarization rejection and act as a spatial filter, as displayed in Fig.10b.

4.3.2 Polarization setup and performance

For clarity, the confocal microscope cross-polarization part from Fig.8 is reproduced in Fig.11.

The beam is prepared by a Glan-Thompson (Thorlabs, GTH5M) linear polarizer (LP), mounted on a motorized rotation stage (Thorlabs, PRM1), with a 7 mdeg position resolution. A PBS (B-Halle, PTW25) directs the polarized beam towards the objective lens (Thorlabs, C330TMD-A, $f = 3.1$, 0.7NA). As mentioned in the previous chapter, polarized light reflected onto a mirror undergo a small polarization angle shift. Part of this leakage can be compensated with the QWP (B-Halle, RAC3.4.10), mounted on a similar motorized rotation stage, where excitation light should go back to their incoming path. A 45 deg rotation on the double pass QWP configuration can perform a 90 deg rotation on the polarization angle, hence transmitting 100 % of the laser light, which is used as a reference.

An extinction of 50 dB is achieved with sole polarization filtering.

Spatial filtering is done with the modal transformation described in 4.3.1. Single-mode fiber coupling is done with the same lens as FC22 (Thorlabs, 354280-A), yielding a total extinction of 66 dB, or a 4e6 extinction ratio (see Fig.11b).

4.4 DETECTION

Collected photons' properties are coupled into an SM fiber. The photon flux can be directed into the appropriate detector to perform the following measurements.

4.4.1 Spectroscopy

An optical spectrometer measures the broad emission spectrum of the quantum emitter. The model is an Andor Shamrock SR-500i mounted with a Newton DU970N-FI EMCCD camera, with a grating of 1200 ln/mm, yielding to a resolution of ~0.07 nm at 602 nm

This instrument allows the extraction of the different energy levels and ground-state and excited-state splitting at any temperature. It finds its limitation in the linewidth measurement in the linewidth/lifetime measurement when cooling down the sample, as the transform-limited lifetime is 27 MHz for GeV-, which is equivalent to $\Delta\nu\frac{\lambda^2}{c} \approx 0.03$ pm at 602 nm wavelength, far below the 0.07 nm resolution limit of the spectrometer.

Every spectrum acquired with this instrument is taken under off-resonant excitation, with a 532 nm wavelength laser, at an excitation power of 30 mW.

4.4.2 Resonant fluorescence spectroscopy

Resonant fluorescence measurements are used to measure different properties and physical behavior of a quantum emitter. Laser scans gives information about the emitter lifetime and spectral stability where CW resonant excitation measurement can bring information about its dynamic.

The following paragraphs describe the alignment protocol executed to perform any resonant excitation measurement presented in this work.

The brightest transition is selected from a spectrum acquired from an off-resonant spectrum measurement for resonant fluorescence measurements, as described in 4.4.1.

A fraction of the 602 nm SFG signal is sent to the spectrometer to align the wavelength to the desired transition using the CTL motor scan, with a 5 pm step size. It corresponds to a ∼4 GHz step size, which falls within the 57 GHz CTL laser piezo-scanner range.

Following the rough wavelength alignment, the confocal microscope collection fiber is connected to a fiber-coupled single-photon avalanche diode (SPAD) detector from Perkin Elmer (SPCM-AQRM-16-FC), with a dark-counts of ∼30 ct/s.

A 25 GHz/s ramp signal is set to the CTL laser to the full 57 GHz frequency range to detect a fluorescence peak, around which the scanning range will be finely tuned. The piezo scanner is controlled by a 0-140 V signal, corresponding to a ±28.5 GHz range around the central frequency. The piezo nonlinear behavior at the edges is avoided by centering the fluorescence signal around 70 V (0 GHz). The SFG crystal temperature is adjusted to ensure phase-matching conditions, and final frequency is measured with the laser spectrum analyzer (1 GHz frequency resolution).

4.4.3 Intensity correlation

Second-order correlation, or intensity correlation spectroscopy, is used as a tool to prove single-photon emission. The measurement is done with a Hanbury Brown and Twiss interferometer, where a photon flux is separated by a 50:50 beam-splitter and sent to two different SPADs, representing two channels. Each photon impinging any detectors is saved in time-tagged-time-resolved (TTTR) mode, using an ultra-fast event recorder (PicoQuant, PicoHarp300), with a 4 ps resolution. The second-order correlation function, or $g^{(2)}(\tau)$, extracts the time delay between every photon in the "start" channel and the other. In the case of a single-photon source, a dip is observed at zero-time delays, indicating antibunching.

This type of measurement can provide more intrinsic information about quantum emitters on their electronic structure, their dynamics, and even about their light states.

4.5 EXPERIMENTAL CONTROL

Such an experimental setup includes many instruments operating simultaneously. Control and synchronization are crucial to take complex measurements. A data acquisition card (PCIe-6323) is used as an interface between the control computer and the instruments. Qudi Python modular interface [102] is used to control devices and acquire signals for the following measurements:

- SPADs count-rate acquisition, using NI card analog inputs (AI)
- Confocal fluorescence mapping, with the Attocube XY piezo-scanners control on NI card analog outputs (AO) and SPAD acquisition
- Laser scans, with the CTL piezo-scanner control on an NI card AO, and SPAD acquisition
- Extinction ratio QWP and LP scans, with the motorized stages control connected to USB ports, and SPAD acquisition

All other measurements are made with instruments' manufacturers' software.

CHAPTER 5

SAMPLE CHARACTERIZATION

In this chapter, the diamond membrane sample (MGEV2) spectral properties will be presented.

The sample was mounted on a dielectric HR mirror (LaserOptik) inside the cryostat. The HR coating was designed to be highly reflective for 602 nm and highly transmissive for 532 nm. Most of the measurements were done under resonant excitation conditions.

5.1 RESULTS

5.1.1 Confocal map

The confocal microscope is described in Chapter 4.1. The 2D scan is necessary to select an emitter with interesting properties. A GeV center that is too close to the edge or has many other defects in its proximity could be significantly disturbed by lattice strain or charge traps.

Each newly investigated area is bleached with high intensity laser at 532 nm wavelength and 30 mW power. This process suppresses fluorescence from remaining surface contaminants deposited during the sample cleaning and transfer processes, reducing background signal or increasing the SNR. Commonly, a scanning speed of 1 min$\cdot \mu\mathrm{m}^{-2}$ was sufficient to suppress most of the contaminants' background signal.

Subsequent confocal scans are done on bleached areas with at the same 532 nm wavelength laser and excitation power. Fig.12 shows a typical scan at 4 K temperature, where the diamond background fluorescence decreased to $\sim$5 kcts/s, and the GeV centers signals ranging from 30 to 100 kcts/s, yielding an SNR of 6-20.

It must be noted that ideal off-resonant excitation is altered by the chromatic aberration of the objective lens. As mentioned in Chap.4, the lens aberration induces a focal shift of $\sim 30\mu$m between 532 nm and 602 nm wavelengths. Therefore, the 532 nm beam is defocused beforehand to compensate for the aberration, which slightly underfill the entrance pupil of the objective and increases the beam waist on the sample, up to $\sim 1\mu$m.

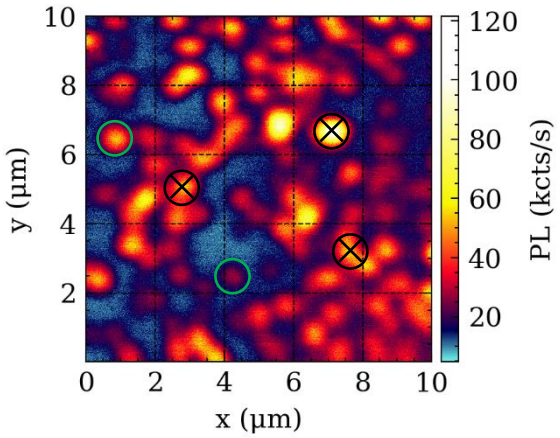

Figure 12 – 10x10 µm confocal image on MGEV2 sample. Green-circled emitters are typical homogeneous GeV centers whereas black-crossed often present strong line shifts and more than four optical transitions.

The full piezo scanner range of 30 μm allows to estimate the emitters' concentration of ~1.25 μm^{-2}. The implantation dose was $5 \cdot 10^9$ cm^{-2}, resulting in a conversion efficiency of 2.5 %.

This relatively high density makes the emitter's spatial selection important. It will be seen in the spectra that the brightest emitters are GeV clusters, and their reciprocal proximity adds strain to the crystal lattice. Spectral shifts are observed, as reported by *Lindner et al.* [103]. The emitters studied in this work have been carefully selected to be spatially isolated from other defects and their spectra to be homogeneous. (See example Fig.13b,c).

One should also consider the polarization detection method discriminating photons not aligned to the PBS polarization axis. Group-IV defects have transitions A-D dipoles emission axis orthogonal to transitions B-C, (transitions are shown in Fig.2). This effect is evident in cross-polarization configuration, where only transitions B-C are visible, whereas in the non-polarized scheme, the four transitions are collected, see Fig.13a.

5.1.2 Spectral distribution

The Germanium-Vacancy centers have four optical transitions at cryogenic temperatures, as shown on the spectrum acquired on a single emitter, with 532 nm wavelength off-resonant excitation of Fig.13a.

Homogeneous spectral properties are crucial to producing an indistinguishable single-photon source for quantum technologies. High temperature annealing during the fabrication process is essential to improve this property by relieving strain in the diamond lattice and easing the vacancies' mobility. The MGEV2 sample's spectral distribution in Fig.13c was obtained on 46 randomly selected emitters. Each occurrence is extracted on each spectrum, where numerous emitters ($\sim 50\%$) had varying numbers of visible optical transitions, between 1 and 7. The emitters' high density can partially explain this inhomogeneity. Indeed, two or more nearby emitters can induce strain in the diamond lattice that affects each other's properties, e.g., more than 4 peaks, optical transitions > 604 nm.

Homogeneous emitters can be identified by selecting spatially isolated, as shown in Fig.12. From a 15x15 μm area, 26 isolated emitters were chosen to obtain the spectral distribution shown in Fig.13b, where the following optical transitions are obtained.

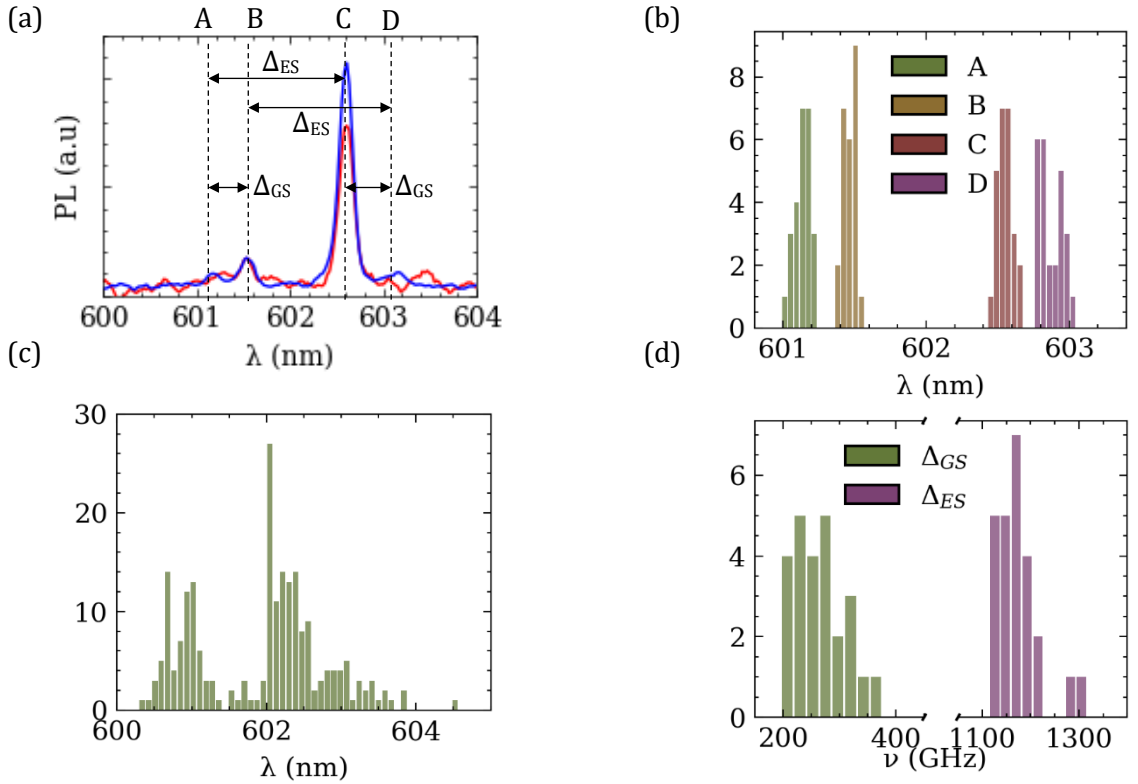

Figure 13 – (a) GeV center spectrum at 4 K, showing the four optical transitions in blue, and in cross-polarization detection (red), transitions A and D are filtered. (b) Averaged optical transitions of 26 homogeneous (b), and 46 inhomogeneous (c) emitters. (d) Ground and excited splitting averaged from (b).

Transition	THz (nm)
A (1-4)	498.711±0.046 (601.135±0.055)
B (2-4)	498.440±0.035 (601.461±0.042)
C (1-3)	497.537 ±0.044(602.552±0.053)
D (2-3)	497.275±0.067 (602.870±0.081)

Table 6 – Optical transitions frequencies obtained from 26 spatially isolated emitters.

These results allow evaluating the ground- and excited-states orbital splitting:

	ν (GHz)
Δ_{GS}	267±45
Δ_{ES}	1171±49

Table 7 – Measured ground and excited states splitting on the MGEV2 sample. The results are the average values of 26 homogeneous emitters.

The values are higher than what has been previously reported [50], which could indicate residual strain in the lattice.

5.1.3 Saturation curve, SNR

Saturation of fluorescence as a function of excitation power was characterized in both off-resonant and resonant configurations. The laser was set at zero-detuning in the resonant excitation measurements, and the count rate was recorded for different power values. The results were fitted to the expression (2-14). Fig.14b shows the saturation curve of four typical GeV centers, where saturation powers from 6 up to 100 nW were obtained. These values are significantly smaller than previously reported [58,60].

5.1.4 Linewidth, spectral diffusion, and power broadening

Successive resonant excitation (RF) laser scans around the optical transition C were done on the GeV centers to measure their excited-state lifetime, spectral diffusion, and power broadening.

The GeV centers spectral stability was measured during 5.5 hours (Fig.14a), where a laser scan was done every 40 seconds (500 scans). Slow frequency drift of ~100 MHz is observable. It is hasty to conclude this slow drift to the emitters. Experimental conditions changes are hardly appreciable over longer measurement time, and the laser spectrum measurement instrument (HighFinesse, LSA) limits the stability measurement to a 1 GHz frequency resolution. The random fluctuations inducing diffusion occur in a short timescale and can be visible in altering the average fluorescence spectrum by adding a Gaussian contribution, resulting in a Voigt profile (Fig.14c). The sample used in this work showed a negligible

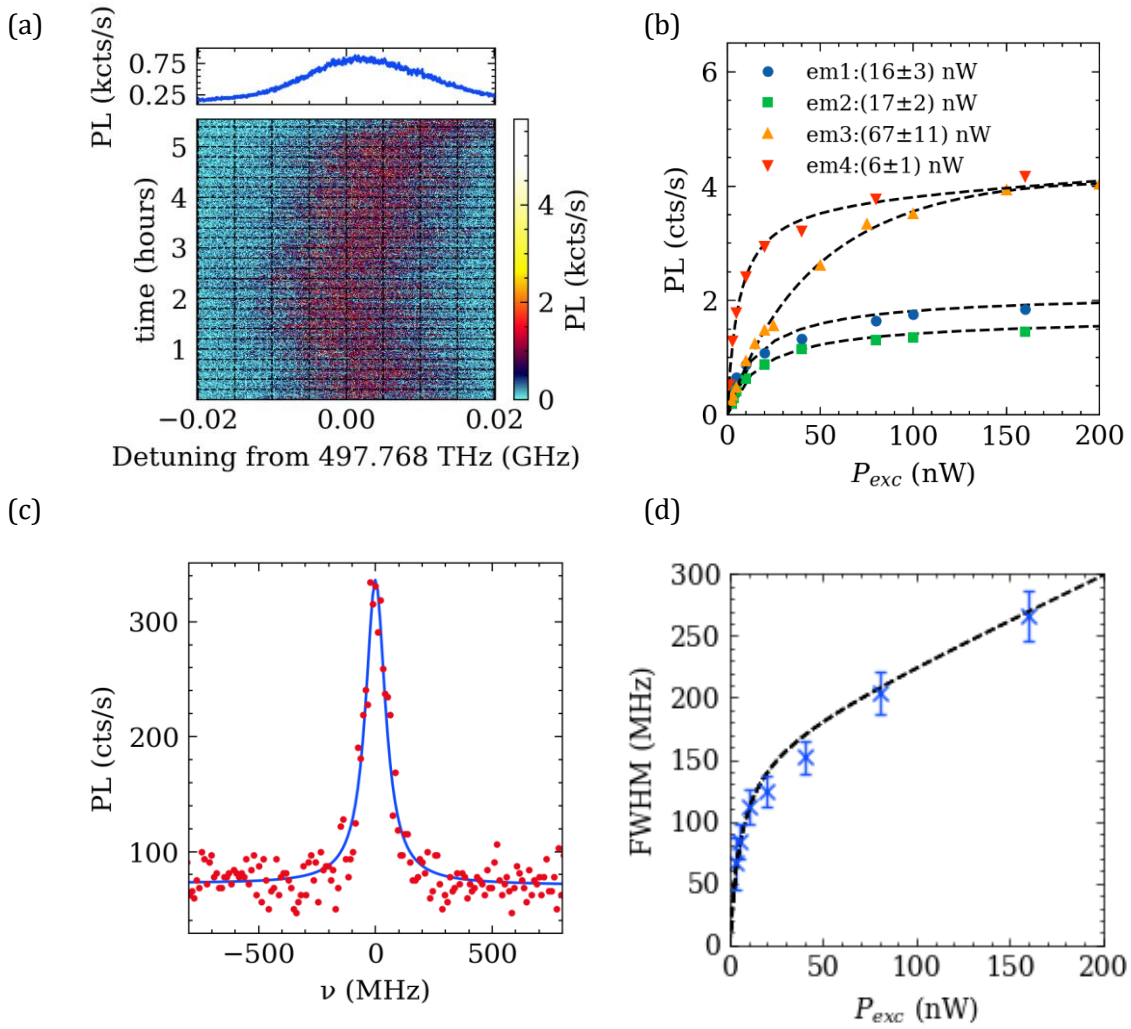

Figure 14 – (a) Spectral diffusion of a GeV center over 5.5 hours. (b) Resonant excitation saturation curves of four characteristic GeV centers. (c) Linewidth characterization with 50 consecutive averaged laser scans. (d) Typical power broadening behavior of GeV centers.

Gaussian contribution in the Voigt function, which can eventually be assumed to be Lorentzian:

$$\Delta\nu = f(x; A, \mu, \sigma) = \frac{A}{\pi}\left[\frac{\sigma}{(x-\mu)^2 + \sigma^2}\right] \tag{5-1}$$

where the FWHM is equal to 2σ. At low excitation power, a linewidth down to 65 MHz was obtained. This value ranges close to the transform-limited linewidth of 26 MHz [58]. Alternative processing, fitting every laser scan yielded an FWHM of 42 MHz on a single GeV center.

Fig.14d shows the linewidth power broadening of a single defect, characterized by [104]:

$$\Gamma = \Gamma_0\sqrt{1+P} \tag{5-2}$$

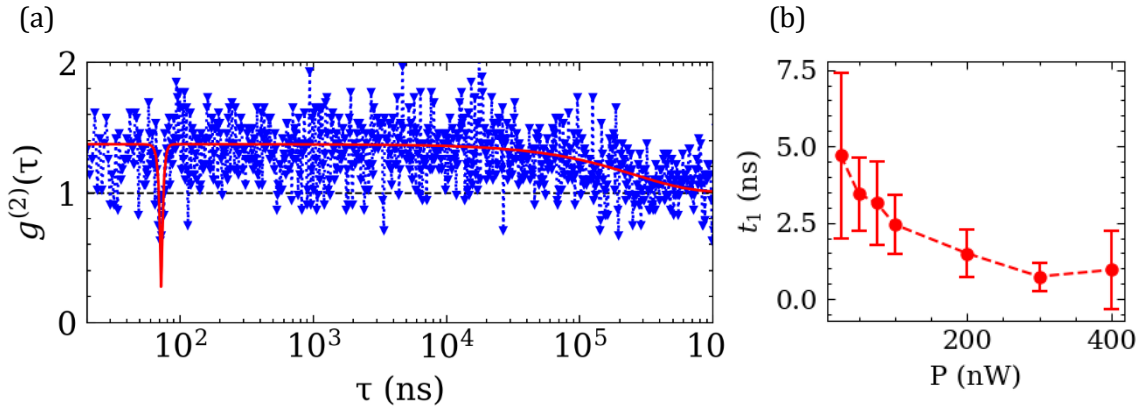

Figure 15 – (a) $g^{(2)}(\tau)$ on a GeV center at 4 K. The $g^{(2)}(0) < 0.5$ proves the single-photon character of the emitter,, and bunching appearing on longer time-scales shows the signature of a dark-state. (b) Time constant parameter t_1 extracted from the 3-level system model.

5.1.5 Correlation intensity measurement

Second-order correlation measurement was done on several emitters under CW resonant-excitation conditions, and ZPL detection. Fig.15a shows the results for a GeV center excited at $P_{exc.} \cong 2 \cdot P_{sat.}$, where a total acquisition time of 10 minutes was selected to collect enough events (count-rate ~30 kcts/s). No Rabi oscillations are visible, suggesting quick decoherence in the ground and excited states. Moreover, bunching appears on longer time-delays, indicating the existence of at least one shelving state, with long lifetime. Hence, the following expression is used for fitting:

$$g^{(2)}(\tau) = 1 - \rho^2 \left[(1 + C_1) e^{-\frac{|\tau|}{t_1}} + C_1 e^{-\frac{|\tau|}{t_2}} \right] \qquad (5\text{-}3)$$

where ρ <1-SNR, the signal-to-noise ratio.

Results of t_1 at low excitation power gives information about the excited state lifetime. From Fig.15b, we can extract a lifetime of 5 ns, which is in good agreement to previously reported results.

The three-level system will be associated to a dark-state, resulting in optical blinking will be further discussed in the next chapter.

5.2 Discussion

The sample used in this work showed homogeneous spectral properties and low spectral diffusion when GeV centers are spatially selected. Overall spectral properties are in good concordance with state-of-the-art results, with excited-state lifetimes ~ 2.3 ns, and ground and excited state splitting of 267 GHz and 1171 GHz, respectively. Lower emitters density could release strain in the diamond lattice, improving the general homogeneity.

CHAPTER 6

FLUORESCENCE SWITCHING EFFECTS

6.1 OPTICAL BLINKING

The sudden ON/OFF fluorescence switching, or fluorescence intermittency, or optical blinking, is an undesired property of quantum emitter. This phenomenon can be explained by the existence of a dark state in its energy levels but can take various forms of complex dynamics. This behavior was observed on around 20 % of the investigated emitters. Dark states were reported in group-IV defects in previous works [51,60], but further investigations are necessary to understand the underlying processes better that could lead to improved fabrication or optical control to mitigate it.

6.1.1 Results

This optical blinking phenomenon is presented in Fig.16a, on successive resonant scans on a GeV center. We can observe that as the laser scans through the transition, the fluorescence signal suddenly goes to the background level, visible on the resulting truncated Lorentzian on the averaging of the scans. The laser wavelength was set in resonance with the emitters' transition in CW to get a more accurate vision of the dynamics. The resulting fluorescence signal is shown in Fig.16b, where a dark-state lifetime ranging from milliseconds to seconds was visible. The counts' statistics for 3-minute-long measurements are shown in Fig.16c, where two Poissonian curves appear for the background signal when the fluorescence is OFF and for the emitted photons when ON. This acquisition method allows extracting the mean bright-state lifetime by averaging every ON time-lapse as a function of excitation power. The acquisition rate was adapted for each measurement parameter to optimize the ON/OFF contrast. This technique shows a limit at higher excitation powers (>45 nW $\sim 0.5 \cdot P_{sat}$), where the bright-state lifetime measurement gets limited by the acquisition time resolution (1 kHz), the emitter count rate (~10 kHz), and data processing limits. We can observe the limitation with the Poissonian distribution of the GeV centers photons lifetimes collapsing to a homogeneous distribution.

The transition rate from the bright state to the dark state power dependance is shown in Fig.16d. The quadratic dependence fitted on results suggests a two-photon process, with the

form $\lambda(P) = aP^2 + bP$, where λ is the inverse lifetime. The fitting results in a=0.004±0.001 Hz nW^{-2}, and b=0.365±0.026 Hz nW^{-1}.

The dark-state dynamics were not accessible using the same method, as the lifetime appeared to be significantly shorter, ranging from seconds down to submillisecond times. The presence of the dark state is modeled by a 3rd level in a 3-level system, where the second-order correlation measurements is similar to 5.1.5. Physical information can be extracted from the second-order correlation of a coherently driven 2-level system such as the Rabi frequency, and constants related to the relaxation time and the coherence time, as one can see from eq.(2-21). For a 3-level system, additional mechanisms occur making the expression of a second-order correlation complex to derive. Therefore, the time constants resulting from the fitting will be left as such (t_1 and t_2)

The t_2 free parameter is extracted from the 3-level system model expression (5-3). The fitting results of TTTR measurements at three different resonant excitation powers are shown in Fig.17a. Bunching appears on the right-hand side at longer time ranges. In this visualization, t_2 of 490±6 μs, 360±4 μs, and 257±3 μs were obtained for the excitation powers of 50 nW, 75 nW, and 100 nW, respectively. These dynamics decrease for higher excitation power is represented in Fig.17b, and similarly, as for the bright-state lifetime, a quadratic trend is observed, where a=0.05±0.02 Hz nW^{-2}, and b=32.2±6.5 Hz nW^{-1}. The blinking can originate from diverse causes and looking at the wavelength dependence of additional light could bring better understanding of the source of it. Low power CW off-resonant light was added to the resonant laser beam, and similar measurements were repeated with 532 and 450 nm, as shown in Fig.17c,d. One should be cautious with the exact power values for both wavelengths. The achromatic aberrations could lead to weaker coupling with the emitter than expected, and more data points would be needed for the 450 nm measurement to have a conclusive interpretation.

Nonetheless, the trends show a linear dependence and shorter dark-state lifetimes. The data were fitted with the expression $\lambda(P) = mP + c$, yielding the following results

	***m* (Hz nW^{-1})**	***c* (Hz)**
532 nm	7.6±0.6·10^3	26.7±12.1·10^3
450 nm	284±4	9.9±1.2·10^3

Table 8 – Fitting results for dark-state lifetimes with the addition of 532 and 450 nm wavelengths CW light.

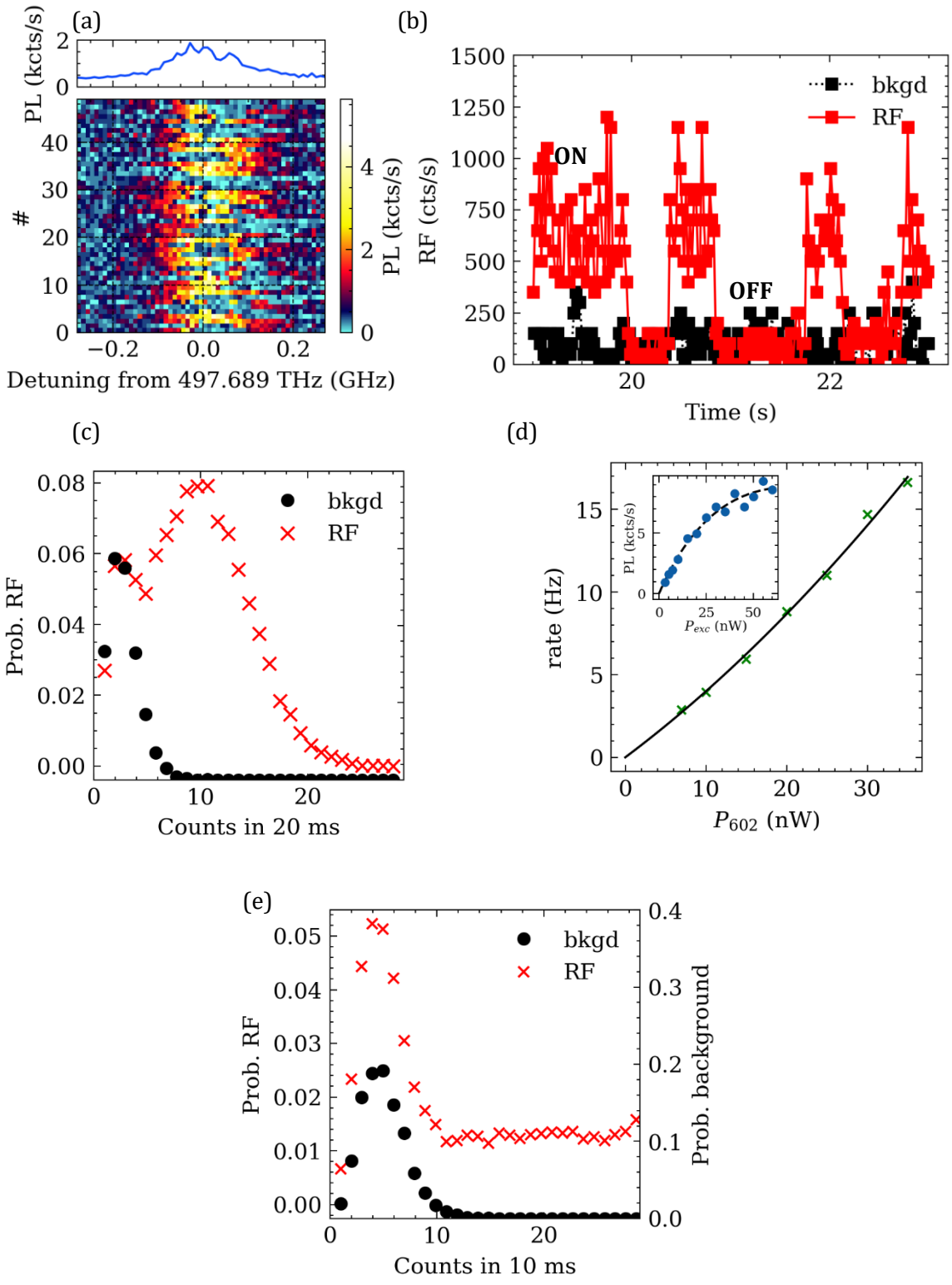

Figure 16 – (a) Resonant fluorescence scans on an emitter at 10 nW excitation power, showing extinction of fluorescence (b) Resonant fluorescence time trace. (c) Intensity histogram acquired with an RF measurement, where two Poissonian distributions are visible for the background and the emitter. (d) Excited-state inverse-lifetime from CW RF measurement Inset shows a saturation power of 86 nW. (e) Counts statistics for 100 nW excitation power (~$2P_{sat}$) and 100 Hz acquisition rate. The Poissonian distribution of the GeV centers' emission disappears due to instrumentation and processing limitations, resulting in a "flat" distribution.

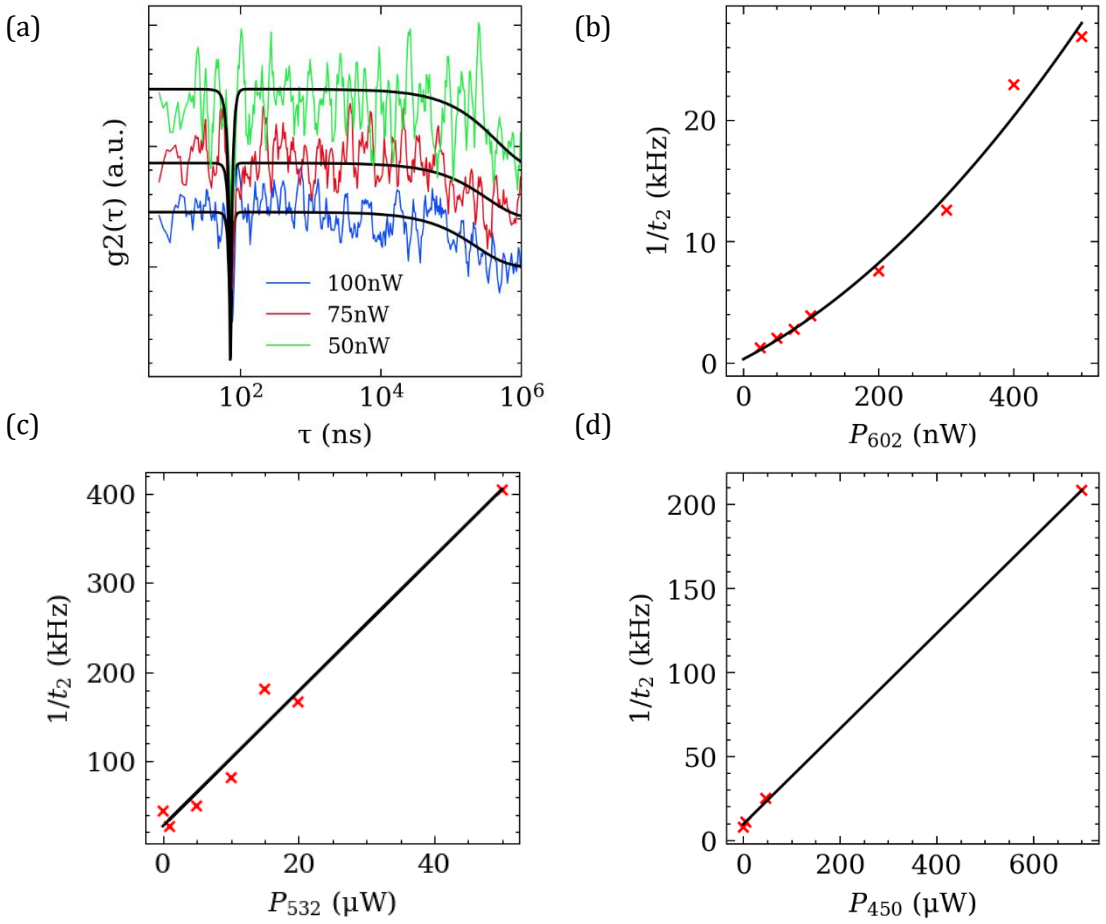

Figure 17 – (a) Second-order correlation measurement at different resonant excitation powers, showing that the dark-state lifetime is decreasing the power increases. Curves are shifted in y-axis for visibility. (b) Dark-state inverse-lifetime extracted from resonant fluorescent TTTR measurement. (c,d) Dark-state inverse lifetime from TTTR measurement with 200 nW resonant laser and additional 532 and 450 nm, respectively.

6.1.2 Discussion

Chen et al. suggested the presence of a dark state in the electronic structure of the GeV centers, forming a 3-level system with the presence of a metastable state [60], that is pictured in Fig.23b. They suggested that the shelving into the dark state could occur in a twostep process due to resonant laser via a metastable electronic level, which could concur with the observation we made here. Dynamical measurements using laser pulses would bring additional information about the transition rates between the different energy levels.

6.2 Spectral jumps

Quantum emitters can show unstable energy level transitions with discrete energy fluctuations, which can be observed as optical blinking or the apparition of other levels on PL scans. This effect was previously reported in group-IV defects as spectral jumps by *Mu et al.* [105], where they observed binary spectral jumps on SiV centers in the range 15 to 17 nm of amplitude on a GeV implanted membrane sample and a few GHz in a nanodiamond sample.

The physical origin of this undesired behavior needs to be elucidated to fabricate reliable platforms for QIP technologies. This section is dedicated to the investigation of such spectral jumps in the MGEV2 sample, where the majority of the investigated emitters (>50 %) exhibited such features.

6.2.1 Results

Spectral jumps are distinctly visible in resonant laser scans measurement, as shown in Fig.18. In addition to the previously presented optical blinking expressed by fluorescence extinction while scanning through the emitter transition, sudden discrete jumps operate to a well-defined energy level. These jumps occurred between two and more energy levels, as seen in Fig.18b. To facilitate the processing, results with jumps between two energy levels were picked for the analysis.

The dynamic was studied on an emitter exhibiting binary spectral jumps of ~ 1 GHz, while being coherently driven. Special care was taken to select a GeV center with a short dark-state lifetime to prevent cross-misinterpretation with the jumping dynamic. More generally, the dark-state lifetimes occurred in one order of magnitude shorter timescales in the > 1 kHz range versus a few Hz for the spectral jumping rate.

At this point, the jumps are associated to a charge fluctuation, either from the emitter or from the environment. The charge rate transfer is shown in Fig.19b, where a linear trend is fitted.

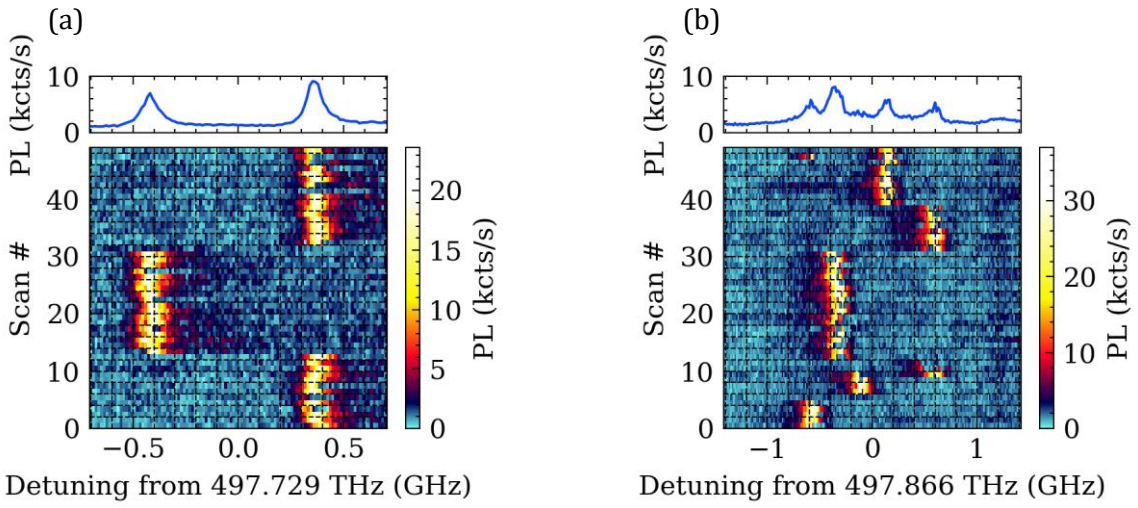

Figure 18 – Typical energy level fluctuations from two different emitters, with 2 discrete energy levels (a) and 5 energy levels (b). Each resonant scan has 100 points acquired at a 200 Hz acquisition rate.

The RF intensity measurement gives the charge transfer rate information but no information about the electronic structure. Hence, second-order correlation intensity measurements were done on an emitter to obtain information about the possible number of electronic levels and time dynamics involved. Results shown in Fig.20b exhibit a complex electronic structure, suggesting a 4-level system structure, described by:

$$g^{(2)}(\tau) = 1 - \rho^2 \left[(1 + C_1 + C_2 + C_3) e^{-\frac{|\tau|}{t_1}} - C_1 e^{-\frac{|\tau|}{t_2}} - C_2 e^{-\frac{|\tau|}{t_3}} - C_3 e^{-\frac{|\tau|}{t_4}} \right] \quad (6\text{-}1)$$

The power dependence on each time constant suggests two different dynamics regimes, at high (> 3 $P_{sat.}$) and low excitation powers.

At this point, making any conclusion about the origin of these jumps is impossible. The relatively small spectral shifts observed in the measurements indicate a possible Stark shift induced by a nearby charge. Even though group-IV defects should be protected from external electric fields due to their vanishing permanent dipole moment, they are still subject to higher-order shifts:

$$E_{Stark} = -\Delta\mu E - \frac{1}{2}\Delta\alpha E^2 - \frac{1}{3!}\Delta\beta E^3 - \frac{1}{4!}\Delta\gamma E^4 \quad (6\text{-}2)$$

where $\Delta\mu$ is the permanent dipole moment, $\Delta\alpha$ is the polarizability, and $\Delta\beta$ and $\Delta\gamma$ are higher-orders terms related to hyperpolarizabilities of the electronic states [106]. Recent works have

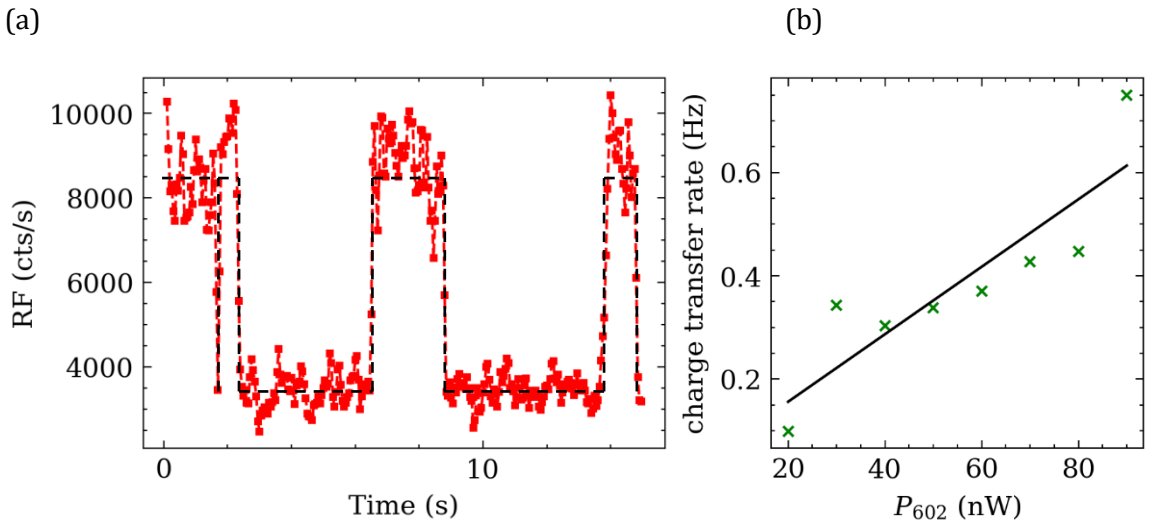

Figure 19 – (a)CW RF measurement with laser tune in resonance with one of the energy levels. (b) Coherent bright state lifetime power dependence. Each data point is extracted from a 2-minute acquisition time measurement, similarly as in (a).

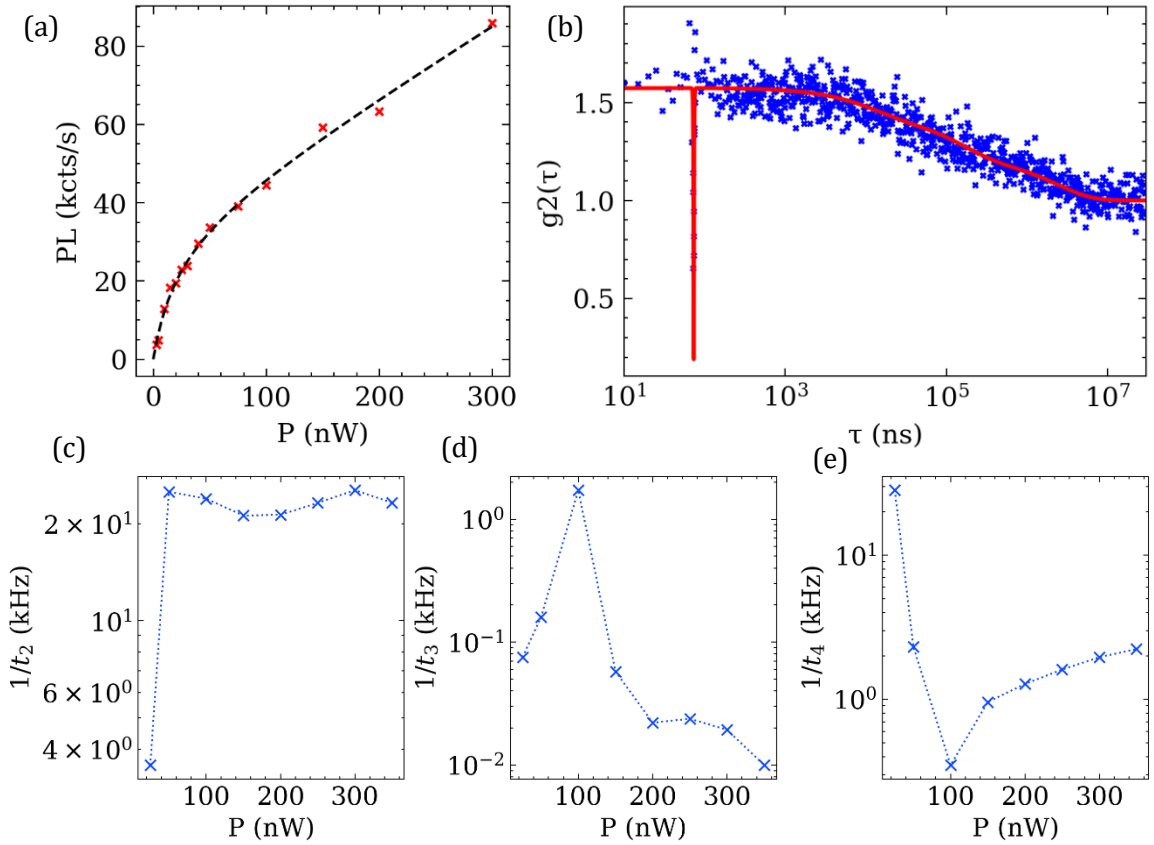

Figure 20 – (a) Saturation curve for a GeV center jumping between levels, having a saturation power of 22±5 nW. (b) Second-order correlation measurement, showing a complex structure. Four different time parameters are required to fit the results. (c)(d)(e) Power dependence of the different time parameters, from fitting.

shown a small linear contribution in Stark shifts in Tin vacancies [106,107]; the major contribution comes from the quadratic term, which should be similar here.

A statistical approach was made from 21 emitters presenting binary spectral jumps. The occurrence was independent of the detection methods. Therefore, data collected with both PSB (13) and ZPL (8) cross-polarized detection united to obtain the statistics. Each measurement was performed under similar conditions, i.e., 50 lines per acquisition at a 500 ms/line rate. A Lorentzian was fitted to the RF signal for every line to extract the central wavelength and determine the average spectral jump value. A histogram containing all the jumps was saved and normalized for each emitter. Finally, all the histograms were combined into one statistic (Fig.21a). A total of 159 measurements were done.

One important observation of this statistic is energy fluctuation amplitudes' distribution of a single GeV center. Indeed, each emitter has a non-unique energy fluctuation value, indicating that the source of the Stark shift must vary in space or charge over time. Different measurement parameters were tested to determine the influence of power and the addition of another excitation wavelength (450 & 532 nm). No correlation could be concluded in the

energy level shift amplitudes. Further measurements are required to observe the effect on the dynamics with the addition of non-resonant wavelength.

An interpretation of the probability distribution shown in Fig.21a will be discussed in the following chapter

6.2.2 Discussion

The origin of spectral jumps is not yet correctly understood. However, some hypotheses were proposed; *Mu et al.* [105] suggested a source due to the presence of P1 defects, or single substitutional nitrogen, in the vicinity of the group IV vacancy centers acting as a charge trap and inducing a Stark shift. Strain or second-order effects of electric field fluctuations in the local environment were advanced by *Maity et al.* [59], acting similarly to the work presented by *Sohn et al.* [52]. Finally, spectral jumps and optical blinking were recently attributed to the presence of divacancies nearby the emitters by *Fuchs et al.* [108], acting both as charge traps inducing Stark shift and as a donor for populating the ground-state after an electron has been promoted to the excited-state.

As aforementioned, the inversion symmetry of group IV defects vanishes the permanent electric dipole moment [37], which should make such group-IV defects invariant to first-order Stark-shift. Despite recent results showing a slight first-order Stark shift on Tin-vacancy centers [106,107], the major contributions come from higher-order terms. Polarizabilities $\Delta\alpha$ of [0.051-0.55] MHz/(MV/m)^2 were extracted from experimental data. To illustrate how an electron charge would affect an SnV center with similar shifts as observed in this work

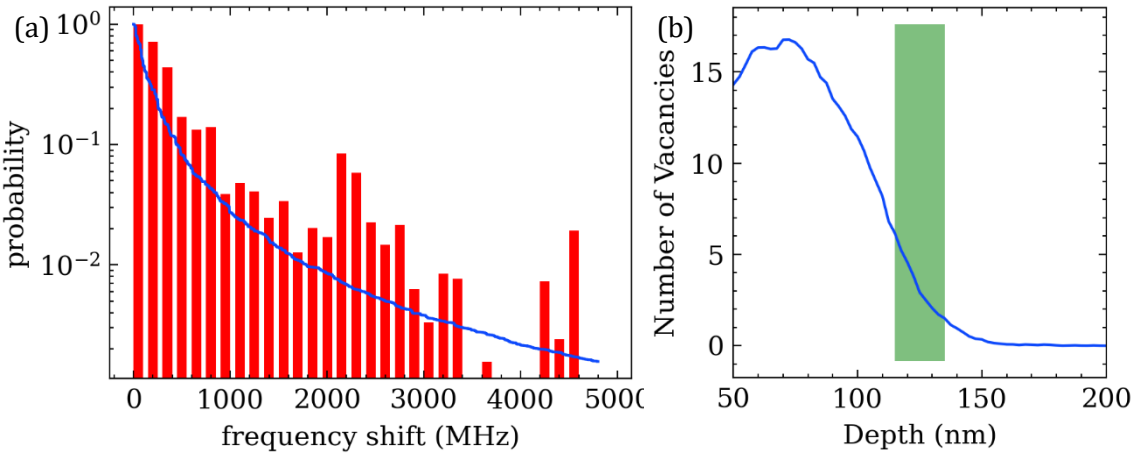

Figure 21 – (a) Binary spectral jump distribution from 23 GeV centers accumulated from 159 measurements. The blue curve represents a $1/r^8$ hypothetical second-order Stark shift induced by a point charge at the carbon sites, within a 2 nm range from the GeV center. (b) Vacancies distributions caused by ion implantation from SRIM simulation. The green area represents a ±10 nm region around the targeted implantation depth of 125 nm, yielding an average of 6 vacancies/ion in the close proximity of the defect.

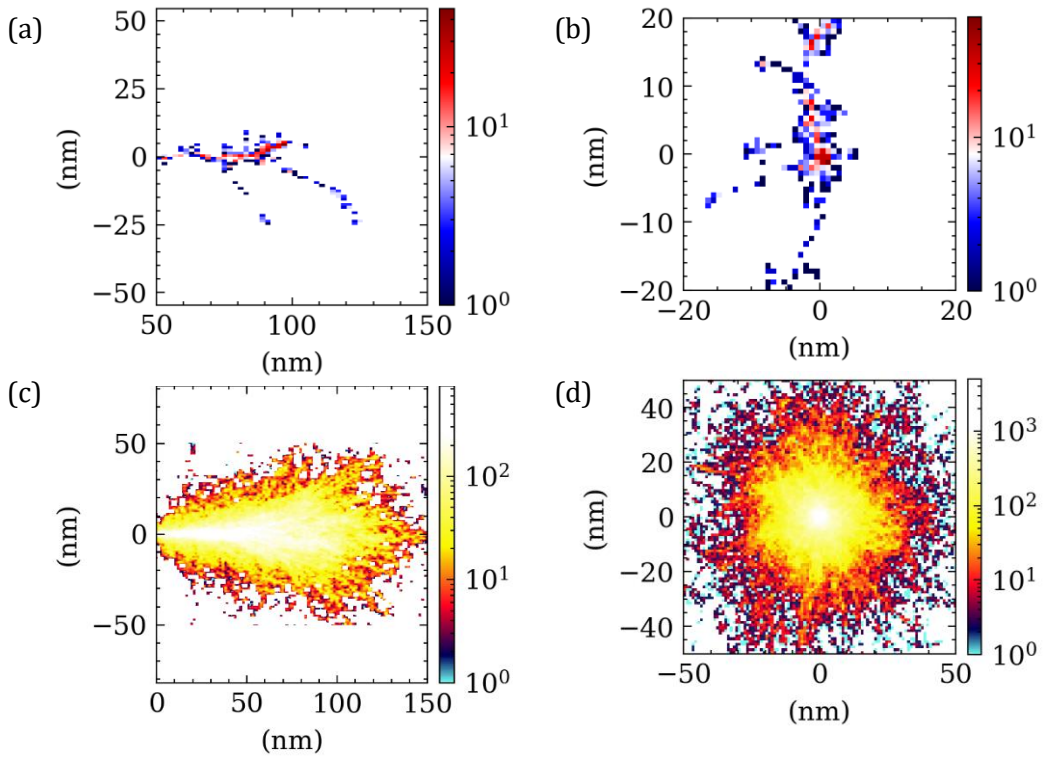

Figure 22 – (a) SRIM simulation showing vacancies cascade creation for 1 germanium ion through a diamond sample. (b) Radial view for the same simulation. (c)(d) Simulation for 200 ions.

(0.1-5 GHz), calculation from the second-order term $\frac{1}{2}\Delta\alpha E^2$ gives a charge-defect distance ranging from $\sim 1.5 - 8$ nm.

The parallel with GeV centers cannot be drawn as no theorical nor experimental for Δα and Δμ values are known yet. However, it appears that a change of one order of magnitude in the polarizability barely affects the induced second-order Stark shift by a factor of $\sqrt[4]{10}$.

With the assumption that the GeV centers' polarizability would be in the same range and that an electron charge induces the jumps, we can hypothesize that the electric field source must be within a 10 nm range around the emitter.

The first suggestion proposed the shifts to be induced by the presence of P1 defects in the diamond lattice. The electronic grade diamond employed in this work specifies a nitrogen concentration [N] < 5 ppb. The diamond unit cell contains 8 atoms and has a lattice constant of 3.567 Å. One billion atoms are enclosed in a $125 \cdot 10^6$ unit cells, corresponding to 500x500x500 unit cells. This gives an average distance from any point to a P1 of 104 nm (the GeV complex concentration is 5 μm^{-2}, or 1 per 450x450 nm^2). The second-order Stark shift induced by P1 defects is therefore unlikely. Indeed, the magnitude of this effects would be much lower from a statistical and jump-amplitude point of view.

An important aspect to consider here is the damage induced during the ion implantation phase. Hundreds of vacancies are created in cascade when the implantation ion decelerates in the diamond's lattice structure. We performed SRIM simulations for a 250 keV germanium ion stream (Fig.22). A total of ~1500 vacancies are created for every implanted ion along its way. In this specific case, most of the vacancies appear around 75 nm, whereas the targeted depth is 125 nm. In a 10 nm sphere around the implanted ions, 60 vacancies are present after the implantation (Fig.21b).

The high-temperature annealing process (2 h at 1200 °C) should have favored the mobility of such vacancies; it is hard to predict what are the actual remaining vacancies in the vicinity of the GeV that can act behaving. However, it is likely that a fraction of these vacancies could not be pulled away from the emitter.

Further experiments with varying annealing temperatures and pressures should be conducted to confirm this hypothesis, and electrical tuning Stark shift measurements to extract polarizability and eventual permanent moment dipole values.

6.3 OPTICAL GATING

This section presents the observation of optical gating of GeV centers under resonant excitation.

Some emitters displayed resonant fluorescence signal quenching which could only be brought back by adding neglectable power of 532 nm off-resonant laser to the excitation. By neglectable, it is meant that no fluorescence is observed by the sole off-resonant 532 nm laser, typically 3 to 5 orders of magnitude below the saturation power. This observation was also reported on a single GeV by *Chen et al.* [60].

6.3.1 Results

The phenomenon is shown on Fig.23, where successive resonant scans through a GeV center's transition 1-3 only show fluorescence when a weak-off resonant laser is turned ON. Scans 10 & 11 show the fluorescence quenching when the off-resonant laser is turned OFF.

The power dependance of the resonant and off-resonant lasers on the linewidth is shown on Fig.25b,c. Fig.25b was taken for resonant excitation with additional 5 μW power CW 532 nm wavelength laser. The curve follows the same trend as in Fig.14d, following eq.(5-2). The off-resonance power dependence is shown on Fig.25c with a 50 nW CW resonant laser power and varying off-resonant laser power. We can observe a plateau at 300 MHz for off-resonant excitation powers <1 mW showing that the 532 nm wavelength have no influence on the excitation from the ground to the excited state but mainly inverting the population from the dark to the ground state.

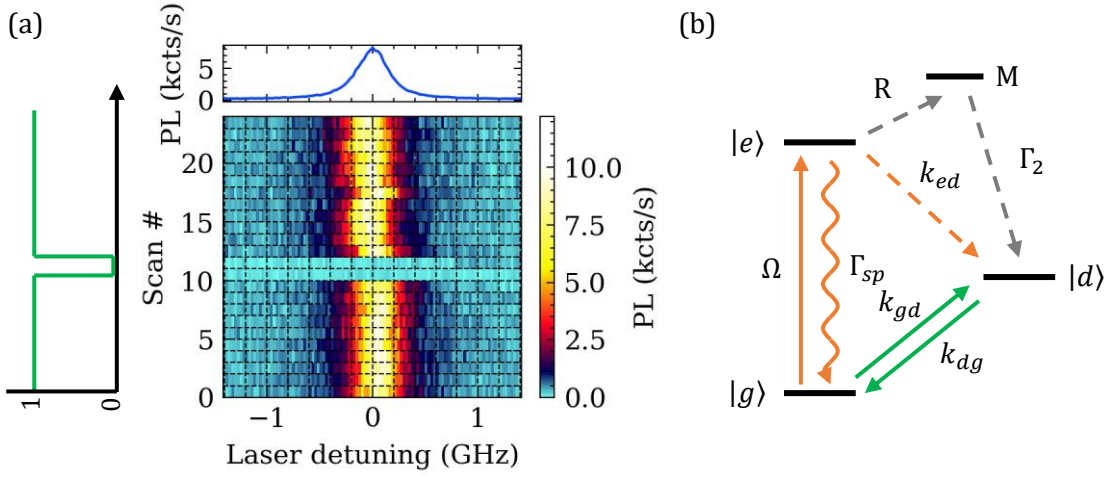

Figure 23 – (a) Optically gated fluorescence measurement under resonant excitation on successive laser scans. Fluorescence is switched-off when a weak nonresonant 532 nm laser is turned off, as visible on scans 10-11. (b) 4-level model proposed by Chen et al. with a dark-state and a metastable state. The M level is believed to have a role in the blinking process. Diagram reproduced from [60]

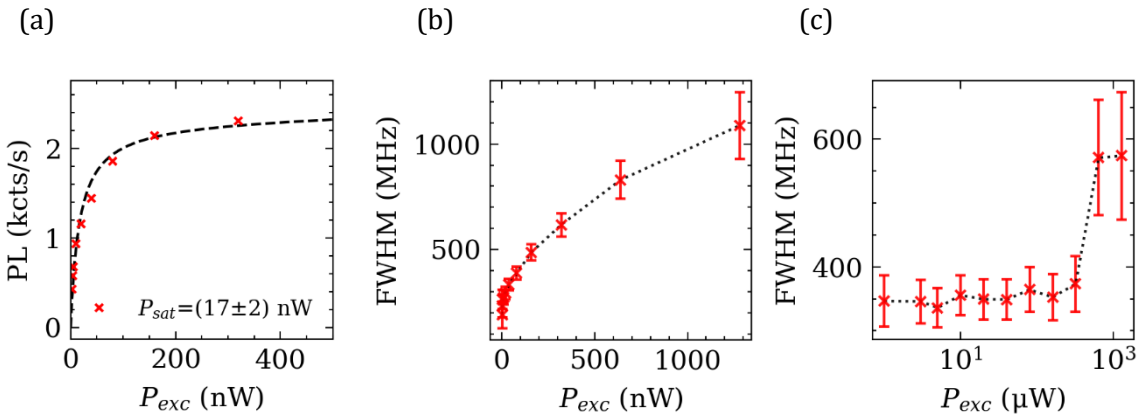

Figure 24 – (a) Resonant fluorescence saturation curve with additional 1.6 µW off-resonant 532 nm laser. (b) Power broadening with varying resonant laser power showing similar broadening as in Ch.5.1.4. (c) Power broadening with varying non-resonant 532 nm wavelength laser power, showing no influence for excitation power below 1 mW.

It is important to mention that the optical gating observation was made only with the PSB detection, and not with the ZPL detection. It could indicate a thermalization process increasing the phonon number triggering the PSB fluorescence.

6.3.2 Discussion

Pulsed measurements allowed *Chen et al.* to extract the dynamics of the rates k_{dg}, k_{gd}, and k_{ed}. Applying similar measurement protocols would probably confirm their observations and conclusion.

An interesting aspect that could be addressed in further investigations is the observation of this gating effect exclusively in PSB detection. One can imagine a detection scheme using dichroic filters to collect separately and simultaneously photons emitted both in the ZPL and PSB and measure the time correlation. Such measurement would give additional insights on the photoemission mechanism of the GeV centers.

CHAPTER 7

NONCLASSICALITY DETECTION

Nonclassicality detection could bring an alternative method to second-order correlation measurement, with a strong interest in resonant excitation measurements. Indeed, the nonclassicality parameters introduced in Ch.2.5 are independent to the Poissonian background, which is a considerable advantage for such measures where excitation light rejection is a challenge.

The α and β nonclassicality criteria described in Ch.2.5.3 can be extracted from an HBT interferometer recording the click events in time-tagged time-resolved (TTTR) mode. Each photon event is recorded by the PicoHarp 300 with a 4 ps time resolution. To evaluate the nonclassicality parameters α and β, different time bins w were tested, and results were compared with the second-order intensity correlation function using a similar time resolution.

An exciting aspect of this analysis method is its robustness to Poissonian noise. In the experimental setup employed in this work, the extinction ratio ($1\text{-}4\cdot10^{6}$) is insufficient to remove all the laser signal. This is even more pronounced for high excitation powers, where the SNR decreases significantly. Therefore, this approach could bring new perspectives to the resonant excitation experiments where background suppression is an essential aspect.

7.1 *ALPHA*- AND *BETA*-PARAMETERS EVALUATION

Nonclassicality detection analysis was done on a single GeV center. The emitter was carefully selected and showed no spectral jump behavior, no optical gating, and a limited dark-state presence not visible in successive laser scans. TTTR measurements in the HBT interferometer were done for several resonant excitation powers: 25, 50, 75, 100, 200, and 300 nW, with a measured saturation power of 50 nW.

Second-order correlations measurements were also recorded in TTTR mode, and time-bins were selected for data processing to be below the emitter's excited-state lifetime of 2-5 ns. Hence, the time-bins were usually 0.5-1 ns.

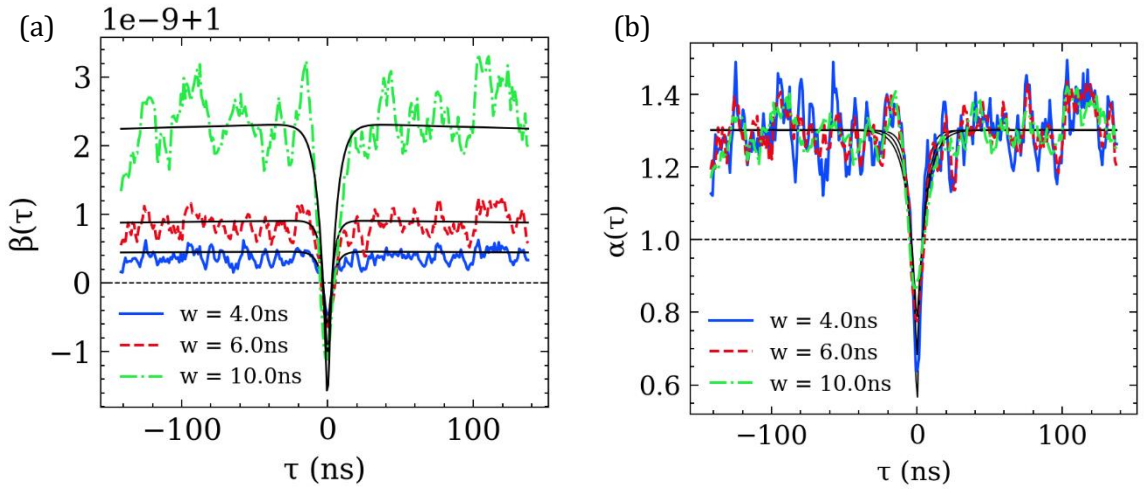

Figure 25 –β-parameter (a) and α-parameter (b) as a function of time-delay τ for different bin-sizes w. The horizontal line at β=1 represents the nonclassicality criterion β<1. The measurement was acquired for 10 minutes, at 100 nW resonant excitation power.

To compare the α and β results with the second-order correlation method, the bin size is set to similar time scales, i.e., 0.5-20 ns.

The effect of the time-bin w on the $\beta(\tau)$ correlation function for three different values is shown in Fig.25. The data are fitted with the following expression, similarly as for the $g^{(2)}$ measurements:

$$\beta(\tau) = 1 - \left(b_1 \cdot exp\left(-1 \cdot \frac{|\tau - \tau_0|}{\tau_1} \right) - b_2 \cdot exp\left(-1 \cdot \frac{|\tau - \tau_0|}{\tau_2} \right) \right) \qquad (7\text{-}1)$$

We can observe oscillations in the data with periods ranging between 12 to 15 ns. Fourier analysis (FFT) on several datasets with different window sizes w did not results in a well-defined frequency that could correspond to the oscillations, e.g., Rabi oscillations. Moreover, similar analysis was performed on different time segments of the whole measurements. The oscillations appeared to be dephased between the different subsets, indicating it to be a numerical artifact. Similar but limited oscillatory behavior was observed on $\alpha(\tau)$ data, as visible in Fig.25b, when the time bin w is 4 ns.

A difference of $\beta(0)$ for the various time bins w is also visible, suggesting an optimal setting for the nonclassicality detection. Fig.26 shows $\beta(0)$ and $\alpha(0)$ for varying time bins w at different resonant excitation powers. Trends appear in the various curves for the two parameters. Indeed, α shows the most nonclassicality when the time bin w is short, similarly as does the $g^{(2)}$ function. In contrast, for β, two observations can be made: a different behavior occurs between low ($<2P_{sat}$) and high excitation regimes, and the optimal time bin w varies with the excitation power. At low excitation power, the emitters behave as a 2-level system,

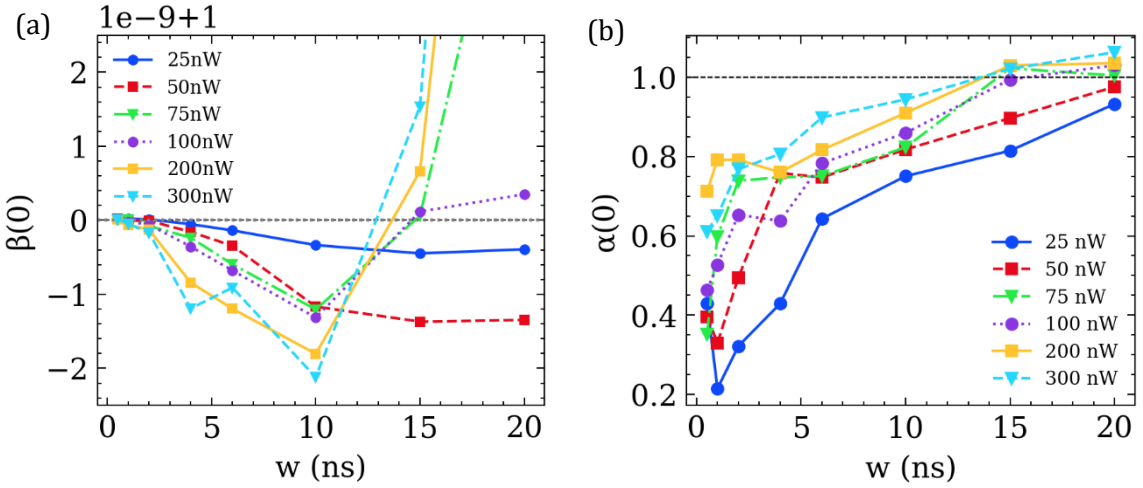

Figure 26 – (a) β parameter and (b) α-parameter values at 0 time-delay for different resonant excitation powers and time-bins. Horizontal lines represent the nonclassicality criteria β<1 and α<1.

which could give a direction to interpret this observation. This will be further addressed in the manuscript in preparation.

Minimum values for *β(0), α(0)* and $g^{(2)}(0)$ are compared in Fig.27. The *α* and $g^{(2)}$ functions appear similar and decrease with the SNR. However, *β(0)* nonclassicality criterion increases as the SNR degrades, which shows the Poissonian background noise robustness of this parameter.

An additional comparison was made with the same measurements and cropping of the dataset to decrease the acquisition time. Fig.28 compares the results for the 100 nW power measurement with acquisition times of 20, 50, and 600 seconds. Results for 20 seconds for all the functions have barely distinguishable features. However, *α* and *β* parameters start to show apparent dips at 0-time delays from 50 seconds, whereas the $g^{(2)}$ function only shows a minor

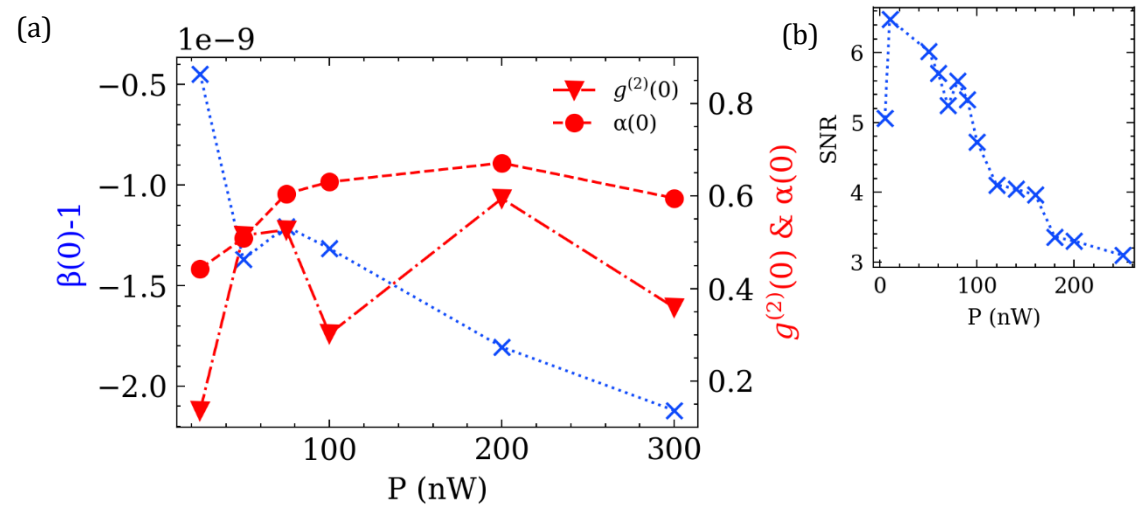

Figure 27 – Minimum β(0), α(0) and $g^{(2)}(0)$ parameters for different excitation powers. The nonclassicality parameters are extracted from the minimum values of Fig.26a,b. Left y-axis is β-1 for readability purposes.

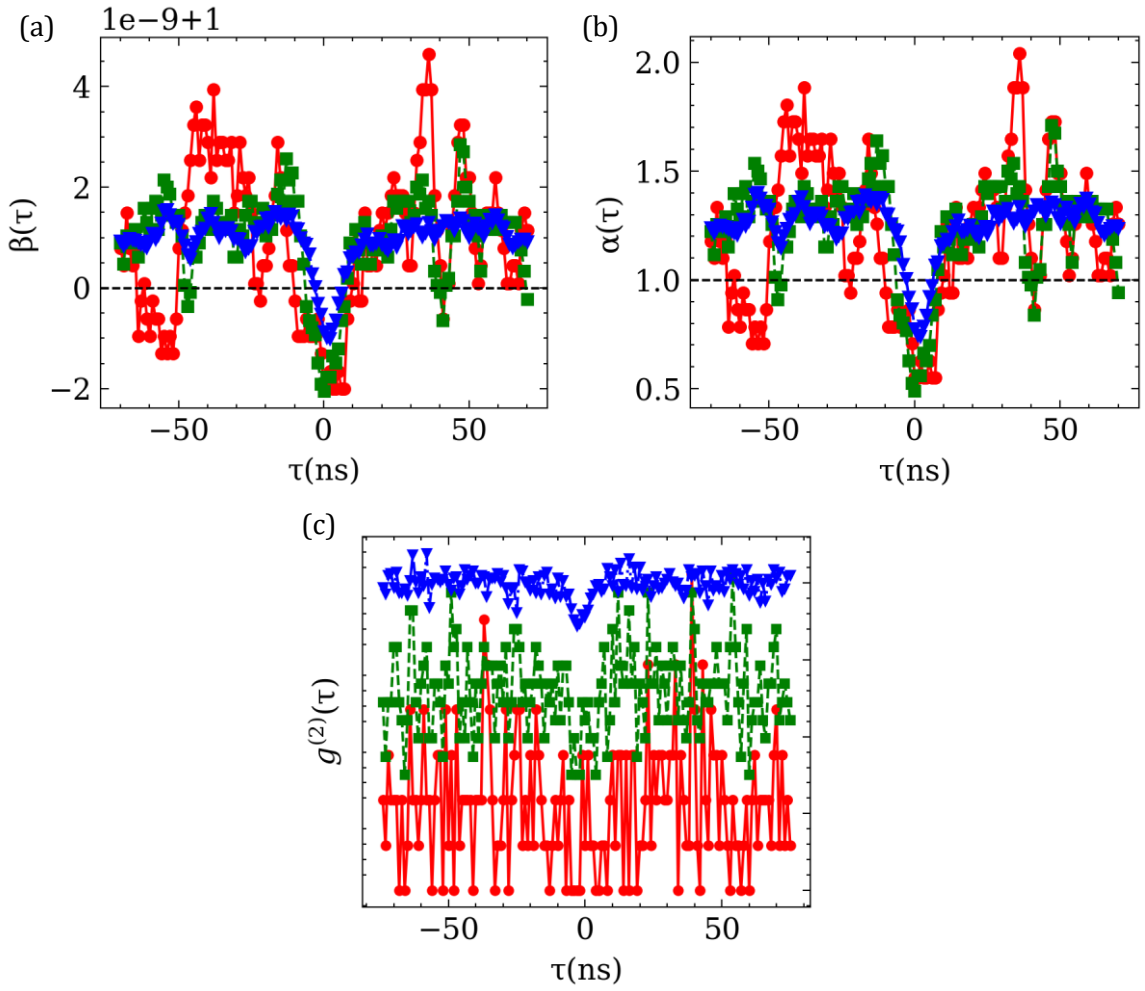

Figure 28 – Varying acquisition times for (a) β, (b) α and (c) $g^{(2)}$ functions. Red, green and blue lines represent 20 seconds, 50 seconds, and 600 seconds total acquisition times, respectively.

drop (green curve). Moreover, the second-order correlation function is limited in resolution when the total count rate is low, which is not the case for the nonclassicality parameters.

7.2 Discussion

This analysis approach combining the second-order correlation and the dual nonclassicality parameters α and β is showing promising results, and bring complementary information on the nature of the source. The processing time is not affected as both methods require scanning through lengthy TTTR measurement files. The α-parameter appears to yield similar curves as the $g^{(2)}$ function but with more contrast for shorter acquisition times.

The robustness of the two parameters to Poissonian noise is a considerable advantage for resonant excitation experiments where laser rejection is challenging for data acquisition.

More information can be extracted from the nonclassicality parameters on the electronic level structure and about the dynamics of the different states, as we can observe from $\alpha(0)$ and $\beta(0)$ for varying time bins w data, and will be discussed in the manuscript in preparation.

CHAPTER 8

FABRY-PÉROT MICROCAVITY

Cavity quantum electrodynamics (CQED) platforms enable strong light-matter interaction between the cavity mode and the quantum emitter. Indistinguishable photons can be generated and increase the spontaneous emission rate by the Purcell factor. The different approaches were described in Chapter 2.6, including nanopillars, nanoring resonators, photonic crystal, and open Fabry-Pérot cavities. The latter offers high-tunability of the platform in terms of emitter selection, Finesse, and cavity length, which directly impact the mode-volume and quality factor, and provide the opportunity to couple out light directly in a fiber. These advantages led to choosing this system to interface the GeV centers in this work. The versatility of this technique comes with a range of technical challenges, especially when cryogenic systems come into consideration. The biggest one is the mechanical stability, necessary to maintain resonances in the cavity. Indeed, cryogenic systems often use mechanically noisy compressors to maintain constant cold-plate temperatures. Furthermore, the helium flow also generates vibrations that propagate to the experimental setup. Isolation stages were designed to reduce the impact on the cavity [109,110], adding extra complexity to the platform. This chapter will describe an open-fiber-cavity system in a bath cryostat and expose the potential of this approach by showing high-mechanical stability.

8.1 EXPERIMENTAL DESIGN

In contrast with closed-cycle, continuous-flow or multistage cryostats, where liquid helium is pumped to and from the cold chamber, a bath cryostat is free from any flow or motion as a mass of liquid helium lies inside a reservoir. The liquid mass is in thermal contact with a cold-plate cooling down the vacuum chamber, comprising the open Fabry-Pérot cavity (Fig.29b). The cryostat model used in this work is a VNF-100 bath cryostat by Janis. The steady operation of bath cryostats at 4 Kelvin makes it a strong candidate for vibration-sensitive-cryogenic experiments. Despite being an attractive approach, this solution has some constraints. Over time, the liquid helium evaporates, and the reservoir needs to be refilled at several days intervals. The cooling-down procedure demands special care due to the high vacuum and low temperatures and liquid helium and nitrogen transfers. The cryostat was

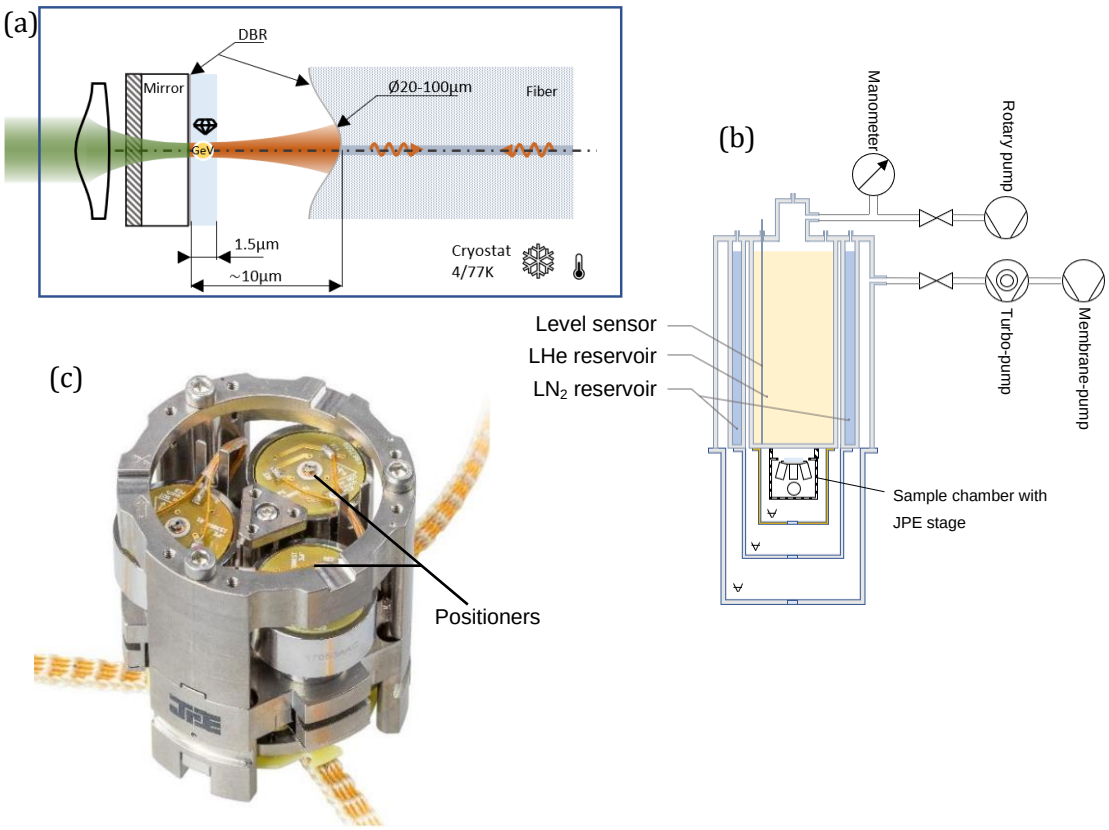

Figure 29 – (a)Open-Fabry-Pérot cavity design schematics. Emitter excitation is done from the flat mirror backhand side. The curved mirror allows cavity mode enhancement. (b) Janis bath cryostat system drawing showing the liquid helium and nitrogen reservoirs, the vacuum isolation walls, and the pumping system. (c) JPE stage showing the 3 actuators moving the sample at the center (source: JPE engineering).

cooled down to 77 K temperature in this work, using exclusively liquid nitrogen in the main reservoir. However, it can be cooled down to 4 K temperature with liquid helium, requiring several cooling stages.

The open cavity comprises a diamond membrane consisting of the GeV centers on a flat mirror and a curved mirror forming a hemispherical cavity, as depicted in Fig.29a. This cavity geometry offers higher mode stability than plano-parallels, which is desirable for experimental setups. The curved mirror is ablated at the tip of an SM fiber (Thorlabs, 630 HP) with a CO_2 laser [74]. The laser pulse blast creates a Gaussian-shaped dimple with an approximate 150 μm radius of curvature at the fiber core. The flat mirror substrate (Coastline Optics) and the fiber-tip are coated with successive dielectric layers to form a distributed Bragg-reflector (DBR). The DBR coating for the flat mirror has high-reflectivity (HR) coefficients at 602 nm and high-transmission (HT) at 532 nm, and the fiber coating is HR for both 602 nm and 532 nm such that the green light is not coupled into the fiber. Hence, off-resonant excitation is enabled from the backside of the flat mirror. The DBR coatings reflection coefficients determine the cavity Finesse according to equation (2-30).

Actuators on different parts of the cavity allow maximal system tunability. The sample is mounted on XYZ positioners (JPE, CPSHR3-S). It enables spatial positioning on the sample's region of interest and coarse cavity length tuning on the sample side. The scanning range is of 8x8x1.6 mm at 4 K. Piezo scanners are also mounted on each axis for fine positioning with a 1.6 μm scan range at 4 K. Instrument control enables wider 2D scans and stitching reconstruction methods. After each 2D confocal map using the piezo scanners, the positioners move by steps of 1.6 μm where another 2D confocal map is done.

The fiber-mirror is mounted on a Z piezo shear stack scanner having a range of 1.5 μm (Noliac, CSAP02). This component is used to scan the cavity length and tune the length in resonance with the laser wavelength and emitter's transition.

8.2 STABILITY MEASUREMENT

Cavity's vibrational response must be as low as possible to keep resonance conditions. We characterize the cavity length fluctuations with a stability measurement. It determines the

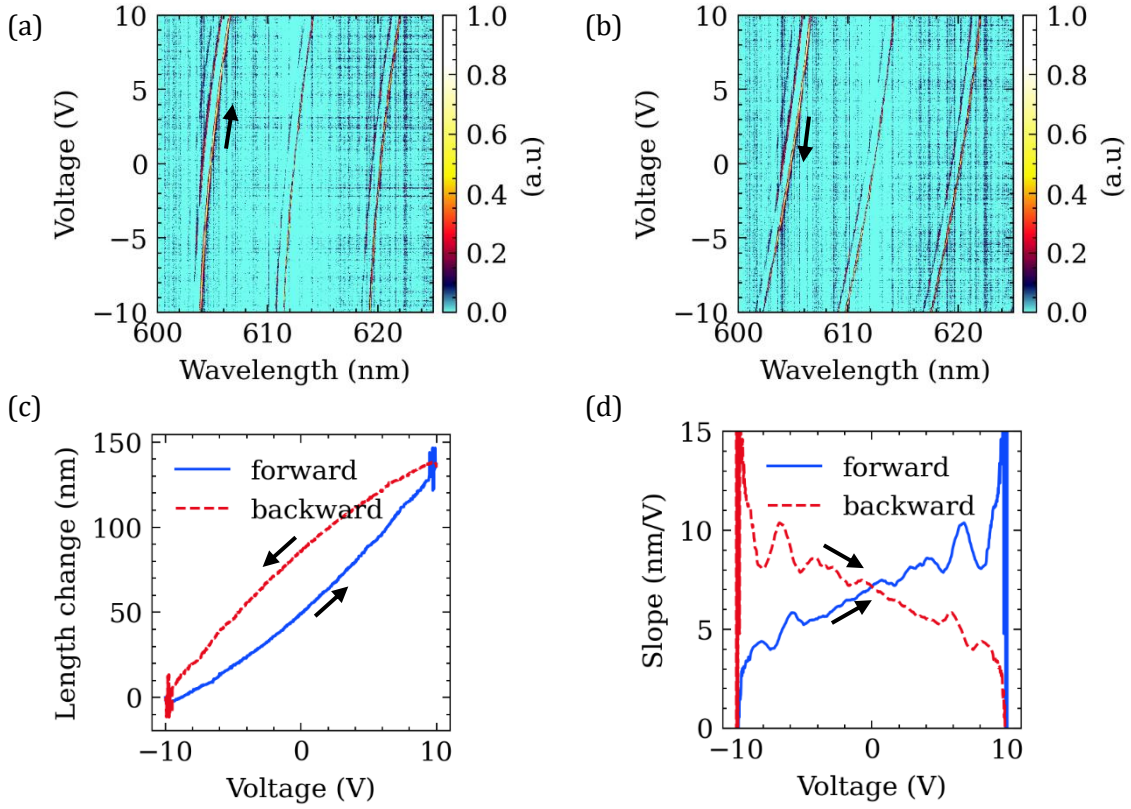

Figure 30 – (a)(b) Cavity resonance spectrum acquired by sending white-light signal and measuring the transmission spectrum while scanning the cavity length. Left is scanning forward, and right is backward. (c) The cavity length is extracted by tracking transmissions peaks. (d) The piezo nonlinear response is obtained by getting the slope from the cavity length measurement in (c).

system's robustness and is done by obtaining the mechanical vibration spectral response when the cavity is in resonance. The following measurements were done at 77 K temperature.

To measure the actual physical displacement when the cavity is on resonance. The cavity's transmission intensity fluctuations are measured with a photodiode (PD). Fig.31a shows the experimental setup used for the measurement. Calibration needs to be done to translate the intensity change measured by the PD into physical displacement.

To do the calibration, a white light laser (NKT Photonics, SuperK Compact) is sent to the cavity to observe resonances and extract the cavity length(Fig.30). The cavity length is defined by:

$$L = \frac{\lambda^2}{2n \cdot FSR_\lambda} \tag{8-1}$$

where FSR_λ is the free spectral range, or the distance between two successive resonances, and n is the refractive index. A cavity length of 13.4 μm is obtained.

A ±10 V voltage ramp signal is applied to the fiber piezo scanner to scan the cavity length, as shown in Fig.30a,b, where the piezo is scanned forward and backward, respectively. The transmission spectrum is acquired to determine the cavity length change ΔL:

$$\frac{\Delta L}{\Delta FSR_\lambda} = \left|\frac{\lambda^2}{2 \cdot (FSR_\lambda)^2}\right| \Rightarrow \Delta L = \frac{\lambda^2}{2 \cdot (FSR_\lambda)^2} \Delta FSR_\lambda \tag{8-2}$$

The resulting cavity length change is shown in Fig.30c. We can observe a hysteresis between forward and backwards scans, which is expected from a piezo. A cavity length difference of ~35 nm is measurable on a ±10 V scan. Piezo actuators have a nonlinear response with respect to the applied voltage. The CSAP02 specifications give a free stroke of 1.5 μm for the entire drive voltage range (±320 V at room temperature). External parameters can affect the stroke, such as the epoxy glue used to mount the fiber on the stack and the stack to the cryostat parts. These parameters can induce an additional nonlinear response to the piezo, combined with the hysteresis. The nonlinear response can be extracted by taking the cavity length curves derivative, which is presented in Fig.30d.

Close to 0 V, we can observe a quasi-linear response of 7 nm/V, with respect to the voltage applied to the piezo scanner. This value allows us to use it as a reference to translate the PD signal into a physical displacement.

This calibration enables the vibrational stability measurement. A resonant 602 nm wavelength laser beam is sent to the cavity, as shown in Fig.31a. The cavity length is set to be at the edge of a resonance. This allows us to get the maximal sensitivity for the vibrational measurement. A ±0.2 V sinewave sweep signal and 70 Hz frequency is applied to the fiber piezo actuator, resulting in a ±1.4 nm displacement. The cavity transmission signal is recorded for 20 seconds at a 320 Hz acquisition rate.(Fig.31b), and the amplitude spectral density (ASP) gives us the vibrational response (Fig.31c). Subsequent measurements can be done to further characterize the cavity stability with a DC voltage tuning the cavity length on-resonance (DC ON), and off-resonance (DC OFF).

From the measurement in Fig.31b, it appears that the slow fluctuations are present in all 3 measurements, including the off-resonance vibration insensitive (DC off) measurement. Therefore, the low-frequency noise most likely stems from the unstable laser power.

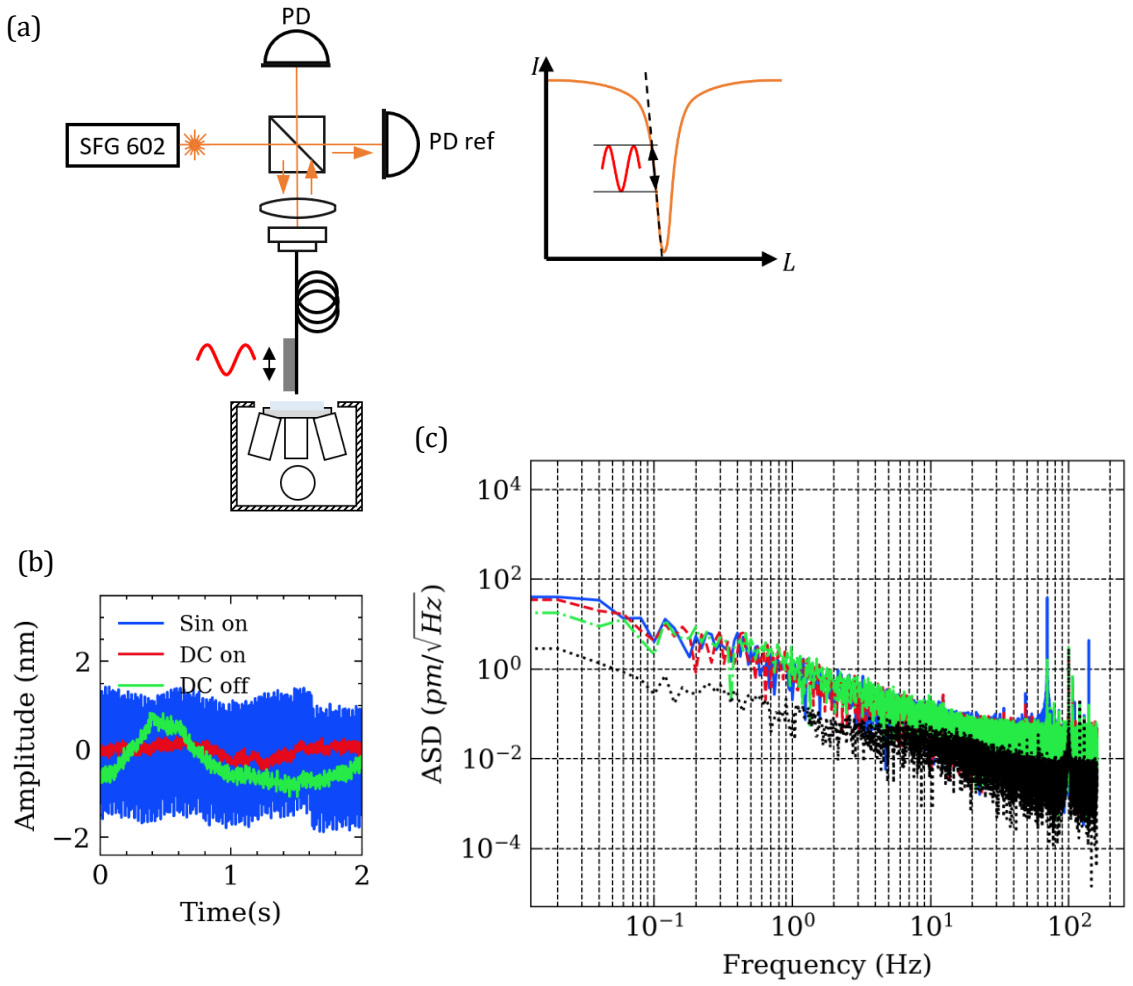

Figure 31 – (a) Vibration measurement schematics where a sinewave signal is applied to the fiber scanner. To maximize the measurement sensitivity, the cavity length is tuned on one of the Lorentzian sides. (b) Cavity length fluctuations time trace over 2 seconds. (c) Amplitude spectrum density ASD of the cavity length fluctuations, with ±0.2 V voltage 70 Hz frequency sine signal (blue), with a DC voltage tuned on cavity resonance (red), off-resonant (green), and the noise floor (black).

Scanning the cavity length at 70 Hz (Sin On) show that the measurement is sensitive to vibration for higher frequencies.

We can conclude that higher frequencies' vibration level is on the sub-pm level. Further, measurement improvements need to be done to characterize the low-frequency stability.

The average displacement is extracted by integrating the amplitude spectral density over the 320 Hz bandwidth to obtain a 50 pm-rms noise floor.

8.3 DISCUSSION

The bath cryostat system offers a mechanical stability that is essential for microcavity experiments.

The path to Purcell enhancement measurements has several challenges that will need to be faced. The high vibrational stability should relieve the experiment from a cavity length locking setup, which would add complexity to the system. Confocal imaging through the cavity will be necessary to observe and select the desired emitter. Therefore, 2D scans will need to be tested in resonance and ensure that the piezo scanners do not alter the cavity stability.

The cooling down procedure is quick and induces thermal drifts throughout the system's mechanical parts. Therefore, pre-alignment is almost futile, and a procedure needs to be established to align the cavity in the enclosed chambers once cold.

Recent work by *Salz et al.* demonstrated the feasibility of this approach by obtaining Purcell enhancement of SiV centers emission at 4 K temperature using a similar setup [81]. These encouraging results offer exciting perspectives for open Fabry-Pérot cavities in bath cryostat.

The attention will also be directed toward commercial solutions that may be released to research groups in the coming years. It has been suggested that isolation stages could enhance closed-cycle cryostats' vibrational stability with <100 pm fluctuations [109].

CHAPTER 9

CONCLUSION & OUTLOOK

9.1 CONCLUSION

Emergent new photonic quantum technologies require reliable interfaces between flying and stationary qubits. Group-IV defects vacancy centers in diamond are promising candidates for such platforms. The GeV centers have a short excited-state lifetime of 2-5 ns, a high Debye-Waller factor of 0.6, and an electron spin lifetime of 25 μs at 2 K, making them great contenders for quantum applications.

An experimental cross-polarization extinction microscope was built to collect photons emitted by the GeV centers' ZPL. The dark-field microscope design used in this work enables a modal transformation of the beam shape due to the Imbert-Fedorov effect yielding an enhancement of excitation beam rejection. Combined with the sole cross-polarization extinction of the optical element, the excitation light rejection of 66 dB at 602 nm wavelength was achieved for the first time on group-IV defects to our knowledge.

We studied photophysical properties at 4 K of deeply implanted GeV centers in a thin diamond membrane. The investigations were conducted on the transition 1-3 (C), the brightest of the four transitions at 4 K temperature. We have shown a homogeneous short excited-state linewidth of 42 MHz, the spectral distribution of spatially selected emitters with ±50 pm standard deviation on the optical transitions, and low spectral diffusion on their optical transitions over several hours. Second-order correlation measurements were conducted with an HBT interferometer detection setup, and evidence of a shelving state was observed with bunching appearing on microsecond up to milliseconds time scales.

Three fluorescence switching effects were reported. 1) Fluorescence intermittency, or optical blinking, is attributed to the existence of a long-lived dark state. Power dependence measurements suggest a two-photon process, which concurs with the work of *Chen et al*. and the shelving processing occurring via a metastable state. 2) A statistical approach was studied by observing spectral jumps, or energy level fluctuations. The amplitude of the jumps ranges

from tenths of MHz to several GHz. SRIM simulations were done to determine the average number of vacancies in the proximity of the defect before annealing. After high-temperature annealing, a significant number of vacancies may remain, which can act as charge traps and cause stark shifts. 3) Finally, optical gating of the PSB fluorescence was observed, where the fluorescence is triggered by the addition of weak nonresonant laser power.

A novel approach using an HBT interferometer was used to extract evidence of nonclassicality in the collected photons statistics with the clicks and no-clicks probabilities. The correlation functions $\alpha(\tau)$ and $\beta(\tau)$ were determined and used as a dual method for nonclassicality detection. Those parameters are independent of Poissonian noise and showed promising results compared to the second-order correlation function. In experiments with resonant excitation schemes, this method showed excellent robustness to the scattered laser light reaching the detectors. We showed that fewer photon counts are needed than $g^{(2)}$ to observe a dip in the β and α functions. Moreover, the time bin used in the data treatment of the β function can be considerably greater than in the $g^{(2)}$ function, speeding up the processing time.

Finally, an open fiber-baser Fabry-Pérot microcavity design in a bath cryostat is proposed as a mechanically stable solution for a light-matter interface. Such platforms allow Purcell enhancement of the fluorescence and increase the photoemission rate. The platform showed a noise floor of 50 pm-rms at 77 K temperature for low frequencies. This high stability is essential for low-temperature cavity measurements.

9.2 OUTLOOK

We have seen the influence of the fabrication process on the optical properties of the GeV centers. The density of the sample showed to have a significant impact on the spectral properties of the emitters. We have shown that two or more emitters having too much proximity influence their optical transitions' wavelengths, probably due to strain in the lattice. A lower density would yield less strain, hence a more homogeneous spectral distribution. Further investigations on similar samples annealed at different temperatures could also give more insight into the vacancies' mobility and their influence on acting as charge traps inducing Stark shifts and spectral jumps.

Moreover, recent results [108] showed that blinking and jumps could be mitigated by adding additional CW off-resonant wavelengths. Further measurements in similar directions could enlighten our understanding of those switching phenomena. Finally, novel annealing methods

using high pressure of 7 GPa and a high temperature of 2100 °C show promising emitter properties.

Setting up pulsed schemes would allow deeper characterization of dynamical properties of the emitters. In addition to extracting physical properties such as the relaxation time and decoherence time, dynamical decoupling spectroscopy would allow better quantification of surrounding noise sources for the GeV centers. Pulsed measurements would also enable to extract exchange rates between the ground and excited states to the dark state.

The observation of optical gating exclusively in the phonon sidebands raises some questions about its origin. A dual collection of the PSB and the ZPL would further test this observation and determine if a thermal process is involved.

The nonclassicality detection with a dual use of the α and β parameters showed exciting results. The robustness to the Poissonian background noise of this approach could become a standard in experimental quantum optics methods. Further theoretical modeling of these parameters in terms of time delays and time bins could unravel information about the emitters' electronic structure.

Finally, further work on the Fabry-Pérot cavity alignment, characterization, and implementation could observe Purcell enhancement at 4 and 77 K temperatures.

“All that remains is more and more precise measurement.”

CHAPTER 10

BIBLIOGRAPHY

[1] S. Wehner, D. Elkouss, and R. Hanson, *Quantum Internet: A Vision for the Road Ahead*, Science (80-.). **362**, (2018).

[2] C. L. Degen, F. Reinhard, and P. Cappellaro, *Quantum Sensing*, (n.d.).

[3] D. P. DiVincenzo and IBM, *The Physical Implementation of Quantum Computation*, Fortschritte Der Phys. **48**, 771 (2000).

[4] B. J. Lawrie, P. D. Lett, A. M. Marino, and R. C. Pooser, *Quantum Sensing with Squeezed Light*, ACS Photonics **6**, 1307 (2019).

[5] J. F. Barry, J. M. Schloss, E. Bauch, M. J. Turner, C. A. Hart, L. M. Pham, and R. L. Walsworth, *Sensitivity Optimization for NV-Diamond Magnetometry*, Rev. Mod. Phys. **92**, 015004 (2020).

[6] S. Slussarenko and G. J. Pryde, *Photonic Quantum Information Processing: A Concise Review*, Appl. Phys. Rev. **6**, 041303 (2019).

[7] J. Wang, F. Sciarrino, A. Laing, and M. G. Thompson, *Integrated Photonic Quantum Technologies*, Nat. Photonics 2019 145 **14**, 273 (2019).

[8] D. A. Vajner, L. Rickert, T. Gao, K. Kaymazlar, and T. Heindel, *Quantum Communication Using Semiconductor Quantum Dots*, (2021).

[9] X. Liu and M. C. Hersam, *2D Materials for Quantum Information Science*, Nat. Rev. Mater. 2019 410 **4**, 669 (2019).

[10] C. D. Bruzewicz, J. Chiaverini, R. McConnell, and J. M. Sage, *Trapped-Ion Quantum Computing: Progress and Challenges*, Appl. Phys. Rev. **6**, 021314 (2019).

[11] S. Pezzagna and J. Meijer, *Quantum Computer Based on Color Centers in Diamond*, Appl. Phys. Rev. **8**, 011308 (2021).

[12] C. Bradac, W. Gao, J. Forneris, M. E. Trusheim, and I. Aharonovich, *Quantum Nanophotonics with Group IV Defects in Diamond*, Nat. Commun. **10**, 1 (2019).

[13] L. Marseglia, J. P. Hadden, A. C. Stanley-Clarke, J. P. Harrison, B. Patton, Y. L. D. Ho, B. Naydenov, F. Jelezko, J. Meijer, P. R. Dolan, J. M. Smith, J. G. Rarity, and J. L. O'brien, *Nanofabricated Solid Immersion Lenses Registered to Single Emitters in Diamond*, Appl. Phys. Lett. **98**, (2011).

[14] J. D. Thompson, K. P. Nayak, M. D. Lukin, N. P. de Leon, T. Peyronel, T. G. Tiecke, and V. Vuletić, *Efficient Fiber-Optical Interface for Nanophotonic Devices*, Opt. Vol. 2, Issue 2, Pp. 70-75 **2**, 70 (2015).

[15] C. Dory, D. Vercruysse, K. Y. Yang, N. V. Sapra, A. E. Rugar, S. Sun, D. M. Lukin, A. Y. Piggott, J. L. Zhang, M. Radulaski, K. G. Lagoudakis, L. Su, and J. Vučković, *Inverse-Designed Diamond Photonics*, Nat. Commun. 2019 101 **10**, 1 (2019).

[16] E. Janitz, L. Childress, and M. K. Bhaskar, *Cavity Quantum Electrodynamics with Color Centers in Diamond*, Opt. Vol. 7, Issue 10, Pp. 1232-1252 **7**, 1232 (2020).

[17] B. C. Rose, D. Huang, Z. H. Zhang, P. Stevenson, A. M. Tyryshkin, S. Sangtawesin, S. Srinivasan, L. Loudin, M. L. Markham, A. M. Edmonds, D. J. Twitchen, S. A. Lyon, and N. P. De Leon, *Observation of an Environmentally Insensitive Solid-State Spin Defect in Diamond*, Science (80-.). **361**, 60 (2018).

[18] B. Pingault, D. D. Jarausch, C. Hepp, L. Klintberg, J. N. Becker, M. Markham, C. Becher, and M. Atatüre, *Coherent Control of the Silicon-Vacancy Spin in Diamond*, Nat. Commun. **8**, 1 (2017).

[19] D. D. D. Sukachev, A. Sipahigil, C. T. Nguyen, M. K. Bhaskar, R. E. Evans, F. Jelezko, and M. D. Lukin, *Silicon-Vacancy Spin Qubit in Diamond: A Quantum Memory Exceeding 10 Ms with Single-Shot State Readout*, Phys. Rev. Lett. **119**, 223602 (2017).

[20] A. E. Rugar, C. Dory, S. Sun, and J. Vučković, *Characterization of Optical and Spin Properties of Single Tin-Vacancy Centers in Diamond Nanopillars*, Phys. Rev. B **99**, 205417 (2019).

[21] K. Bray, B. Regan, A. Trycz, R. Previdi, G. Seniutinas, K. Ganesan, M. Kianinia, S. Kim, and I. Aharonovich, *Single Crystal Diamond Membranes and Photonic Resonators Containing Germanium Vacancy Color Centers*, ACS Photonics **5**, 4817 (2018).

[22] K. G. Fehler, A. P. Ovvyan, L. Antoniuk, N. Lettner, N. Gruhler, V. A. Davydov, V. N. Agafonov, W. H. P. Pernice, and A. Kubanek, *Purcell-Enhanced Emission from Individual SiV-Center in Nanodiamonds Coupled to a Si3N4-Based, Photonic Crystal Cavity*, Nanophotonics **9**, 3655 (2020).

[23] A. Faraon, C. Santori, Z. Huang, V. M. Acosta, and R. G. Beausoleil, *Coupling of Nitrogen-Vacancy Centers to Photonic Crystal Cavities in Monocrystalline Diamond*, Phys. Rev. Lett. **109**, 033604 (2012).

[24] T. Iwasaki, F. Ishibashi, Y. Miyamoto, Y. Doi, S. Kobayashi, T. Miyazaki, K. Tahara, K. D. Jahnke, L. J. Rogers, B. Naydenov, F. Jelezko, S. Yamasaki, S. Nagamachi, T. Inubushi, N. Mizuochi, and M. Hatano, *Germanium-Vacancy Single Color Centers in Diamond*, Sci. Reports 2015 51 **5**, 1 (2015).

[25] I. Aharonovich, C. Zhou, A. Stacey, J. Orwa, S. Castelletto, D. Simpson, A. D. Greentree, F. Treussart, J. F. Roch, and S. Prawer, *Enhanced Single-Photon Emission in the near Infrared from a Diamond Color Center*, Phys. Rev. B - Condens. Matter Mater. Phys. **79**, 235316 (2009).

[26] I. Aharonovich, S. Castelletto, D. A. Simpson, A. Stacey, J. McCallum, A. D. Greentree, and S. Prawer, *Two-Level Ultrabright Single Photon Emission from Diamond Nanocrystals*, Nano Lett. **9**, 3191 (2009).

[27] C. Santori, P. E. Barclay, K. M. C. Fu, R. G. Beausoleil, S. Spillane, and M. Fisch, *Nanophotonics for Quantum Optics Using Nitrogen-Vacancy Centers in Diamond*, Nanotechnology **21**, 274008 (2010).

[28] P. C. Maurer, G. Kucsko, C. Latta, L. Jiang, N. Y. Yao, S. D. Bennett, F. Pastawski, D. Hunger, N. Chisholm, M. Markham, D. J. Twitchen, J. I. Cirac, and M. D. Lukin, *Room-Temperature Quantum Bit Memory Exceeding One Second*, Science (80-.). **336**, 1283 (2012).

[29] M. H. Abobeih, J. Cramer, M. A. Bakker, N. Kalb, M. Markham, D. J. Twitchen, and T. H. Taminiau, *One-Second Coherence for a Single Electron Spin Coupled to a Multi-Qubit Nuclear-Spin Environment*, Nat. Commun. 2018 91 **9**, 1 (2018).

[30] G. Balasubramanian, P. Neumann, D. Twitchen, M. Markham, R. Kolesov, N. Mizuochi, J. Isoya, J. Achard, J. Beck, J. Tissler, V. Jacques, P. R. Hemmer, F. Jelezko, and J. Wrachtrup, *Ultralong Spin Coherence Time in Isotopically Engineered Diamond*, Nat. Mater. **8**, 383 (2009).

[31] I. P. Radko, M. Boll, N. M. Israelsen, N. Raatz, J. Meijer, F. Jelezko, U. L. Andersen, and A. Huck, *Determining the Internal Quantum Efficiency of Shallow-Implanted Nitrogen-Vacancy Defects in Bulk Diamond*, Opt. Express **24**, 27715 (2016).

[32] A. Batalov, C. Zierl, T. Gaebel, P. Neumann, I. Y. Chan, G. Balasubramanian, P. R. Hemmer, F. Jelezko, and J. Wrachtrup, *Temporal Coherence of Photons Emitted by Single Nitrogen-*

Vacancy Defect Centers in Diamond Using Optical Rabi-Oscillations, Phys. Rev. Lett. **100**, 077401 (2008).

[33] K. Y. Han, S. K. Kim, C. Eggeling, and S. W. Hell, *Metastable Dark States Enable Ground State Depletion Microscopy of Nitrogen Vacancy Centers in Diamond with Diffraction-Unlimited Resolution*, Nano Lett. **10**, 3199 (2010).

[34] E. Neu, D. Steinmetz, J. Riedrich-Möller, S. Gsell, M. Fischer, M. Schreck, and C. Becher, *Single Photon Emission from Silicon-Vacancy Colour Centres in Chemical Vapour Deposition Nano-Diamonds on Iridium*, New J. Phys. **13**, 025012 (2011).

[35] J. Görlitz, D. Herrmann, G. Thiering, P. Fuchs, M. Gandil, T. Iwasaki, T. Taniguchi, M. Kieschnick, J. Meijer, M. Hatano, A. Gali, and C. Becher, *Spectroscopic Investigations of Negatively Charged Tin-Vacancy Centres in Diamond*, New J. Phys. **22**, 013048 (2020).

[36] A. Dietrich, K. D. Jahnke, J. M. Binder, T. Teraji, J. Isoya, L. J. Rogers, and F. Jelezko, *Isotopically Varying Spectral Features of Silicon-Vacancy in Diamond*, New J. Phys. **16**, 113019 (2014).

[37] G. Thiering and A. Gali, *Ab Initio Magneto-Optical Spectrum of Group-IV Vacancy Color Centers in Diamond*, Phys. Rev. X **8**, 021063 (2018).

[38] A. T. Collins, L. Allers, C. J. H. Wort, and G. A. Scarsbrook, *The Annealing of Radiation Damage in De Beers Colourless CVD Diamond*, Diam. Relat. Mater. **3**, 932 (1994).

[39] J. Riedrich-Möller, C. Arend, C. Pauly, F. Mücklich, M. Fischer, S. Gsell, M. Schreck, and C. Becher, *Deterministic Coupling of a Single Silicon-Vacancy Color Center to a Photonic Crystal Cavity in Diamond*, Nano Lett. **14**, 5281 (2014).

[40] Y. N. Palyanov, I. N. Kupriyanov, Y. M. Borzdov, and N. V. Surovtsev, *Germanium: A New Catalyst for Diamond Synthesis and a New Optically Active Impurity in Diamond*, Sci. Rep. **5**, (2015).

[41] M. Nguyen, N. Nikolay, C. Bradac, M. Kianinia, E. A. Ekimov, N. Mendelson, O. Benson, and I. Aharonovich, *Photodynamics and Quantum Efficiency of Germanium Vacancy Color Centers in Diamond*, Adv. Photonics **1**, 1 (2020).

[42] T. Iwasaki, Y. Miyamoto, T. Taniguchi, P. Siyushev, M. H. Metsch, F. Jelezko, and M. Hatano, *Tin-Vacancy Quantum Emitters in Diamond*, Phys. Rev. Lett. **119**, 253601 (2017).

[43] S. D. Tchernij, T. Herzig, J. Forneris, J. Küpper, S. Pezzagna, P. Traina, E. Moreva, I. P.

Degiovanni, G. Brida, N. Skukan, M. Genovese, M. Jakšić, J. Meijer, and P. Olivero, *Single-Photon-Emitting Optical Centers in Diamond Fabricated upon Sn Implantation*, ACS Photonics **4**, 2580 (2017).

[44] T. Lühmann, J. Küpper, S. Dietel, R. Staacke, J. Meijer, and S. Pezzagna, *Charge-State Tuning of Single SnV Centers in Diamond*, ACS Photonics **7**, 3376 (2020).

[45] S. Ditalia Tchernij, T. Lühmann, T. Herzig, J. Küpper, A. Damin, S. Santonocito, M. Signorile, P. Traina, E. Moreva, F. Celegato, S. Pezzagna, I. P. Degiovanni, P. Olivero, M. Jakšić, J. Meijer, P. M. Genovese, and J. Forneris, *Single-Photon Emitters in Lead-Implanted Single-Crystal Diamond*, ACS Photonics **5**, 4864 (2018).

[46] P. Wang, T. Taniguchi, Y. Miyamoto, M. Hatano, and T. Iwasaki, *Low-Temperature Spectroscopic Investigation of Lead-Vacancy Centers in Diamond Fabricated by High-Pressure and High-Temperature Treatment*, ACS Photonics **8**, 2947 (2021).

[47] S. D. Tchernij, E. Corte, T. Lühmann, P. Traina, S. Pezzagna, I. Pietro Degiovanni, G. Provatas, E. Moreva, J. Meijer, P. Olivero, M. Genovese, J. Forneris, S. Ditalia Tchernij, E. Corte, T. Lühmann, P. Traina, S. Pezzagna, I. Pietro Degiovanni, G. Provatas, E. Moreva, J. Meijer, P. Olivero, M. Genovese, and J. Forneris, *Spectral Features of Pb-Related Color Centers in Diamond – a Systematic Photoluminescence Characterization*, New J. Phys. **23**, 063032 (2021).

[48] K. D. Jahnke, A. Sipahigil, J. M. Binder, M. W. Doherty, M. Metsch, L. J. Rogers, N. B. Manson, M. D. Lukin, and F. Jelezko, *Electron-Phonon Processes of the Silicon-Vacancy Centre in Diamond*, New J. Phys **17**, 43011 (2015).

[49] L. J. L. Rogers, K. D. Jahnke, M. H. Metsch, A. Sipahigil, J. M. Binder, T. Teraji, H. Sumiya, J. Isoya, M. D. Lukin, P. Hemmer, and F. Jelezko, *All-Optical Initialization, Readout, and Coherent Preparation of Single Silicon-Vacancy Spins in Diamond*, Phys. Rev. Lett. **113**, 263602 (2014).

[50] P. Siyushev, M. H. Metsch, A. Ijaz, J. M. Binder, M. K. Bhaskar, D. D. Sukachev, A. Sipahigil, R. E. Evans, C. T. Nguyen, M. D. Lukin, P. R. Hemmer, Y. N. Palyanov, I. N. Kupriyanov, Y. M. Borzdov, L. J. Rogers, and F. Jelezko, *Optical and Microwave Control of Germanium-Vacancy Center Spins in Diamond*, **96**, 081201 (2017).

[51] B. Pingault, J. N. Becker, C. H. H. Schulte, C. Arend, C. Hepp, T. Godde, A. I. Tartakovskii, M. Markham, C. Becher, and M. Atatüre, *All-Optical Formation of Coherent Dark States of Silicon-Vacancy Spins in Diamond*, Phys. Rev. Lett. **113**, 263601 (2014).

[52] Y. I. Sohn, S. Meesala, B. Pingault, H. A. Atikian, J. Holzgrafe, M. Gündoğan, C. Stavrakas, M. J. Stanley, A. Sipahigil, J. Choi, M. Zhang, J. L. Pacheco, J. Abraham, E. Bielejec, M. D. Lukin, M. Atatüre, and M. Lončar, *Controlling the Coherence of a Diamond Spin Qubit through Its Strain Environment*, **9**, 1 (2018).

[53] M. E. Trusheim, B. Pingault, N. H. Wan, M. Gündoğan, L. De Santis, R. Debroux, D. Gangloff, C. Purser, K. C. Chen, M. Walsh, J. J. Rose, J. N. Becker, B. Lienhard, E. Bersin, I. Paradeisanos, G. Wang, D. Lyzwa, A. R. P. Montblanch, G. Malladi, H. Bakhru, A. C. Ferrari, I. A. Walmsley, M. Atatüre, and D. Englund, *Transform-Limited Photons from a Coherent Tin-Vacancy Spin in Diamond*, Phys. Rev. Lett. **124**, 023602 (2020).

[54] R. Debroux, C. P. Michaels, C. M. Purser, N. Wan, M. E. Trusheim, J. Arjona Martínez, R. A. Parker, A. M. Stramma, K. C. Chen, L. De Santis, E. M. Alexeev, A. C. Ferrari, D. Englund, D. A. Gangloff, and M. Atatüre, *Quantum Control of the Tin-Vacancy Spin Qubit in Diamond*, Phys. Rev. X **11**, 041041 (2021).

[55] A. M. Edmonds, M. E. Newton, P. M. Martineau, D. J. Twitchen, and S. D. Williams, *Electron Paramagnetic Resonance Studies of Silicon-Related Defects in Diamond*, Phys. Rev. B - Condens. Matter Mater. Phys. **77**, 245205 (2008).

[56] B. C. Rose, G. Thiering, A. M. Tyryshkin, A. M. Edmonds, M. L. Markham, A. Gali, S. A. Lyon, and N. P. De Leon, *Strongly Anisotropic Spin Relaxation in the Neutral Silicon Vacancy Center in Diamond*, Phys. Rev. B **98**, 235140 (2018).

[57] J. Görlitz, D. Herrmann, P. Fuchs, T. Iwasaki, T. Taniguchi, D. Rogalla, D. Hardeman, P.-O. Colard, M. Markham, M. Hatano, and C. Becher, *Coherence of a Charge Stabilised Tin-Vacancy Spin in Diamond*, (2021).

[58] M. K. K. K. Bhaskar, D. D. D. D. Sukachev, A. Sipahigil, R. E. E. E. Evans, M. J. J. J. Burek, C. T. T. T. Nguyen, L. J. J. J. Rogers, P. Siyushev, M. H. H. H. Metsch, H. Park, F. Jelezko, M. Lončar, M. D. D. D. Lukin, M. Loncar, and M. D. D. D. Lukin, *Quantum Nonlinear Optics with a Germanium-Vacancy Color Center in a Nanoscale Diamond Waveguide*, Phys. Rev. Lett. **118**, 223603 (2017).

[59] S. Maity, L. Shao, Y.-I. Sohn, S. Meesala, B. Machielse, E. Bielejec, M. Markham, and M. Lončar, *Spectral Alignment of Single-Photon Emitters in Diamond Using Strain Gradient*, Phys. Rev. Appl. **10**, 024050 (2018).

[60] D. Chen, Z. Mu, Y. Zhou, J. E. Fröch, A. Rasmit, C. Diederichs, N. Zheludev, I. Aharonovich, and W.-B. B. Gao, *Optical Gating of Resonance Fluorescence from a Single Germanium Vacancy Color Center in Diamond*, Phys. Rev. Lett. **123**, 1 (2019).

[61] G. S. Agarwal, *Quantum Optics* (Cambridge University Press, 2013).

[62] D. A. Requena, Resonant Excitation of Colour Centres in Diamond, DTU, 2021.

[63] I. Aharonovich, D. Englund, and M. Toth, *Solid-State Single-Photon Emitters*, Nat. Photonics **10**, 631 (2016).

[64] R. J. Glauber, *Photon Correlations*, Phys. Rev. Lett. **10**, 84 (1963).

[65] R. J. Glauber, *Coherent and Incoherent States of the Radiation Field*, Phys. Rev. **131**, 2766 (1963).

[66] E. C. G. Sudarshan, *Equivalence of Semiclassical and Quantum Mechanical Descriptions of Statistical Light Beams*, Phys. Rev. Lett. **10**, 277 (1963).

[67] H. J. Kimble, M. Dagenais, and L. Mandel, *Photon Antibunching in Resonance Fluorescence*, Phys. Rev. Lett. **39**, 691 (1977).

[68] R. E. Slusher, L. W. Hollberg, B. Yurke, J. C. Mertz, and J. F. Valley, *Observation of Squeezed States Generated by Four-Wave Mixing in an Optical Cavity*, Phys. Rev. Lett. **55**, 2409 (1985).

[69] C. H. H. Schulte, J. Hansom, A. E. Jones, C. Matthiesen, C. Le Gall, and M. Atatüre, *Quadrature Squeezed Photons from a Two-Level System*, Nature **525**, 222 (2015).

[70] P. Obšil, L. Lachman, T. Pham, A. Lešundák, V. Hucl, M. ČíŽek, J. Hrabina, O. Číp, L. Slodička, and R. Filip, *Nonclassical Light from Large Ensembles of Trapped Ions*, Phys. Rev. Lett. **120**, 253602 (2018).

[71] R. Filip and L. Lachman, *Hierarchy of Feasible Nonclassicality Criteria for Sources of Photons*, Phys. Rev. A - At. Mol. Opt. Phys. **88**, 043827 (2013).

[72] L. Lachman, L. Slodička, and R. Filip, *Nonclassical Light from a Large Number of Independent Single-Photon Emitters*, Sci. Reports 2016 61 **6**, 1 (2016).

[73] E. Janitz, *A Fabry-Pérot Microcavity for Quantum Optics with Atomic Defects in Diamond*, (2019).

[74] R. Høy Jensen, Cavity-Enhanced Emission from Germanium Vacancy Centers in Diamond, 2019.

[75] B. R. Patton, F. Grazioso, G. M. Hughes, J. M. Smith, and P. R. Dolan, *Femtoliter Tunable Optical Cavity Arrays*, Opt. Lett. Vol. 35, Issue 21, Pp. 3556-3558 **35**, 3556 (2010).

[76] D. Hunger, T. Steinmetz, Y. Colombe, C. Deutsch, T. W. Hänsch, and J. Reichel, *A Fiber*

Fabry–Perot Cavity with High Finesse, New J. Phys. **12**, 065038 (2010).

[77] D. Riedel, S. Flågan, P. Maletinsky, and R. J. Warburton, *Cavity-Enhanced Raman Scattering for in Situ Alignment and Characterization of Solid-State Microcavities*, Phys. Rev. Appl. **13**, 014036 (2020).

[78] J. Benedikter, H. Kaupp, T. Hümmer, Y. Liang, A. Bommer, C. Becher, A. Krueger, J. M. Smith, T. W. Hänsch, and D. Hunger, *Cavity-Enhanced Single-Photon Source Based on the Silicon-Vacancy Center in Diamond*, Phys. Rev. Appl. **7**, 024031 (2017).

[79] S. Häußler, J. Benedikter, K. Bray, B. Regan, A. Dietrich, J. Twamley, I. Aharonovich, D. Hunger, and A. Kubanek, *Diamond Photonics Platform Based on Silicon Vacancy Centers in a Single-Crystal Diamond Membrane and a Fiber Cavity*, Phys. Rev. B **99**, 1 (2019).

[80] R. H. Jensen, E. Janitz, Y. Fontana, Y. He, O. Gobron, I. P. Radko, M. Bhaskar, R. Evans, C. D. R. Rosenblueth, L. Childress, A. Huck, and U. L. Andersen, *Cavity-Enhanced Photon Emission from a Single Germanium-Vacancy Center in a Diamond Membrane*, (2019).

[81] M. Salz, Y. Herrmann, A. Nadarajah, A. Stahl, M. Hettrich, A. Stacey, S. Prawer, D. Hunger, and F. Schmidt-Kaler, *Cryogenic Platform for Coupling Color Centers in Diamond Membranes to a Fiber-Based Microcavity*, Appl. Phys. B Lasers Opt. **126**, 1 (2020).

[82] Y. Fontana, R. Zifkin, E. Janitz, C. D. Rodríguez Rosenblueth, and L. Childress, *A Mechanically Stable and Tunable Cryogenic Fabry–Pérot Microcavity*, Rev. Sci. Instrum. **92**, 053906 (2021).

[83] S. B. Van Dam, M. Ruf, and R. Hanson, *Optimal Design of Diamond-Air Microcavities for Quantum Networks Using an Analytical Approach*, New J. Phys. **20**, (2018).

[84] J. Riedrich-Moller, *One- and Two-Dimensional Photonic Crystal Microcavities in Single Crystal Diamond*, Nat. Nanotech. **7**, 69 (2012).

[85] J. L. Zhang, S. Sun, M. J. Burek, C. Dory, Y. K. Tzeng, K. A. Fischer, Y. Kelaita, K. G. Lagoudakis, M. Radulaski, Z. X. Shen, N. A. Melosh, S. Chu, M. Lončar, and J. Vučković, *Strongly Cavity-Enhanced Spontaneous Emission from Silicon-Vacancy Centers in Diamond*, Nano Lett. **18**, 1360 (2018).

[86] K. Kuruma, B. Pingault, C. Chia, D. Renaud, P. Hoffmann, S. Iwamoto, C. Ronning, and M. Lončar, *Coupling of a Single Tin-Vacancy Center to a Photonic Crystal Cavity in Diamond*, Appl. Phys. Lett. **118**, 230601 (2021).

[87] A. E. Rugar, S. Aghaeimeibodi, D. Riedel, C. Dory, H. Lu, P. J. McQuade, Z. X. Shen, N. A.

Melosh, and J. Vučković, *Quantum Photonic Interface for Tin-Vacancy Centers in Diamond*, Phys. Rev. X **11**, 031021 (2021).

[88] Y. Chu, N. P. De Leon, B. J. Shields, B. Hausmann, R. Evans, E. Togan, M. J. Burek, M. Markham, A. Stacey, A. S. Zibrov, A. Yacoby, D. J. Twitchen, M. Loncar, H. Park, P. Maletinsky, and M. D. Lukin, *Coherent Optical Transitions in Implanted Nitrogen Vacancy Centers*, Nano Lett. **14**, 1982 (2014).

[89] William G Eversole, *Synthesis of Diamond*, US3030188A (1961).

[90] T. Fukui, Y. Doi, T. Miyazaki, Y. Miyamoto, H. Kato, T. Matsumoto, T. Makino, S. Yamasaki, R. Morimoto, N. Tokuda, M. Hatano, Y. Sakagawa, H. Morishita, T. Tashima, S. Miwa, Y. Suzuki, and N. Mizuochi, *Perfect Selective Alignment of Nitrogen-Vacancy Centers in Diamond*, Appl. Phys. Express **7**, 055201 (2014).

[91] J. Michl, T. Teraji, S. Zaiser, I. Jakobi, G. Waldherr, F. Dolde, P. Neumann, M. W. Doherty, N. B. Manson, J. Isoya, and J. Wrachtrup, *Perfect Alignment and Preferential Orientation of Nitrogen-Vacancy Centers during Chemical Vapor Deposition Diamond Growth on (111) Surfaces*, Appl. Phys. Lett. **104**, 102407 (2014).

[92] H. Ozawa, K. Tahara, H. Ishiwata, M. Hatano, and T. Iwasaki, *Formation of Perfectly Aligned Nitrogen-Vacancy-Center Ensembles in Chemical-Vapor-Deposition-Grown Diamond (111)*, Appl. Phys. Express **10**, 045501 (2017).

[93] J. F. Ziegler, M. D. Ziegler, and J. P. Biersack, *SRIM – The Stopping and Range of Ions in Matter (2010)*, Nucl. Instruments Methods Phys. Res. Sect. B Beam Interact. with Mater. Atoms **268**, 1818 (2010).

[94] Y. Chu, Quantum Optics with Atom-like Systems in Diamond A Dissertation Presented, 2013.

[95] Element Six, *Diamond Handbook* (2021).

[96] P. Maletinsky, S. Hong, M. S. Grinolds, B. Hausmann, M. D. Lukin, R. L. Walsworth, M. Loncar, and A. Yacoby, *A Robust Scanning Diamond Sensor for Nanoscale Imaging with Single Nitrogen-Vacancy Centres*, Nat. Nanotechnol. 2012 75 **7**, 320 (2012).

[97] B. J. M. Hausmann, I. Bulu, M. Lončar, M. J. Burek, P. Latawiec, and V. Venkataraman, *On-Chip Diamond Raman Laser*, Opt. Vol. 2, Issue 11, Pp. 924-928 **2**, 924 (2015).

[98] M. Akaishi, H. Kanda, and S. Yamaoka, *High Pressure Synthesis of Diamond in the Systems of Grahpite-Sulfate and Graphite-Hydroxide*, Jpn. J. Appl. Phys. **29**, L1172 (1990).

[99] M. C. T. Bahaa E. A. Saleh, *Fundamentals of Photonics*, in 2nd ed. (Wiley, 2007), p. 1177.

[100] *Optical Cryostat - AttoDRY800*, https://www.attocube.com/en/products/cryostats/closed-cycle-cryostats/attodry800-optical-cryostat.

[101] M. Benelajla, E. Kammann, B. Urbaszek, and K. Karrai, *Physical Origins of Extreme Cross-Polarization Extinction in Confocal Microscopy*, Phys. Rev. X **11**, 021007 (2021).

[102] J. M. Binder, A. Stark, N. Tomek, J. Scheuer, F. Frank, K. D. Jahnke, C. Müller, S. Schmitt, M. H. Metsch, T. Unden, T. Gehring, A. Huck, U. L. Andersen, L. J. Rogers, and F. Jelezko, *Qudi: A Modular Python Suite for Experiment Control and Data Processing*, SoftwareX **6**, 85 (2017).

[103] S. Lindner, A. Bommer, A. Muzha, A. Krueger, L. Gines, S. Mandal, O. Williams, E. Londero, A. Gali, and C. Becher, *Strongly Inhomogeneous Distribution of Spectral Properties of Silicon-Vacancy Color Centers in Nanodiamonds Recent Citations Strongly Inhomogeneous Distribution of Spectral Properties of Silicon-Vacancy Color Centers in Nanodiamonds*, New J. Phys **20**, 115002 (2018).

[104] W. Demtröder, *Laser Spectroscopy: Fourth Edition*, Vol. 1 (Springer Berlin Heidelberg, 2008).

[105] Z. Mu, Y. Zhou, D. Chen, J. E. Fröch, J. Yang, X. Li, I. Aharonovich, and W.-B. Gao, *Observation of Binary Spectral Jumps in Color Centers in Diamond*, Adv. Opt. Mater. **8**, 2000495 (2020).

[106] L. De Santis, M. Trusheim, K. Chen, and D. Englund, *Investigation of the Stark Effect on a Centrosymmetric Quantum Emitter in Diamond*, (2021).

[107] S. Aghaeimeibodi, D. Riedel, A. E. Rugar, C. Dory, and J. Vučković, *Electrical Tuning of Tin-Vacancy Centers in Diamond*, Phys. Rev. Appl. **15**, 064010 (2021).

[108] P. Fuchs, J. Görlitz, R. Morsch, D. Herrmann, and C. Becher, *Optical Interfacing of Tin-Vacancy Spin Qubits in Diamond*, Https://Doi.Org/10.1117/12.2615298 **PC12010**, PC1201019 (2022).

[109] S. Vadia, J. Scherzer, H. Thierschmann, C. Schäfermeier, C. Dal Savio, T. Taniguchi, K. Watanabe, D. Hunger, K. Karraï, and A. Högele, *Open-Cavity in Closed-Cycle Cryostat as a Quantum Optics Platform*, PRX Quantum **2**, 040318 (2021).

[110] E. Janitz, M. Ruf, Y. Fontana, J. Sankey, and L. Childress, *High Mechanical Bandwidth*

Fiber-Coupled Fabry-Perot Cavity, Opt. Express **25**, 20932 (2017).

Point defects in diamond are promising candidates in the solid-state for a wide range of applications in quantum information processing. Among different defects with allowed optical transitions, the germanium-vacancy center (GeV) is attractive because it has good optical properties at room temperature, including a narrow zero-phonon line and low emission into the phonon sideband. Some of the GeV center's intrinsic physical properties are yet unknown. This contribution focuses on the optical investigation of single GeV center deeply implanted into a synthetic diamond crystal at a cryogenic sample temperature of 4K. Single GeV center's optical properties are monitored by collecting photons emitted in the phonon side band and the zero-phonon line using a cross-polarization scheme. Applying a resonant optical excitation scheme, we report on the observation of fluorescence switching effects with the evidence of a dark shelving state, optical gating of the phonon-sidebands emission with the addition of weak power off-resonant laser, and discrete spectral jumps. Further, evidence of nonclassical states of light is studied using a dual correlation approach. Finally, a fiber-based Fabry-Pérot microcavity in a bath cryostat design is proposed as a low vibration solution for enabling Purcell enhancement.

Technical
University of
Denmark

Bygning 311
Fysikvej
2800 Kgs. Lyngby
Tlf. 45 25 33 44
Fax: 45 93 23 99